Temperature-Induced Metamagnetic Transition and Domain Structures of Single-Crystalline FeRh Thin Films on MgO(100)

Inaugural-Dissertation

zur

Erlangung des Doktorgrades

der Mathematisch-Naturwissenschaftlichen Fakultät

der Universität zu Köln

vorgelegt von

Xianzhong Zhou

aus Guangdong, China

Jülich, 2013

Berichterstatter: (Gutachter)	PD Dr. Daniel E. Bürgler
	Prof. Dr. Thomas Michely

Tag der mündlichen Prüfung: 16.10.2013

Abstract

Exchange systems of FeRh with a hard magnetic layer are a promising approach for heat-assisted magnetic recording that can largely increase the storage density of hard disk drives. The FeRh alloy is known to undergo a temperature-induced metamagnetic transition from antiferromagnetic (AFM) to ferromagnetic (FM) just above the room temperature. But the AFM and FM phases coexist across the transition in single-crystalline FeRh thin films with thin capping layers (e.g. Au, Al, or MgO). In order to investigate the intrinsic surface magnetic properties, single-crystalline FeRh films without capping layer are prepared by two kinds of experimental procedures.

For the ex-situ sample preparation procedure, two 40 nm thick, single-crystalline FeRh films are prepared on MgO(100) by separate layer deposition of Fe and Rh. X-ray photoemission spectroscopy (XPS) immediately after the deposition shows that one sample is Rh-rich and the other Fe-rich. The samples are exposed to air and transferred to a second ultra-high vacuum (UHV) system to perform the magnetic characterization. This transfer results in a contamination by C and O. After surface cleaning by high-temperature annealing the Rh-rich sample is still slightly contaminated with C, while the Fe-rich surface is oxidized. Magneto-optical Kerr effect (MOKE) measurements reveal that only the Rh-rich sample shows the metamagnetic transition below room temperature. The Fe-rich sample is FM at 193 and 293 K. Scanning electron microscopy with polarization analysis (SEMPA) reveals that the Rh-rich surface is FM at all temperatures between 160 and 450 K although the bulk is AFM below room temperature.

For the in-situ sample preparation procedure, a 10 nm single-crystalline FeRh film is prepared on MgO(100) again by separate layer deposition of Fe and Rh but now in the same UHV system as all characterizations. Thus, the intrinsic properties of the single-crystalline FeRh film are investigated without exposure to air and additional cleaning steps. The in-situ prepared FeRh film also exhibits the metamagnetic phase transition below room temperature as indicated by MOKE. The temperature dependent domain structure obtained by SEMPA reveals that FM domains exist at the surface while the bulk is AFM. In contrast to the ex-situ prepared sample the domain size changes drastically at the transition temperature. This is related to a spin reorientation transition from out-of-plane to in-plane between 350 to 400 K.

The results show that the previously observed coexistence of the FM state at the

surface and the AFM phase in the bulk is not due to an artifact of capping layers or surface contamination. This coexistence is shown in this work to be an intrinsic property of (100) surfaces of single-crystalline FeRh thin films on MgO(100).

Zusammenfassung

FeRh Schichten in Austauschwechselwirkung mit einer magnetisch harten Schicht sind ein vielversprechender Ansatz für die wärmeunterstützte magnetische Datenspeicherung (engl. *Heat-Assisted Magnetic Recording*), mit der die Speicherdichte von Festplatten erheblich erhöht werden kann. Die FeRh Legierung zeigt nahe Raumtemperatur einen Temperatur-induzierten metamagnetischen Phasenübergang von antiferromagnetisch (AFM) zu ferromagnetisch (FM). In einkristallinen FeRh dünnen Filmen mit Deckschicht (z.B. Au, Al oder MgO) können die AFM und FM Phasen im Bereich des Phasenübergangs koexistieren. Mit dem Ziel, die intrinsischen Oberflächeneigenschaften von FeRh zu untersuchen, werden in dieser Arbeit einkristalline FeRh Filme ohne Deckschicht nach zwei verschiedenen Verfahren präpariert und ihre magnetischen Eigenschaften untersucht.

Im Rahmen der ex-situ Probenpräparation werden zwei 40 nm dicke, einkristalline FeRh Filme auf MgO(100) durch separate Deposition von Fe und Rh und anschließendes Tempern synthetisiert. Röntgenphotoemissionsspektroskopie (XPS) zeigt direkt nach der Deposition, dass eine Probe einen Überschuss an Fe und die andere Probe einen Überschuss an Rh aufweist. Danach werden die Proben der Umgebungsluft ausgesetzt, um sie in ein weiteres Ultrahochvakuum (UHV) System zu transferieren, in dem die magnetische Charakterisierung durchgeführt werden kann. Anschließend werden die Proben bei 900 K angelassen, um Oberflächenverunreinigungen wie C oder O zu desorbieren. Als Ergebnis ist die Rh-reiche Probe noch minimal C-kontaminiert, und die Fe-reiche Probe ist an der Oberfläche oxidiert. Messungen des magneto-optischen Kerr Effekts (MOKE) zeigen, dass nur die Rh-reiche Probe einen megamagnetischen Phasenübergang aufweist, und zwar unterhalb Raumtemperatur. Die Fe-reiche Probe dagegen ist bei 193 und 293 K FM. Rasterelektronenmikroskopie mit Polarisationsanalyse (SEMPA) ergibt, dass die Rh-reiche Oberfläche zwischen 160 und 450 K FM ist, während das Volumen des Films nach MOKE unterhalb Raumtemperatur AFM ist.

Beim in-situ Präparationsverfahren werden 10 nm dicke FeRh Schichten wiederum durch separate Deposition von Fe und Rh auf MgO(001) synthetisiert, nun aber direkt in dem UHV System, in dem sämtliche Charakterisierungen durchgeführt werden. Deshalb können nun die intrinsischen Eigenschaften ohne Verunreinigung durch Umgebungsluft und ohne zusätzliche Reinigungsschritte untersucht werden. Diese in-situ hergestellten FeRh Filme zeigen gemäß MOKE Messungen einen metamagnetischen Phasenübergang unterhalb Raumtemperatur. Die mittels SEMPA abgebildeten temperaturabhängigen Domänenstrukturen zeigen, dass FM

Domämen an der Oberfläche existieren, während das Volumen des Films AFM ist. Im Gegensatz zur ex-situ präparierten Probe ändert sich hier im Bereich der metamagnetischen Übergangstemperatur die Domänengröße drastisch, was auf einen Spinumorientierungsübergang von senkrecht zu parallel zur Probenoberfläche bei einer Temperatur zwischen 350 bis 400 K zurückgeführt wird.

Die Ergebnisse zeigen, dass die bereits früher beobachtete Koexistenz der FM Phase an der Oberfläche mit der AFM Phase im Volumen kein Artefakt von Deckschichten oder Oberflächenverunreinigungen ist. Die hier nachgewiesene Koexistenz der beiden magnetischen Phasen ist vielmehr eine intrinsische Eigenschaft der (100) Oberfläche von einkristallinen, dünnen FeRh Film auf MgO(100).

Contents

List of Figures

List of Tables

1. Introduction

Since the first disk drive, the legendary IBM 305 RAMAC, was introduced in 1956, magnetic disk storage is one of the most important modern data storage technologies [1]. The rapid evolution of magnetic hard disks during the past couple of years is the result of many new technological innovations [2], including giant magnetoresistance (GMR) [3, 4] and tunnelling magnetoresistance (TMR) [5, 6]. Compared to the semiconductor random-access memory (RAM), magnetic disk storage is slower for data access, but magnetic disk storage is always nonvolatile, i.e., no power is required to preserve the data.

The demand of market for increasing data storage capacity at decreasing cost per gigabyte (GB) requires a tremendously increasing storage areal density (GB/in^2) of hard disks. In order to achieve higher areal density, the magnetic grain size needs to be continually decreased to guarantee a sufficient signal-to-noise ratio (SNR) of the readback signal [7]. On the other hand, the reduction of the grain size leads to the reduction of the thermal stability due to the superparamagnetic limit [8]. In the superparamagnetic limit, the magnetization direction of a grain fluctuates randomly, because the thermal energy k_BT, which is the product of Boltzmann constant k_B and the temperature T, can overcome the switching energy barrier K_uV given by the product of the uniaxial anisotropy constant K_u and the grain volume V, if the grain size is too small. In order to have long time thermal stability of written bits, the stability ratio K_uV/k_BT should be larger than 35 for conventional longitudinal magnetic recording [9].

One way to avoid the superparamagnetic limit is increasing the uniaxial anisotropy constant, which is employed in perpendicular recording [10, 11]. However, as the grain size is continually decreasing, the uniaxial anisotropy constant needs to continually increase. At some point, the coercivity will become so larger that the maximum magnetic field generated by the write head of the hard disk drive can not switch the magnetization anymore. The superparamagnetic limit imposes a tradeoff between SNR, thermal stability, and writing field that limits the scaling of magnetic recording to higher storage density. Heat-assisted magnetic recording (HAMR) is a promising approach to extend the storage density continually [12]. In HAMR, the high anisotropy and small grain size magnetic recording medium is heated up to significantly reduce the coercivity before the writing process, and then immediately cooled down to ensure the thermal stability of the recorded information. In principle, a semiconductor laser with a near-field transducer can be used as a fast heat source for HAMR [13]. But for a normal perpendicular mag-

netic recording material, only when it is heated up to near the Curie temperature, the coercivity can be significantly reduced. With these high temperatures, heating dissipation will become a serious problem, and the power consumption is inevitably much higher than for conventional perpendicular magnetic recording.

A bi-layer system comprising one layer of FeRh and another layer of FePt can solve these problems [14, 15]. FePt is a high anisotropy magnetic material, while FeRh undergoes a temperature-induced metamagnetic transition. The magnetization of FeRh abruptly sets in upon heating just above room temperature (e.g. 350 K [16]) due to a first-order magnetic phase transition from antiferromagnetic to ferromagnetic order. The first-order transition temperature can easily be changed by adding a small amount of impurity, i.e., Pd can decrease the transition temperature, while Ir can increase the transition temperature [17]. If the bi-layer system is heated above the first-order transition temperature for the writing process, FeRh is a soft ferromagnetic material and becomes exchange coupled to the much harder FePt. The total coercivity of the bilayer is then significantly reduced compared to a single layer of FePt due to the so-called exchange spring mechanism [18]. After writing, when the bi-layer system is cooled to room temperature, FeRh becomes antiferromagnetic, and the FePt layer provides the high anisotropy energy that ensures the thermal stability for long-time stable data storage.

Figure 1.1 shows a promising scheme for a future high density HAMR hard disk drive. It mainly contains two parts, a FeRh/FePt bi-layer system as data storage medium and an integrated head, which has at least three functions: heating, writing, and reading. A semiconductor laser and a near-field transducer are used heat exactly the area for writing, which is done inductively as in conventional write heads. A TMR or GMR sensor is used for reading. The transition from antiferromagnetic to ferromagnetic in FeRh can be triggered with femtosecond optical pulses [19, 20], which leads to the possibility of ultrafast data writing.

Although it has already been found decades ago [21] that FeRh exhibits a first-order phase transition from antiferromagnetic to ferromagnetic, the mechanism of the transition is still under debate, especially concerning the surface magnetic properties of single-crystalline FeRh thin films. Recently, it was found by X-ray magnetic circular dichroism (XMCD) that both antiferromagnetic and ferromagnetic states can coexist in the 50 nm single-crystalline FeRh thin films on MgO(100) [22]. The interface between FeRh and the capping layer (e.g. MgO or Au) is ferromagnetic at low temperature though the bulk is antiferromagnetic. Photoemission electron microscopy (PEEM) results also confirm the coexistence of both antiferromagnetic and ferromagnetic states in 90 nm single-crystalline FeRh thin film on MgO with a 2.5 nm Al capping layer [23]. The domain structure of the interface between the FeRh and the Al capping layer imaged by PEEM reveals that the ferromagnetic domain nucleation and formation can be driven by temperature. Furthermore, in-plane and out-of-plane magnetic hysteresis loops of a 150 nm single-crystalline FeRh thin film on MgO(100) obtained by vibrating sample magnetometry (VSM) indi-

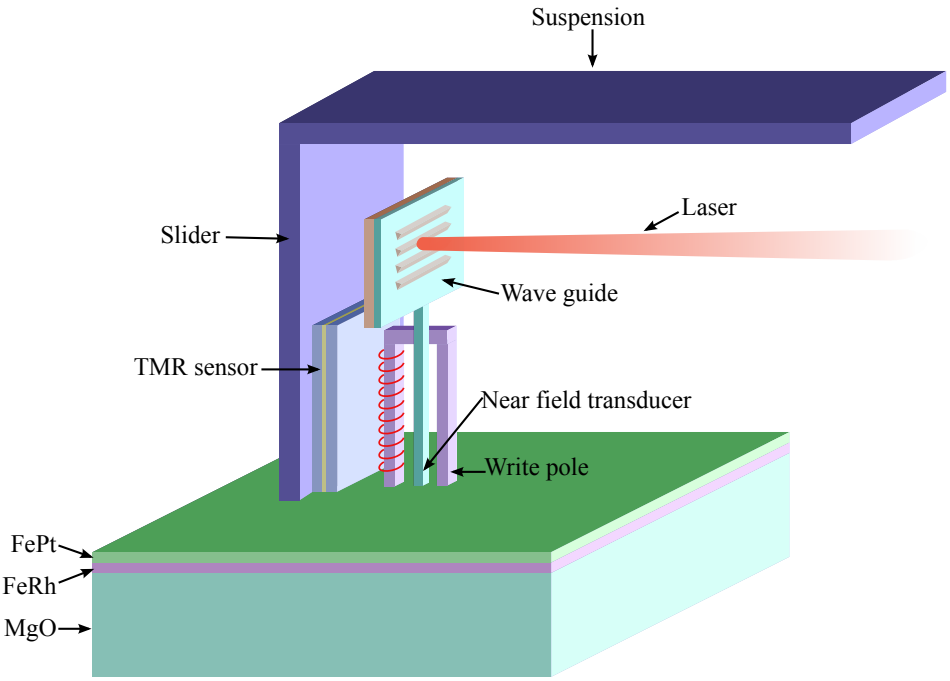

Figure 1.1.: Schematic drawing of a heat-assisted magnetic recording setup based on a medium comprising a FeRh/FePt bi-layer system.

cate that there is a stress-induced magnetic anisotropy in FeRh thin films during first-order phase transition [24]. ^{57}Fe conversion electron Mössbauer spectroscopy (CEMS) results of single-crystalline FeRh thin film on MgO further reveal an Fe spin reorientation from in-plane(out-of-plane) to out-of-plane(in-plane) during the first-order phase transition which is determined by the stress introduced at the FeRh/substrate interface [25].

Obviously, the surface magnetic properties of FeRh thin films can behave differently from the bulk. But up to know, all the works on the surface magnetic properties of FeRh thin films are done with a capping layer (e.g. Au, Al or MgO) or with contaminated or even oxidized surfaces. Since Au, Al, or MgO capping materials can diffuse into FeRh or chemically react with it, the surface magnetic properties of FeRh are inevitably changed by capping layers [26, 27]. This also holds for contaminated and oxidized surfaces.

The motivation for this thesis is to unravel the intrinsic surface magnetic properties of single-crystalline FeRh thin films at temperatures below and above the temperature-induced metamagnetic transition. To this end, the equipment was improved in the course of this work to allow in-situ deposition, characterization, and measurement of thin, uncapped FeRh films by (i) installing a new a multi-pocket e-beam evaporator, (ii) adapting an in-situ magneto-optical Kerr effect (MOKE) set-up, and (iii) updating the analyzer of the scanning electron microscope with

polarization analysis (SEMPA).

Chapter 2 briefly introduces the material FeRh with emphasis on the magnetic moments. An Ising model of FeRh will be given and the approximate solution obtained by mean field theory will be discussed. Finally, the domain theory will be described and the magnetic switching behavior of FeRh/FePt bi-layer system is simulated by micromagnetic theory.

Chapter 3 describes the experimental procedures used in this work. Samples are prepared according to two different procedures. The so-called ex-situ procedure involved two ultra-high vacuum (UHV) systems, one for sample preparation and one for the measurements, whereas for the in-situ procedure, which had to be realized in the course of the work, all required steps from film deposition to magnetic measurements were performed in a single UHV system. Both UHV systems are briefly introduced, and the main measurement techniques are explained in some more detail.

In Chapter 4, both the ex-situ and in-situ sample preparation procedures and the corresponding measurements will be discussed and compared in detail. The major result concerns in situ prepared uncapped FeRh-films and shows clear differences observed between the bulk magnetic properties measured by in-situ MOKE and the intrinsic surface magnetic properties accessed by SEMPA.

Finally, a conclusion will be given in Chapter 5.

2. Fundamentals

After it has been found decades ago that the CsCl-ordered FeRh alloy undergoes a first-order phase transition from antiferromagnetic (AFM) to ferromagnetic (FM) and a second-order phase transition from FM to paramagnetic (PM), many attempts are made in order to understand the temperature-induced metamagnetic transition and the magnetic properties of FeRh system. In this chapter, the magnetic moments of FeRh system are first described. Then the Ising model of FeRh is introduced to describe the temperature-induced metamagnetic transition of FeRh. At last, the magnetic domain theory will be briefly introduced.

2.1. Magnetic moments of FeRh

Typically, a CsCl-ordered FeRh alloy undergoes a first-order transition from AFM to FM state at 350 K and exhibits a second-order transition from FM to PM state at 675 K [16, 17]. Neutron scattering of FeRh shows that the spin configuration is type-II AFM at low temperature and becomes FM if the temperature rises above the critical temperature [28], see Fig. 2.1.

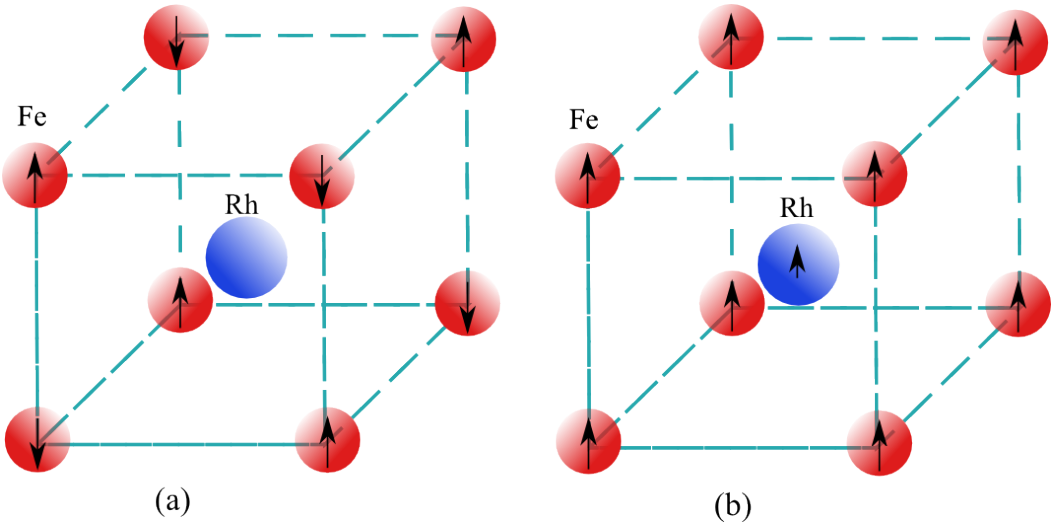

Figure 2.1.: Spin configurations of FeRh: (a) Type-II AFM, (b) FM.

In the AFM state, the Fe atoms have a magnetic moment of about $3\,\mu_B$, while the Rh atoms have no magnetic moment. On the other hand, in the FM state, the Fe atoms still have a magnetic moment around $3\,\mu_B$, while the Rh atoms also have a magnetic moment of about $1\,\mu_B$. This significant increase of the Rh magnetic moment is not associated with a structural change of the FeRh lattice [29, 30]. The lattice constant of the CsCl-structure of FeRh is about 3 Å at room temperature. Ibarra et al. [31] pointed out that there is a total 0.82% volume change of FeRh in the temperature range from 250 to 800 K. In addition, the volume further increases by about 0.1% at the critical transition temperature. Besides, the magnetic moment in the FM state is very sensitive to the stoichiometry, see Fig 2.2. The magnetic moment of Fe-rich and Rh-rich FeRh is measured by Shirane et al. [28] and Hofer et al. [32], respectively. Although the magnetic moment of Fe-rich FeRh alloys at room temperature does not change so much, the first-order transition temperature decreases dramatically. Only when the atomic concentration of Fe is several percent more than 50%, there is no first-order phase transition, and the Fe-rich FeRh alloys become a normal FM material [28]. On the other hand, the average magnetic moment of Rh-rich FeRh alloys at room temperature decreases very fast when the atomic concentration of Rh increases from 50% to 63% (see Fig. 2.2), but the first-order and second-order transition temperatures only change slightly. However, when the Rh concentration exceeds 64%, Rh-rich FeRh alloys become paramagnetic. In this manner both the first-order and the second-order transition temperatures of Rh-rich FeRh alloys suddenly decrease to zero (see Fig. 2.3) [32]. When the atomic concentration of Rh is more than 64%, the FeRh alloys become paramagnetic.

Density functional calculations (DFT) of equiatomic FeRh have been performed

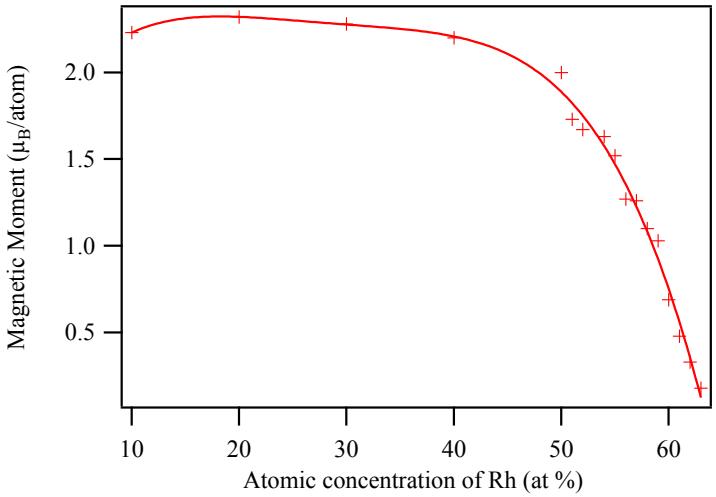

Figure 2.2.: Measured average magnetic moment per atom of FeRh as a function of the atomic concentration of Rh at room temperature [28, 32].

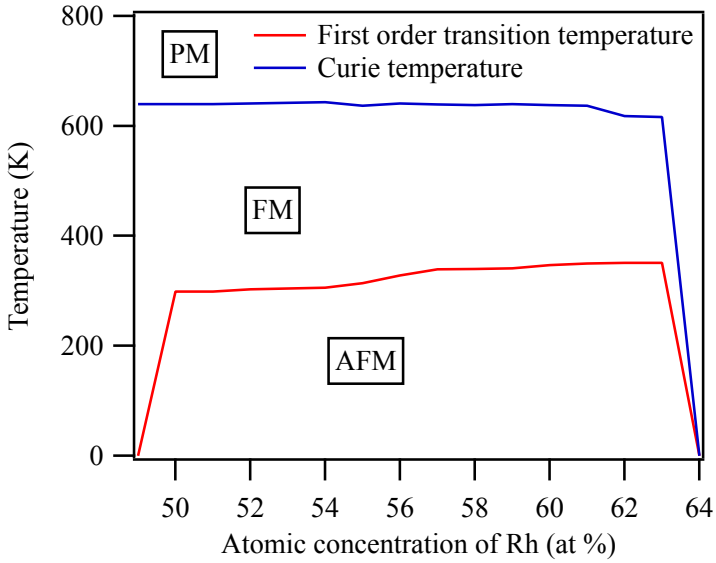

Figure 2.3.: Magnetic transition temperature of Rh-rich FeRh alloy as a function of the atomic concentration of Rh at room temperature [32]. The red line is the first-order magnetic phase transition temperature from AFM to FM, and the blue line is the Curie temperature which is also the second order magnetic phase transition temperature from FM to PM. When Rh is more than 64%,FeRh alloy become paramagnet, in this manner the first-order and the second-order magnetic phase transition is absent and the transition temperature decreases to zero.

by Moruzzi et al. [33] and show that the magnetic moment of equiatomic FeRh in both the FM and the AFM state is not sensitive to the lattice constant, but the ground state of equiatomic FeRh – AFM or FM – strongly depends on the lattice constant, see Fig. 2.4. Figure 2.4 (a) is the magnetic moment of FeRh in the AFM and FM state as a function of lattice constant. Figure 2.4 (b) shows the difference of the average energy per atom between the FM and AFM state. The results show that the energy difference strongly depends on the lattice constant. The energy difference decreases as the lattice constant increases and it changes sign at about 3.096 Å. Normally, the lattice constant of FeRh is about 3 Å and its ground state is AFM ordered. The energy difference between the AFM and FM ordered ground state is only 1.775 mRy. The DFT calculation reveals that the AFM and FM states of FeRh are almost degenerate. Therefore, the magnetic state of FeRh can be changed by adding small energy terms, such as Zeeman energy or strained induced energy. As a result, small changes of the external parameters, such as magnetic field, pressure or temperature, can cause the phase transition of FeRh from AFM to FM.

The DFT calculation results by Sandratskii et al. [34] further reveal that the Rh

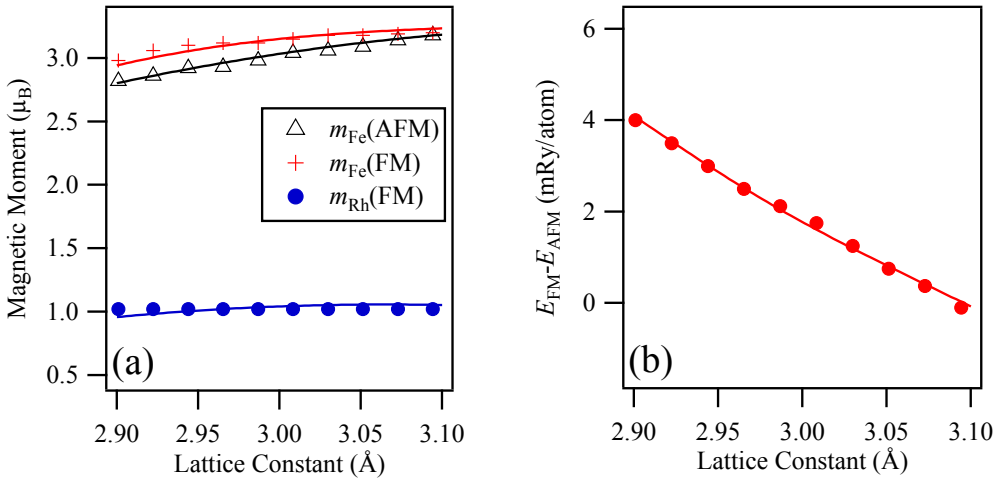

Figure 2.4.: Magnetic moment and the energy difference between FM and AFM as a function of lattice constant [33].

moment is induced by the Fe in the FM state due to strong hybridization between Rh and Fe. They demonstrate that the FM Fe-Rh interaction is robust with respect to the changes of the volume, while the AFM Fe-Fe interaction is strongly volume dependent. Hence, the AFM Fe-Fe interaction plays a key role in the metamagnetic transition of FeRh. If the Fe-Fe interaction can be reduced by the changes of lattice constant due to strain, atomic concentration or other effect, the magnetic properties of FeRh may be strongly changed, particularly the first-order magnetic phase transition from AFM to FM. As anticipated by the DFT calculations, the energy difference between the AFM and FM state is small, thus the AFM state is not robust.

2.2. Mean field approximation of Ising model for FeRh

After the first-order magnetic phase transition of FeRh was discovered, many people attempted to explain the first-order phase transition using various theories. In 1960, Kittel [35] proposed a model of exchange-inversion magnetization to explain the first-order magnetic phase transition from AFM to FM, such as for instance in MnAs. He assumed that the inter-lattice exchange interaction changes sign when the lattice constant increase beyond certain value. But Tu et al. [36] later concluded that the exchange-inversion model was not valid for FeRh because it failed to explain the large total entropy change due to the electronic band structure changes. Although recently DFT calculations can explain the electronic structure changes when FeRh undergons the AFM to FM transition, the DFT calculations can only describe ground state, but not the magnetic transitions at finite temperatures.

The Ising model is a simple model of a many-body system that can be solved analytically on one- and two-dimensional lattices. The basic assumption of the Spin-$\frac{1}{2}$ Ising model is that the spins in a d-dimensional lattice only can take the values +1 or -1 and only nearby spins interact with each other. The Hamiltonian of the Ising model can be expressed as[37]

$$H = -\sum_{<i,j>}^{N} J_{ij} S_i S_j - \mu h \sum_i S_i, \tag{2.1}$$

where J_{ij} are the exchange constants, S_i is the ith spin, and h is the external magnetic field. The symbol $< i, j >$ indicates that the summation is over all pairs of neighbouring spins, N is the total number of the spins of the Ising system. Ising models are widely applied to many problems of statistical physics including the second-order phase transition from FM to PM. However, the Spin-$\frac{1}{2}$ Ising model only shows second-order phase transition, it can not be directly used to explain the first-order transition of FeRh (see Appendix A).

Blume [38] and Capel [39, 40, 41] extended the Ising model to spin triplets ($S = 1$) with zero-field splitting in order to explain the first-order magnetic phase transition of UO_2 from PM to FM. The spin-1 Ising model showed both first-order and second-order magnetic phase transition (see Appendix B). Hence, it is possible to use the spin-1 Ising model to explain the first-order magnetic phase transition of FeRh from AFM to FM. Following the approach of Gruner et al. [42] and Matt et al. [43], the spin-1 Ising model with zero-field splitting of FeRh will be presented here.

2.2.1. Ising model of FeRh

Though the spin-1 Ising model with zero-field splitting that only takes account of the nearest-neighbour (NN) interactions shows first-order magnetic phase transitions from FM to PM or AFM to PM, which, however, are different from the transition of FeRh. Hence, the standard spin-1 Ising model will be extended here for FeRh including the next-nearest-neighbour (NNN) interaction.

Taking into account both NN and NNN interactions, the Hamiltonian of spin-1 Ising model with zero-field splitting is

$$H = \sum_i D_i S_i^2 - \sum_{<NN,NNN>} J_{ij} S_i S_j, \tag{2.2}$$

where D is the zero-field splitting, S is the spin, which only can take three values $(0, \pm 1)$.

Based on the DFT calculations (see Section 2.1), we make the following assumptions to simplify the Hamiltonian of the Ising model for FeRh:

1. $J_{\mathrm{RhRh}} = 0$: The nearest neighbour of each Rh atom are Fe atoms. Thus, $J_{\mathrm{RhRh}} = 0$ is the next-nearest interaction. Compared to the Fe-Rh interaction, the Rh-Rh interaction is much smaller, especially in the ground state when the magnetic moment of Rh is zero. Hence, the next-nearest neighbour interaction of Rh can be neglected.

2. $S_{\mathrm{Fe}} \in \{\pm 1\}$: Because the magnetic moments of Fe atoms at in both the AFM and the FM state are about $3\,\mu_B$, the singlet energy level of Fe atoms is much higher than the doublet energy level. The zero-field splitting $D_{\mathrm{Fe}} \ll 0$. As a result, the possibility of $S_{\mathrm{Fe}} = 0$ is so small that it can be neglect.

3. The zero-field splitting of Rh in the AFM state is different from that in the FM state. In ground state, FeRh is AFM and the magnetic moment of Rh is zero. The singlet energy level of Rh is much lower than the doublet, hence, $D_{\mathrm{Rh}} \gg 0$. As a result, $S_{\mathrm{Rh}} = 0$ is the only possible spin configuration of Rh. On the other hand, in the FM state, all Fe magnetic moments align in the same direction, the energy level of both Rh singlet and doublet can be changed due to strong Fe-Rh interaction. If D_{Rh} becomes smaller in the FM state, then $S_{\mathrm{Rh}} = \pm 1$ are also possible spin configurations.

4. The correlation between the atoms can be neglected. This is the basic assumption of the mean field theory. Since the exact partition function is difficult to obtain, mean field theory will be used to solve the problem. Under the mean field approximation, Rh and Fe atoms can be treated independently. Hence, we can calculate the Hamiltonian of Fe and Rh atoms separately.

According to the above assumptions, the Hamiltonian of FeRh is

$$H = \sum D_{\mathrm{Rh}} S_{\mathrm{Rh}_i}^2 - \sum_{NN} J_{\mathrm{FeRh}} S_{\mathrm{Fe}_i} S_{\mathrm{Rh}_j} - \sum_{NNN} J_{\mathrm{FeFe}} S_{\mathrm{Fe}_i} S_{\mathrm{Fe}_j}. \tag{2.3}$$

Ferromagnetic Ising model of FeRh

At first, the ferromagnetic state of FeRh will be considered. In the ferromagnetic state, the lattice needs not to be decomposed into two sub-lattices. Under the mean field approximation, the Fe atoms and the Rh atoms are assumed to be independent, we can express the single spin density matrix of Fe and Rh as

$$\rho_{\mathrm{Fe}} = \frac{\exp\left[-H_{\mathrm{Fe}}/(k_B T)\right]}{\mathrm{Tr}\exp\left[-H_{\mathrm{Fe}}/(k_B T)\right]} \tag{2.4a}$$

$$\rho_{\mathrm{Rh}} = \frac{\exp\left[-H_{\mathrm{Rh}}/(k_B T)\right]}{\mathrm{Tr}\exp\left[-H_{\mathrm{Rh}}/(k_B T)\right]}. \tag{2.4b}$$

Under the mean field approximation, the Hamiltonian of a particular Fe and Rh

atoms can be calculated as

$$H_{\mathrm{Fe}} = -(z_{\mathrm{FeFe}} J_{\mathrm{FeFe}} m_{\mathrm{Fe}} + z_{\mathrm{FeRh}} J_{\mathrm{FeRh}} m_{\mathrm{Rh}}) S_{\mathrm{Fe}} \tag{2.5a}$$

$$H_{\mathrm{Rh}} = D_{\mathrm{Rh}} S_{\mathrm{Rh}}^2 - z_{\mathrm{FeRh}} J_{\mathrm{FeRh}} m_{\mathrm{Fe}} S_{\mathrm{Rh}}, \tag{2.5b}$$

where $z_{FeFe} = 6$ is the number of a Fe atom's next-nearest Fe neighbours, $z_{FeRh} = 8$ is the number of a Fe or Rh atom's nearest Rh or Fe neighbours. S_{Fe} and S_{Rh} can be expressed in the form of diagonal matrices

$$S_{\mathrm{Fe}} = \begin{pmatrix} 1 & 0 \\ 0 & -1 \end{pmatrix} \tag{2.6a}$$

$$S_{\mathrm{Rh}} = \begin{pmatrix} 1 & 0 & 0 \\ 0 & 0 & 0 \\ 0 & 0 & -1 \end{pmatrix}. \tag{2.6b}$$

As a result, we can also obtain an expression of the average free energy

$$\begin{aligned} F &= F_{\mathrm{Fe}} + F_{\mathrm{Rh}} \\ &= D_{\mathrm{Rh}} \mathrm{Tr}\rho_{\mathrm{Rh}} S_{\mathrm{Rh}}^2 - z_{\mathrm{FeRh}} J_{\mathrm{FeRh}} (\mathrm{Tr}\rho_{\mathrm{Fe}} S_{\mathrm{Fe}})(\mathrm{Tr}\rho_{\mathrm{Rh}} S_{\mathrm{Rh}}) \\ &\quad - \frac{1}{2} z_{\mathrm{FeFe}} J_{\mathrm{FeFe}} (\mathrm{Tr}\rho_{\mathrm{Fe}} S_{\mathrm{Fe}})^2 \\ &\quad - k_B T \mathrm{Tr}\rho_{\mathrm{Fe}} \ln \rho_{\mathrm{Fe}} - k_B T \mathrm{Tr}\rho_{\mathrm{Rh}} \ln \rho_{\mathrm{Rh}}. \end{aligned} \tag{2.7}$$

Substituting Eqs. (2.4) and Eqs. (2.6) into the Eq. (2.7), we could obtain the expression of the average free energy as

$$\begin{aligned} F =& \frac{1}{2} z_{\mathrm{FeFe}} J_{\mathrm{FeFe}} m_{\mathrm{Fe}}^2 + z_{\mathrm{FeRh}} J_{\mathrm{FeRh}} m_{\mathrm{Rh}} m_{\mathrm{Fe}} \\ &- k_B T \ln \left\{ 2 \cosh \left(\frac{z_{\mathrm{FeFe}} J_{\mathrm{FeFe}} m_{\mathrm{Fe}} + z_{\mathrm{FeRh}} J_{\mathrm{FeRh}} m_{\mathrm{Rh}}}{k_B T} \right) \right\} \\ &- k_B T \ln \left\{ \left[1 + 2 \exp\left(- \frac{D}{k_B T} \right) \cosh \left(\frac{z_{\mathrm{FeRh}} J_{\mathrm{FeRh}} m_{\mathrm{Fe}}}{k_B T} \right) \right] \right\}. \end{aligned} \tag{2.8}$$

According to the assumptions, the magnetizations of Fe and Rh are the expectation values of S_{Fe} and S_{Rh}, respectively, which can be expressed as

$$m_{\mathrm{Fe}} = \mathrm{Tr}\{\rho_{\mathrm{Fe}} S_{\mathrm{Fe}}\} \tag{2.9a}$$

$$m_{\mathrm{Rh}} = \mathrm{Tr}\{\rho_{\mathrm{Rh}} S_{\mathrm{Rh}}\}. \tag{2.9b}$$

Substituting Eqs. (2.4), Eqs. (2.5) and Eqs. (2.6) into Eqs. (2.9), we obtain m_{Fe} and m_{Rh} as

$$m_{\mathrm{Fe}} = \tanh\left[(z_{\mathrm{FeFe}} J_{\mathrm{FeFe}} m_{\mathrm{Fe}} + z_{\mathrm{FeRh}} J_{\mathrm{FeRh}} m_{\mathrm{Rh}}) / (k_B T) \right] \tag{2.10a}$$

$$m_{\mathrm{Rh}} = \frac{2 \sinh\left[z_{\mathrm{FeRh}} J_{\mathrm{FeRh}} m_{\mathrm{Fe}} / (k_B T) \right]}{\exp[D/(k_B T)] + 2 \cosh\left[z_{\mathrm{FeRh}} J_{\mathrm{FeRh}} m_{\mathrm{Fe}} / (k_B T) \right]}. \tag{2.10b}$$

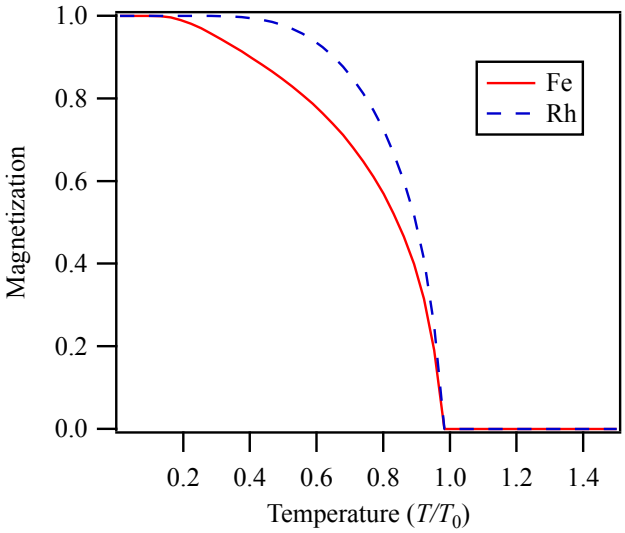

Figure 2.5.: Temperature dependence of magnetizations of the Fe and Rh sublattices for $\delta = -1$, $\epsilon = -1.5$, $T_0 = (z_{\mathrm{FeFe}}|J_{\mathrm{FeFe}}|)/k_B$.

Obviously, Eqs. (2.10) have at lest one solution, which is $m_{\mathrm{Fe}} = 0$ and $m_{\mathrm{Rh}} = 0$.

If we define the dimensionless parameters $T' = T/T_0$ with unit temperature $T_0 = (z_{\mathrm{FeFe}}|J_{\mathrm{FeFe}}|)/k_B$, $\delta = D/(z_{\mathrm{FeFe}}|J_{\mathrm{FeFe}}|)$, and $\epsilon = z_{\mathrm{FeRh}}J_{\mathrm{FeRh}}/z_{\mathrm{FeFe}}J_{\mathrm{FeFe}}$, then we can rewrite Eqs. (2.10) as

$$m_{\mathrm{Fe}} = \mathrm{sgn}(J_{\mathrm{FeFe}}) \tanh\left[(m_{\mathrm{Fe}} + \epsilon m_{\mathrm{Rh}})/T'\right] \tag{2.11a}$$

$$m_{\mathrm{Rh}} = \mathrm{sgn}(J_{\mathrm{FeFe}}) \frac{2\sinh\left(\epsilon m_{\mathrm{Fe}}/T'\right)}{\exp(\delta/T') + 2\cosh\left(\epsilon m_{\mathrm{Fe}}/T'\right)}, \tag{2.11b}$$

where $\mathrm{sgn}(x)$ is the sign function. Except the trivial zero solution, the nonzero solutions need to be solved numerically. Figure 2.5 shows the magnetization of Fe and Rh for $\delta = -1$, $\epsilon = -1.5$ as a function of temperature. Although the magnetization of Fe does not have the same slope as Rh, both decrease to zero as the temperature reaches the Curie temperature T_{C}. Further numerical results reveal that the Curie temperature strongly depends on the δ and ϵ. With different parameters, T_{C} can be larger or smaller than T_{N}.

In order to figure out how the parameters affect the transition temperature, the magnetization behavior both in the ground state and at the critical temperature will be analyzed.

In the ground state, when $T \to 0$, Eqs. (2.10) become

$$\lim_{T'\to 0} m_{\mathrm{Fe}} = \lim_{T'\to 0} \mathrm{sgn}(J_{\mathrm{FeFe}})\mathrm{sgn}\left(m_{\mathrm{Fe}} + \epsilon m_{\mathrm{Rh}}\right) \tag{2.12a}$$

$$\lim_{T'\to 0} m_{\mathrm{Rh}} = \lim_{T'\to 0} \mathrm{sgn}(J_{\mathrm{FeRh}} m_{\mathrm{Fe}}) \frac{2}{\exp\left[(\delta - |\epsilon m_{\mathrm{Fe}}|)/T'\right] + 2}. \tag{2.12b}$$

Equations (2.12) indicate that the magnetization of Fe and Rh only have three possible solutions, which are $\pm 1, 0$ in the ground state. Depending on the values of ϵ and δ and the sign of J_{FeFe} and J_{FeRh}, Eqs. (2.12) may have different solutions. As Eqs. (2.12) are an odd functions, we only discuss the case for $m_{\mathrm{Fe}} = 1$. The possible nonzero solutions and the conditions are shown in Table 2.1. Actually, when $J_{\mathrm{FeRh}} < 0$, although there are nonzero solutions, m_{Fe} and m_{Rh} always have opposite signs, which corresponds a ferrimagnetic state.

If the Ising system of FeRh has a second-order transition, there should exist a critical temperature $T_{c2_{\mathrm{FM}}}$, for which $\lim_{T\to T_{c2_{\mathrm{FM}}}} m_{\mathrm{Fe}} \to 0$ and $\lim_{T\to T_{c2_{\mathrm{FM}}}} m_{\mathrm{Rh}} \to 0$. For small m_{Fe} and m_{Rh}, Eqs. (2.10) can be approximated by

$$m_{\mathrm{Fe}} = \mathrm{sgn}(J_{\mathrm{FeFe}})(m_{\mathrm{Fe}} + \epsilon m_{\mathrm{Rh}})/T' \tag{2.13a}$$

$$m_{\mathrm{Rh}} = \mathrm{sgn}(J_{\mathrm{FeFe}}) \frac{2\epsilon m_{\mathrm{Fe}}/T'}{\exp(\delta/T') + 2}. \tag{2.13b}$$

Substituting Eq. (2.13b) into Eq. (2.13a), we have

$$T'^2 - \mathrm{sgn}(J_{\mathrm{FeFe}})T' = \frac{\epsilon^2}{\frac{1}{2}\exp(\frac{\delta}{T'}) + 1}. \tag{2.14}$$

When $J_{\mathrm{FeRh}} > 0$, $J_{\mathrm{FeFe}} < 0$, and $\delta < 0$, Eq. (2.14) always has one nonzero solution $(\frac{1}{2} + \sqrt{\frac{2}{3}\epsilon^2 + \frac{1}{4}})T_0 < T_{c2_{\mathrm{FM}}} < (\frac{1}{2} + \sqrt{\epsilon^2 + \frac{1}{4}})T_0$. The Curie temperature strongly depends on δ and ϵ. The numerical solution of Eq. (2.14) is shown in Figure 2.6 as a contour plot of the temperature T/T_0 as a function of $0 < \delta < 1$ and $-2 < \epsilon < -1$. The numerical results indicate that as the zero-field splitting decreases, the Curie temperature will increase. This means that the Curie temperature increases when the energy level of the Rh singlet decreases. At the same time, if the FM coupling between Fe and Rh becomes stronger than the AFM coupling between Fe atoms, the Curie temperature also increases.

Table 2.1.: The nonzero solutions and the conditions of ferromagnetic Ising model of FeRh.

solutions		conditions	
$m_{\mathrm{Fe}} = 1$	$m_{\mathrm{Rh}} = 0$	$\delta > \lvert\epsilon\rvert$, $J_{\mathrm{FeFe}} > 0$	
$m_{\mathrm{Fe}} = 1$	$m_{\mathrm{Rh}} = -1$	$\delta < \lvert\epsilon\rvert$, $J_{\mathrm{FeRh}} < 0$	$\epsilon > 1$
			$\epsilon < 0$
$m_{\mathrm{Fe}} = 1$	$m_{\mathrm{Rh}} = 1$	$\delta < \lvert\epsilon\rvert$, $J_{\mathrm{FeRh}} > 0$	$\epsilon > 0$
			$\epsilon < -1$

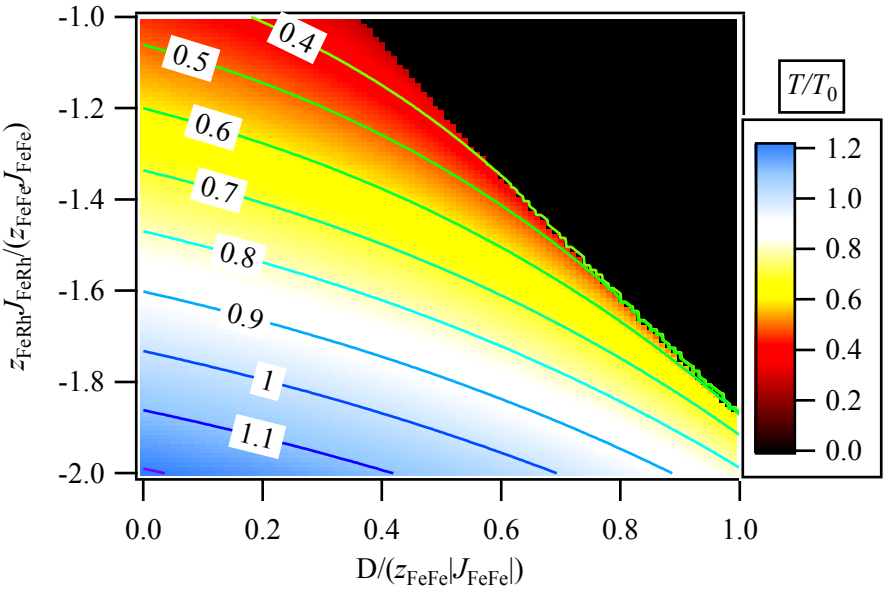

Figure 2.6.: The Curie temperature of ferromagnetic Ising model of FeRh as a function of $\delta = D/(z_{\mathrm{FeFe}}|J_{\mathrm{FeFe}}|)$, $\epsilon = z_{\mathrm{FeRh}}J_{\mathrm{FeRh}}/z_{\mathrm{FeFe}}J_{\mathrm{FeFe}}$ and $T_0 = (z_{\mathrm{FeFe}}|J_{\mathrm{FeFe}}|)/k_B$.

Antiferromagnetic Ising model of FeRh

For the antiferromagnetic Ising model of FeRh, we need to decompose the lattice into two sub-lattices A and B (see Fig. B.6). Each sub-lattice contains one Fe and one Rh atom per unit cell.

Similar to the spin-1 antiferromagnetic Ising model, we can express the single-spin density of Fe and Rh in sub-lattices A and B as

$$\rho_{\mathrm{Fe}_A} = \frac{\exp\left[-H_{\mathrm{Fe}_A}/(k_BT)\right]}{\mathrm{Tr}\exp\left[-H_{\mathrm{Fe}_A}/(k_BT)\right]} \tag{2.15a}$$

$$\rho_{\mathrm{Fe}_B} = \frac{\exp\left[-H_{\mathrm{Fe}_B}/(k_BT)\right]}{\mathrm{Tr}\exp\left[-H_{\mathrm{Fe}_B}/(k_BT)\right]} \tag{2.15b}$$

$$\rho_{\mathrm{Rh}} = \frac{\exp\left[-H_{\mathrm{Rh}}/(k_BT)\right]}{\mathrm{Tr}\exp\left[-H_{\mathrm{Rh}}/(k_BT)\right]}. \tag{2.15c}$$

Using the mean field approximation, the Hamiltonian of Fe_A, Fe_B and Rh atoms can be expressed as

$$H_{\mathrm{Fe}_A} = -(z_{\mathrm{FeFe}}J_{\mathrm{FeFe}}m_{\mathrm{Fe}_B} + z_{\mathrm{FeRh}}J_{\mathrm{FeRh}}m_{\mathrm{Rh}})S_{\mathrm{Fe}_A} \tag{2.16a}$$

$$H_{\mathrm{Fe}_B} = -(z_{\mathrm{FeFe}}J_{\mathrm{FeFe}}m_{\mathrm{Fe}_A} + z_{\mathrm{FeRh}}J_{\mathrm{FeRh}}m_{\mathrm{Rh}})S_{\mathrm{Fe}_B} \tag{2.16b}$$

$$H_{\mathrm{Rh}} = DS_{\mathrm{Rh}}^2 - \frac{1}{2}z_{\mathrm{FeRh}}J_{\mathrm{FeRh}}(m_{\mathrm{Fe}_A} + m_{\mathrm{Fe}_B})S_{\mathrm{Rh}} \tag{2.16c}$$

Then the average free energy per cell is

$$\begin{aligned} F =& \frac{1}{2} z_{\mathrm{FeFe}} J_{\mathrm{FeFe}} m_{\mathrm{Fe}_A} m_{\mathrm{Fe}_B} - \frac{1}{2} k_B T \ln \left\{ 2 \cosh \left(\frac{z_{\mathrm{FeFe}} J_{\mathrm{FeFe}} m_{\mathrm{Fe}_A} + z_{\mathrm{FeRh}} J_{\mathrm{FeRh}} m_{\mathrm{Rh}}}{k_B T} \right) \right\} \\ & - \frac{1}{2} k_B T \ln \left\{ 2 \cosh \left(\frac{z_{\mathrm{FeFe}} J_{\mathrm{FeFe}} m_{\mathrm{Fe}_B} + z_{\mathrm{FeRh}} J_{\mathrm{FeRh}} m_{\mathrm{Rh}}}{k_B T} \right) \right\} \\ & - k_B T \ln \left\{ 2 \cosh \left[\frac{z_{\mathrm{FeRh}} J_{\mathrm{FeRh}} (m_{\mathrm{Fe}_A} + m_{\mathrm{Fe}_B})}{2 k_B T} \right] \right\}. \end{aligned} \tag{2.17}$$

The magnetizations m_{Fe_A}, m_{Fe_B} and m_{Rh}, which are the expectation values of S_{Fe_A}, S_{Fe_B} and S_{Rh}, can be calculated as

$$m_{\mathrm{Fe}_A} = \tanh \left(\frac{z_{\mathrm{FeFe}} J_{\mathrm{FeFe}} m_{\mathrm{Fe}_B} + z_{\mathrm{FeRh}} J_{\mathrm{FeRh}} m_{\mathrm{Rh}}}{k_B T} \right) \tag{2.18a}$$

$$m_{\mathrm{Fe}_B} = \tanh \left(\frac{z_{\mathrm{FeFe}} J_{\mathrm{FeFe}} m_{\mathrm{Fe}_A} + z_{\mathrm{FeRh}} J_{\mathrm{FeRh}} m_{\mathrm{Rh}}}{k_B T} \right) \tag{2.18b}$$

$$m_{\mathrm{Rh}} = \frac{2 \sinh \left[z_{\mathrm{FeRh}} J_{\mathrm{FeRh}} (m_{\mathrm{Fe}_A} + m_{\mathrm{Fe}_B}) / (2 k_B T) \right]}{\exp[D/(k_B T)] + 2 \cosh \left[z_{\mathrm{FeRh}} J_{\mathrm{FeRh}} (m_{\mathrm{Fe}_A} + m_{\mathrm{Fe}_B}) / (2 k_B T) \right]}. \tag{2.18c}$$

When $D \ll 0$, we obtain

$$m_{\mathrm{Rh}} \cong 0. \tag{2.19}$$

When $m_{\mathrm{Rh}} = 0$, we only can obtain the AFM state if $J_{\mathrm{FeFe}} < 0$, which corresponds to AFM coupling between the Fe atoms. In this case, the spin-1 Ising model of FeRh degenerates to the antiferromagnetic spin-$\frac{1}{2}$ Ising model. Defining the dimensionless temperature $T' = T/T_{\mathrm{N}}$ with unit temperature $T_{\mathrm{N}} = z_{\mathrm{FeFe}} |J_{\mathrm{FeFe}}| / k_B T$, then substituting $m_{\mathrm{Rh}} = 0$ into Eqs. (2.18), we have

$$m_{\mathrm{Fe}_A} = -\tanh \left(\frac{m_{\mathrm{Fe}_B}}{T'} \right) \tag{2.20a}$$

$$m_{\mathrm{Fe}_B} = -\tanh \left(\frac{m_{\mathrm{Fe}_A}}{T'} \right). \tag{2.20b}$$

Obviously, $m_{\mathrm{Fe}_A} = m_{\mathrm{Fe}_B} = 0$ is always a solution of Eqs. (2.20). The nonzero solutions of Eqs. (2.20) can be obtained numerically as shown in Fig. 2.7. In the AFM state of FeRh, $m_{\mathrm{Fe}_A} = -m_{\mathrm{Fe}_B}$, and $m_{\mathrm{Rh}} = 0$. In the ground state, when $T \to 0$, m_{Fe_A} and m_{Fe_B} have two nonzero solution. One is $m_{\mathrm{Fe}_A} = 1$ and $m_{\mathrm{Fe}_B s} = -1$, the other one is $m_{\mathrm{Fe}_A} = -1$ and $m_{\mathrm{Fe}_B} = 1$. In addition, the antiferromagnetic Ising system of FeRh has a second-order transition from AFM order to disorder. The transition temperature is $T_{\mathrm{N}} = z_{\mathrm{FeFe}} |J_{\mathrm{FeFe}}| / k_B$.

2.2.2. First-order magnetic transition for the Ising model of FeRh

To describe the first-order magnetic transition of FeRh, we not only need to calculate the temperature dependence of the magnetization but also the free energy

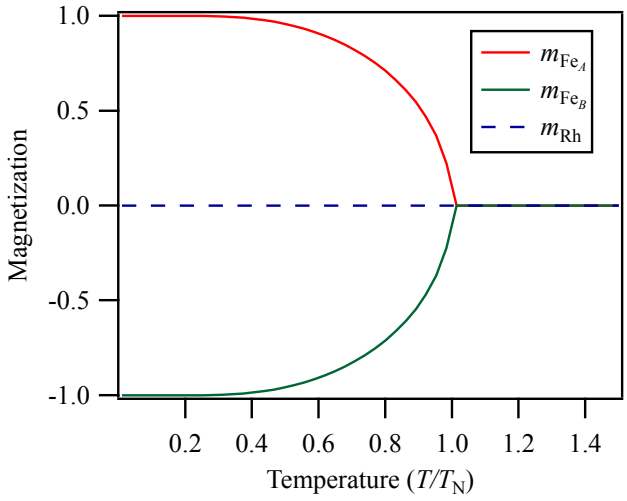

Figure 2.7.: Temperature dependence of the magnetizations of Fe and Rh in the AFM state. $T_N = (z_{FeFe}|J_{FeFe}|)/k_B$ is the Néel temperature.

of the system in order to determine the stable magnetic state. In addition, the ferromagnetic Ising model of FeRh can be treated as the special case of the antiferromagnetic Ising model with $m_{Fe_A} = m_{Fe_B}$.

Recalling Eq. (2.17) and substituting $m_{Fe_A} = -m_{Fe_B} = m_{Fe}$ we get

$$F_{AFM} = -\frac{1}{2} z_{FeFe} J_{FeFe} m_{Fe}^2 - k_B T \ln \left\{ 2 \cosh \left(\frac{z_{FeFe} J_{FeFe} m_{Fe}}{k_B T} \right) \right\}. \tag{2.21}$$

Because FeRh can be in both the AFM and the FM state, $J_{FeFe} < 0$ and $\epsilon < -1$ are required. With the dimensionless parameters $T' = k_B T/(z_{FeFe}|J_{FeFe}|)$, $\delta = D/(z_{FeFe}|J_{FeFe}|)$, and $\epsilon = z_{FeRh} J_{FeRh}/z_{FeFe} J_{FeFe}$, $\Phi = F/(z_{FeFe}|J_{FeFe}|)$, the above equation becomes

$$\Phi_{AFM}(m_{Fe}, T') = \frac{1}{2} m_{Fe}^2 - T' \ln \left[2 \cosh \left(\frac{m_{Fe}}{T'} \right) \right]. \tag{2.22}$$

In the ground state, for $T' \to 0^+$, we have

$$\lim_{T' \to 0^+} \Phi_{AFM}(0, T') = 0 \tag{2.23a}$$

$$\lim_{T' \to 0^+} \Phi_{AFM}(1, T') = -\frac{1}{2}. \tag{2.23b}$$

Because $\lim_{T' \to 0^+} \Phi_{AFM}(1, T') < \lim_{T' \to 0^+} \Phi_{AFM}(0, T')$, $m_{Fe_A} = -m_{Fe_B} = 1$ and $m_{Rh} = 0$ is the ground state for antiferromagnetic Ising model of FeRh for all parameters.

Substituting $m_{\mathrm{Fe}_A} = m_{\mathrm{Fe}_B} = m_{\mathrm{Fe}}$ into Eq. (2.17) and using the dimensionless parameters, we have

$$\begin{aligned}\Phi_{\mathrm{FM}}(m_{\mathrm{Fe}}, m_{\mathrm{Rh}}, T') = &-\frac{1}{2}m_{\mathrm{Fe}}^2 - \epsilon m_{\mathrm{Fe}} m_{\mathrm{Rh}} - T' \ln\Big[2\cosh\big(\frac{m_{\mathrm{Fe}} + \epsilon m_{\mathrm{Rh}}}{T'}\big)\Big] \\ &- T\ln\Big[1 + 2\exp\big(-\frac{\delta}{T'}\big)\cosh\big(\frac{\epsilon m_{\mathrm{Fe}}}{T'}\big)\Big] \end{aligned} \tag{2.24}$$

when $T' \to 0^+$. The conditions for the ferromagnetic Ising model of FeRh to have nonzero solutions are $\epsilon < -1$ and $\delta < |\epsilon|$. Thus,

$$\lim_{T'\to 0^+} \Phi_{\mathrm{FM}}(0,0,T') = \begin{cases} 0 & \delta \geqslant 0 \\ \delta & \delta < 0 \end{cases} \tag{2.25a}$$

$$\lim_{T'\to 0^+} \Phi_{\mathrm{FM}}(1,1,T') = \frac{1}{2} + \epsilon + \delta. \tag{2.25b}$$

If a nonzero solution is a stable solution in the ground state, its free energy should be lower than for the zero solution. Hence, we have

$$\lim_{T'\to 0^+} \Phi_{\mathrm{FM}}(1,1,T') < \lim_{T'\to 0^+} \Phi_{\mathrm{FM}}(0,0,T'). \tag{2.26}$$

As a result, we obtain $\delta < -1/2 - \epsilon$.

Because the ground state of FeRh is antiferromagnetic, we have

$$\lim_{T'\to 0^+} \Phi_{\mathrm{AFM}}(1,T') < \lim_{T'\to 0^+} \Phi_{\mathrm{FM}}(1,1,T'). \tag{2.27}$$

Substituting Eq. (2.23b) and Eq. (2.25b) into Eq. (2.27), we obtain $\epsilon + \delta > -1$. Therefore, the condition to have a stable AFM state of FeRh is $-\epsilon - 1 < \delta < -\epsilon - \frac{1}{2}$. Besides, since $\epsilon < -1$, δ should be larger than 0.

If the Ising system of FeRh can undergo a first-order magnetic transition from AFM to FM, there should exist a critical temperature T_{c1} with $T_{c1} < T_{\mathrm{N}}$ and $T_{c1} < T_{\mathrm{C}}$. If $T > T_{c1}$ and $F_{\mathrm{AFM}} > F_{\mathrm{FM}}$, then the FM state is the stable state. Because the free energy is analytic with respective to T, we can obtained the critical temperature by solving the equation $\Phi_{\mathrm{AFM}}(T') = \Phi_{\mathrm{FM}}(T')$. For given parameters T_{N}, δ, and ϵ, we obtain the magnetizations of both the FM and AFM state at a particular temperature $T' = T/T_{\mathrm{N}}$ by solving the Eqs. (2.10) and Eqs. (2.20). Then substituting the magnetizations of both states into Eq. (2.24) and Eq. (2.22), we obtain the free energy at T'. Comparing the two free energies, we can determine the first-order transition temperature T_{c1}.

Finally, we get the first-order phase transition temperature as a function of δ and ϵ numerically as shown in Fig. 2.8. The black colored regions shows no first-order phase transition, while the colorful region shows a first-order phase transition. The first-order transition only exists in a small region. And the first-order transition temperature decreases dramatically when δ or ϵ decreases.

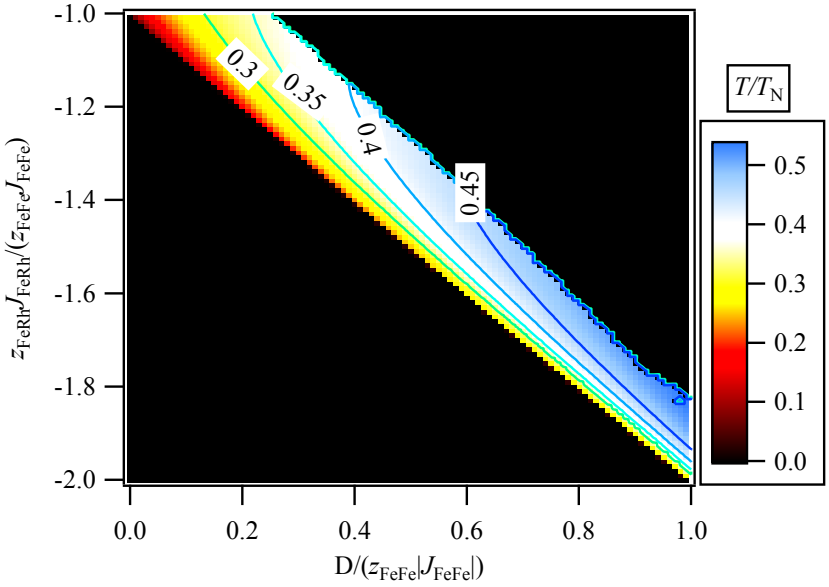

Figure 2.8.: First-order transition temperature of Ising model of FeRh as a function of δ and ϵ.

On the other hand, if we know the first-order transition temperature and the Curie temperature, we can estimate δ and ϵ numerically. For example, if T_{c1} is 316 K and T_C is 667 K for $Fe_{49}Rh_{51}$ [44], then possible values are $\delta = 0.5254$ and $\epsilon = -1.5$. Numerical results for the free energy and the magnetization using these values are shown in Fig. 2.9.

The blue lines show the free energy, and the red lines correspond to the magnetization. The free energy curves show that at $T = 0$ the AFM state has the lower free energy. But there is a critical temperature $T_{c1} = 0.3043 T_N$, above which the FM state has the lower free energy. Because the magnetization changes at T_{c1} discontinuously, the transition from AFM to FM is first-order. If the temperature increases further, the magnetization will continuously decrease to zero. This is a second-order phase transition from FM to disordered. The Curie temperature is equal to $0.6423 T_N$ as obtained numerically from Eq. (2.10). Hence, we can estimate the Néel temperature from the Curie temperature and get 1038 K, which is much higher than the Curie temperature.

Now, we can calculate the exchange constant and the zero-field splitting as

$$J_{FeFe} = -\frac{k_B T_N}{z_{FeFe}} = -1.10 \text{ mRy} \tag{2.28a}$$

$$J_{FeRh} = \frac{z_{FeFe} J_{FeFe}}{z_{FeRh}} \epsilon = 1.23 \text{ mRy} \tag{2.28b}$$

$$D = z_{FeFe} |J_{FeFe}| \delta = 3.45 \text{ mRy}. \tag{2.28c}$$

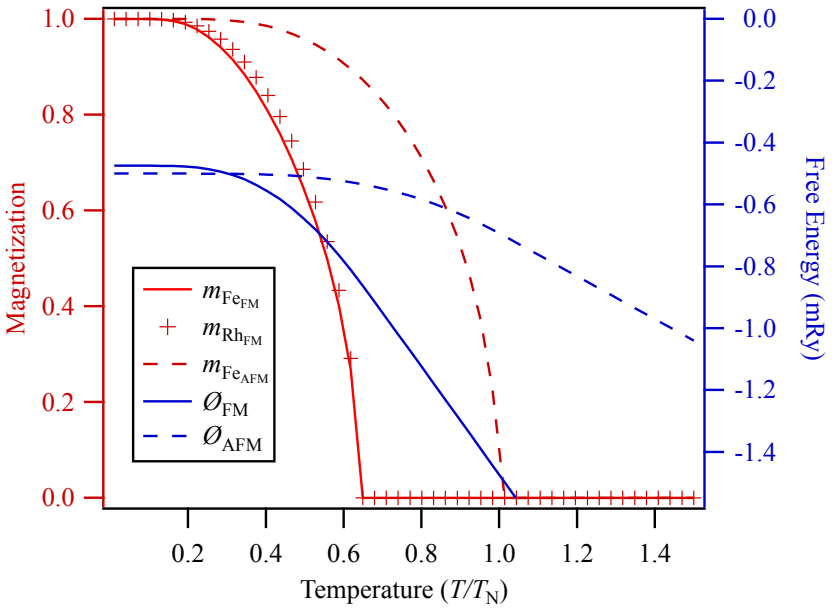

Figure 2.9.: Temperature dependence of the magnetization and the free energy for both the FM and AFM state, calculated for $\delta = 0.5254$ and $\epsilon = -1.5$.

The FM Fe-Rh exchange energy obtained here is in quite good agreement with the DFT calculation result given by Sandratskii et at. [34], but the absolute value of AFM Fe-Fe exchange energy is several times larger.

Under the mean field approximation, we can calculate the energy levels of the Rh atoms with a particular spin value at zero temperature using the above results. Since according to Blume's explanation of the zero-field splitting [38] $D/(z_{\mathrm{FeRh}} J_{\mathrm{FeRh}}) = 0.35$, the energy level of the Rh singlet lies between the energy levels of the doublet as shown in Fig. 2.10. This zero-field splitting may be due to the exchange interaction between Fe and Rh atoms.

From the DFT calculations in Section 2.1 we know that the magnetic moments of FM FeRh at $T = 0$ are $m_{\mathrm{Fe}} = 3.2265\,\mu_B$ and $m_{\mathrm{Rh}} = 0.9837\,\mu_B$. We can obtain the magnetization as a function of temperature as shown in Figure 2.11. In the ground state, since FeRh is AFM, the macroscopic magnetization is zero. When FeRh undergoes the first-order magnetic transition from AFM to FM, the magnetization suddenly increases from zero to 1.34×10^6 A/m. As the temperature continuously increases, the magnetization will also continuously decrease to zero.

Furthermore, Sandratskii et al. [34] indicate that the AFM Fe-Fe interaction is not robust with respect to the volume variation in contrast to the FM Fe-Rh interaction. In our model, we can calculate the change of magnetization when J_{FeFe} changes and obtain the phase diagram of FeRh, which is shown in Fig. 2.12.

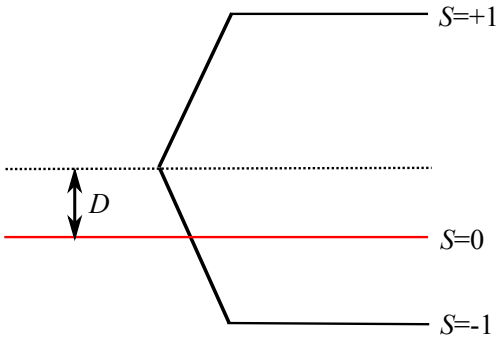

Figure 2.10.: Proposed energy level diagram of the Rh atoms in the FM state. The singlet level is lying between the doublet levels.

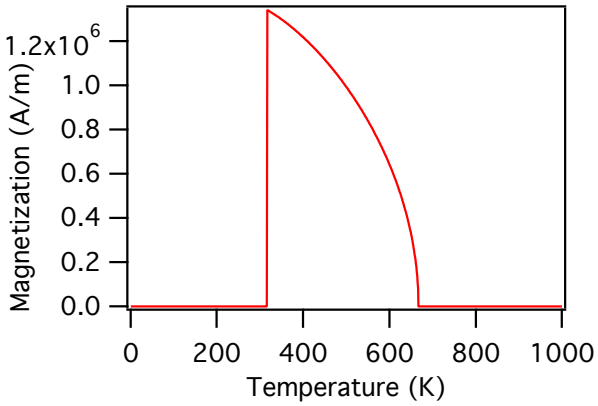

Figure 2.11.: Magnetization of FeRh as a function of temperature.

From the change of magnetization, we could further obtain the first-order transition temperature (see the red line in Fig. 2.12) and the second-order transition temperature (see the blue line in Fig. 2.12). When the AFM Fe-Fe interaction becomes stronger, the absolute value of $|J_{\mathrm{FeFe}}|$ increases, the first-oder transition temperature will increase while the second-order transition temperature decreases. On the other hand, when the AFM Fe-Fe interaction becomes weaker, the first-order transition temperature decreases fast from 328 K to zero, if J_{FeFe} changes from -1.1 to -1.06 mRy. Only 4% change of J_{FeFe} already suppresses the first-order magnetic phase transition and makes the system become a normal FM material.

The Ising model with zero-field splitting of FeRh is described in this section. The approximate solution is obtained using the mean field theory. The main results are summarized as follows:

1. The Ising model of FeRh shows both the first-order magnetic phase transition

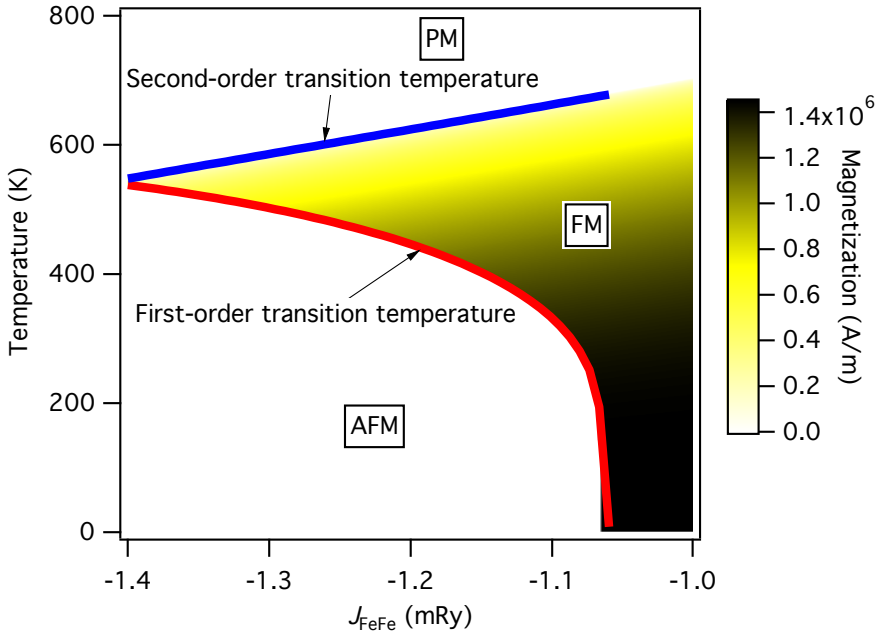

Figure 2.12.: Magnetic phase transition temperature of FeRh.

from AFM to FM and the second-order magnetic phase transition from FM to PM, which can be used to explain the magnetic transitions of FeRh.

2. The numerical results show that the energy level of the singlet lies between the doublet levels in the FM state, while the energy levels of the doublet lies much lower than the doublet levels in the AFM state.

3. The first-order transition temperature decreases dramatically when the AFM Fe-Fe exchange interaction becomes weaker. The first-order magnetic transition from AFM to FM can be absent if the Fe-Fe exchange interaction energy decreases by 4%, and the Ising system of FeRh becomes then a normal ferromagnet.

2.3. Magnetic domain theory

The principle of domain theory goes back to Landau and Lifshitz's famous article [45]. A magnetic domain is a region of magnetic material that has uniform magnetization. The origin of domain structures is the natural consequence of the various contributions to the energy, including exchange energy, anisotropy energy and dipolar energy [46].

2.3.1. Magnetic energy terms

Micromagnetism and domain theory are based on the same variational principle initially established by Landau and Lifshitz [45]. As a consequence, the magnetization direction is chosen so that the total energy reaches a minimum. According to the phenomenological theory, the free energy is the sum of exchange energy, anisotropy energy, Zeeman energy and stray field energy.

Exchange energy

In the continuum representation, the exchange energy density is given by [47, 45]

$$E_{ex} = A \int_V (\Delta m_x)^2 + (\Delta m_y)^2 + (\Delta m_z)^2 \mathrm{d}V, \tag{2.29}$$

where m_x, m_y, m_z are the Cartesian components of the normalized magnetization $\mathbf{m} = \mathbf{M}/|M|$. A is the exchange stiffness constant. This energy originates from the inhomogeneity in the distribution of the direction of magnetic moments.

Anisotropy energy

Magnetic anisotropy is used to describe the dependence of the internal energy on the direction of the spontaneous magnetization [48]. The simplest case is uniaxial magnetic anisotropy, e.g. in hcp Co at room temperature. The uniaxial magnetic anisotropy energy can be expressed as

$$E_a = \frac{1}{2} K_{u1}(1 - \cos(2\theta)) + \frac{1}{8} K_{u2}(3 - -4\cos(2\theta) + \cos(4\theta)). \tag{2.30}$$

The coefficients K_{u1} and K_{u2} are called anisotropy constants. They are typically (e.g. for Co) of the order of $10^5\,\mathrm{Jm}^{-3}$.

For cubic crystals such as Fe and Ni, the anisotropy energy can be expressed as

$$E_a = K_1(\alpha_1^2\alpha_2^2 + \alpha_2^2\alpha_3^2 + \alpha_1^2\alpha_3^2) + K_2\alpha_1^2\alpha_2^2\alpha_3^2, \tag{2.31}$$

where (α_1, α_2, α_3) are the direction cosines of the magnetization vector with respect to the three cube edges. K_1, K_2 are called the cubic anisotropy constants. For iron and nickel they are of the order of 10^3 to $10^4\,\mathrm{Jm}^{-3}$. In contrast to the Fe and Ni, single-crystalline FeRh thin films on MgO(100) grown by sputtering exhibit in the FM state an uniaxial magnetic anisotropy with an in-plane easy axis [14]. Besides, the coercivity of the sputtered FeRh thin films is less than 10 mT. Hence, the anisotropy energy of bulk FeRh is not so large, and FeRh can be considered as a soft magnetic material.

Zeeman energy

The interaction energy of the magnetization vector field with an external field $\mathbf{H}_{ex}$ is

$$E_H = -\mu_0 \int \mathbf{H}_{ex} \cdot \mathbf{M} \mathrm{d}V, \tag{2.32}$$

where μ_0 is the vacuum permeability. If a uniform external field is applied, the Zeeman energy depends only on the average magnetization.

Stray field energy

According to Maxwell's equation

$$\mathrm{div}\mathbf{B} = \mathrm{div}(\mu_0 \mathbf{B} + \mathbf{M}) = 0, \tag{2.33}$$

the stray field $\mathbf{H}_d$ is defined as the field generated by the divergence of the magnetization

$$\mathrm{div}\mathbf{H}_d = -\mathrm{div}(\mathbf{M}/\mu_0). \tag{2.34}$$

Then the stray field energy can be expressed as

$$E_d = -\frac{1}{2} \int \mathbf{H_d} \cdot \mathbf{M} \mathrm{d}V. \tag{2.35}$$

2.3.2. Magnetic domain structure

The essential reason why domains exist is that the domain formation in general reduces the total magnetic energy. As a consequence, the domain structure is not constant attribute of a bulk FM material, but is a functions of the dimensions, the shape, the boundary surfaces as well as strain and temperature [46].

In principle, we can distinguish between two basic geometries of domain structures of magnetic thin film: Films with in-plane anisotropy and films with perpendicular anisotropy [49]. For films with in-plane anisotropy, the magnetization in the domains is parallel to the film surface. The in-plane domain structure is usually determined by the exchange energy and the anisotropy energy [50]. On the other hand, the magnetization in domains is perpendicular to the film surface for films with large perpendicular anisotropy. Out-of-plane domain sizes can be strongly influenced by the stray field energy [51].

When the temperature is above the first-order transition, not only the magnetization of FeRh is changed by temperature (see Fig. 2.11), but also the magnetic anisotropy of FeRh changes in magnitude and even sign, leading to a spin reorientation transition from out-of-plane to in-plane [24, 25]. As consequence, the domain structure of FeRh strongly depends on temperature.

3. Experimental procedures

The experimental procedures and techniques employed in this work and introduced here are based on ultra-high vacuum (UHV). Two kinds of procedures are used: (i) sample preparation and measurement in two different UHV systems with air exposure of the samples during transfer between the systems (in the following called the ex-situ procedure) and (ii) complete in-situ sample preparation and measurement. The second option only became technically available during the course of this thesis.

In this chapter, the experimental UHV setups are briefly introduced. Then the details of the sample preparation methods are presented and finally the principles of both the in-situ magneto-optical Kerr effect (MOKE) and scanning electron microscopy with polarization analysis (SEMPA), the main magnetic characterization techniques, are explained in detail.

3.1. Experimental setups

There are two main setups, which will be introduced here. One is a molecular beam epitaxy (MBE) system dedicated exclusively for thin film preparation, and the other one is the so-called nanospintronics cluster tool (NSCT), which allows both in-situ sample preparation and in-situ magnetic characterization. Both setups are UHV machines with a base pressure below 5×10^{-10} mbar.

The setup of the MBE system is shown in Fig. 3.1. The MBE system comprises three chambers: load-lock, analysis, and preparation chamber, which are shown in Fig. 3.2. The preparation chamber contains two e-beam evaporators with 5 crucibles each for thin film deposition. The analysis chamber is equipped with a low-energy electron diffraction (LEED) optics and an X-ray photoelectron spectrometer (XPS) to characterize the surface properties of the deposited thin films. Besides, the manipulator has an integrated heater so that the sample can be heated up to 1000 K during thin film growth.

Figure 3.3 shows the setup of the NSCT, while Fig. 3.4 shows the schematic drawing of the NSCT, which contains basically five chambers: UHV Gemini, preparation, STM, Transfer, and load-lock chamber. The UHV Gemini chamber houses a scanning electron microscope (SEM), a spin polarization low-energy electron diffraction (SPLEED) detector, and a focused ion beam (FIB) source. The preparation

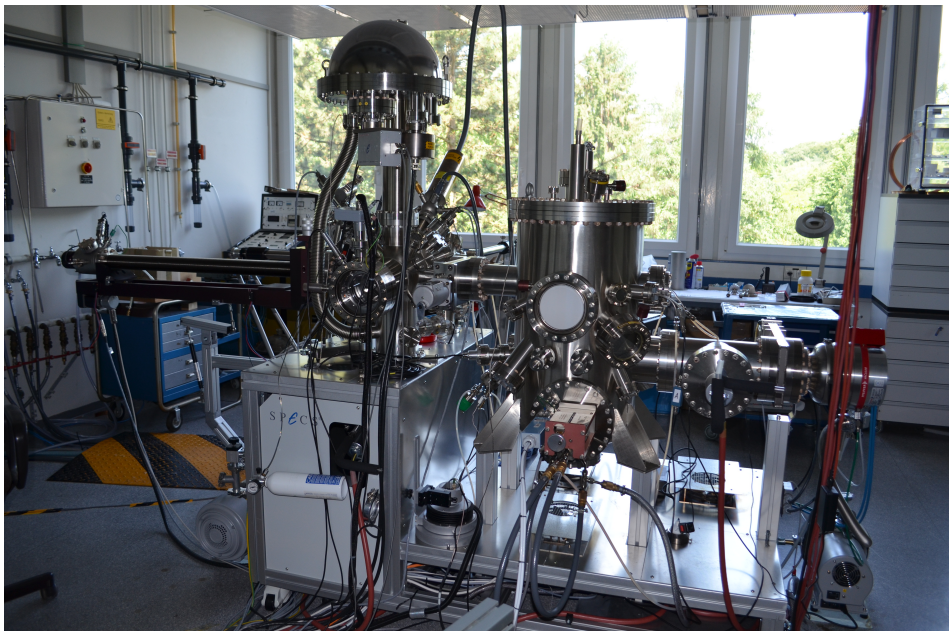

Figure 3.1.: The MBE system used for ex-situ sample preparation.

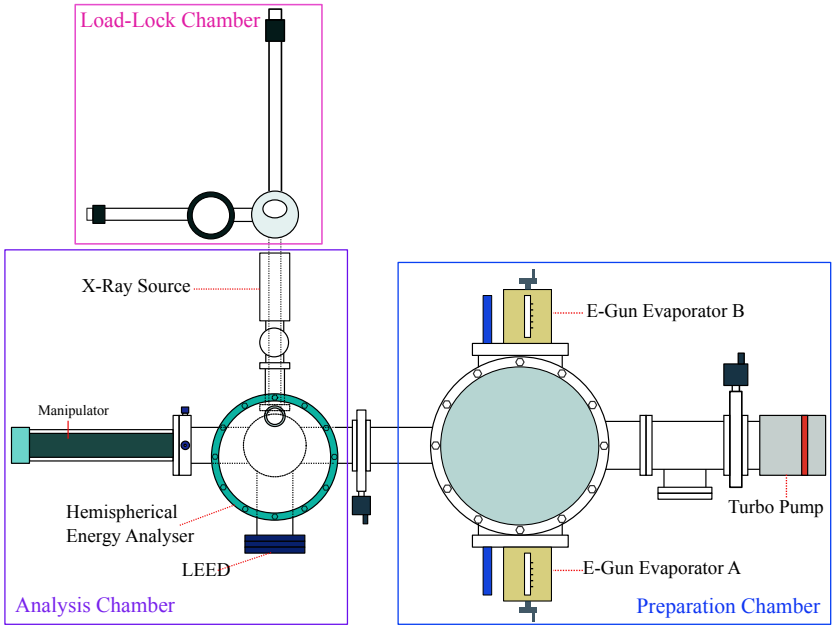

Figure 3.2.: Schematic drawing of the MBE system used for ex-situ sample preparation.

chamber comprises XPS, Auger electron spectroscopy (AES), LEED, an e-beam evaporator with 5 crucibles, an Argon sputtering gun, an e-beam heater, and an in-situ MOKE setup. During the course of this thesis, the in-situ MOKE setup and the new e-beam evaporator have been added in order to achieve complete in-situ sample preparation and measurement in NSCT.

The main purpose of the MBE system is the thin film deposition and structural as well as chemical characterization (ex-situ procedure). The samples, which are prepared in the MBE system, need to be transferred through air to the NSCT for further measurements. Upon exposure to air, the sample will be contaminated or oxidized. Therefore, during the course of this work the NSCT was extended by adding an identical e-beam evaporator as those in the MBE system. With this addition, all sample preparation, characterization, and magnetic measurements can be performed in-situ under best UHV conditions without ever breaking the vacuum. Thus, any contamination or oxidation of the sample should be prevented. Unfortunately, this evaporator became operable only at the very end of the experimental period. Compared to the MBE system, there is only one technical limitation for the sample preparation in the NSCT: The heater in the manipulator of the preparation chamber can only achieve temperatures up to 400 K. As the sample is mounted on this manipulator during the thin films deposition, the effect of higher substrate temperatures during deposition on the thin films growth cannot be explored in the NSCT. But there is a separate e-beam assisted sample heater stage and an oxygen doser in the preparation chamber of the NSCT, which allows post-annealing to temperatures well above 1000 K and in oxygen atmosphere is required. Hence, combining these setups can help understanding the magnetic properties of FeRh thin films prepared with different protocols.

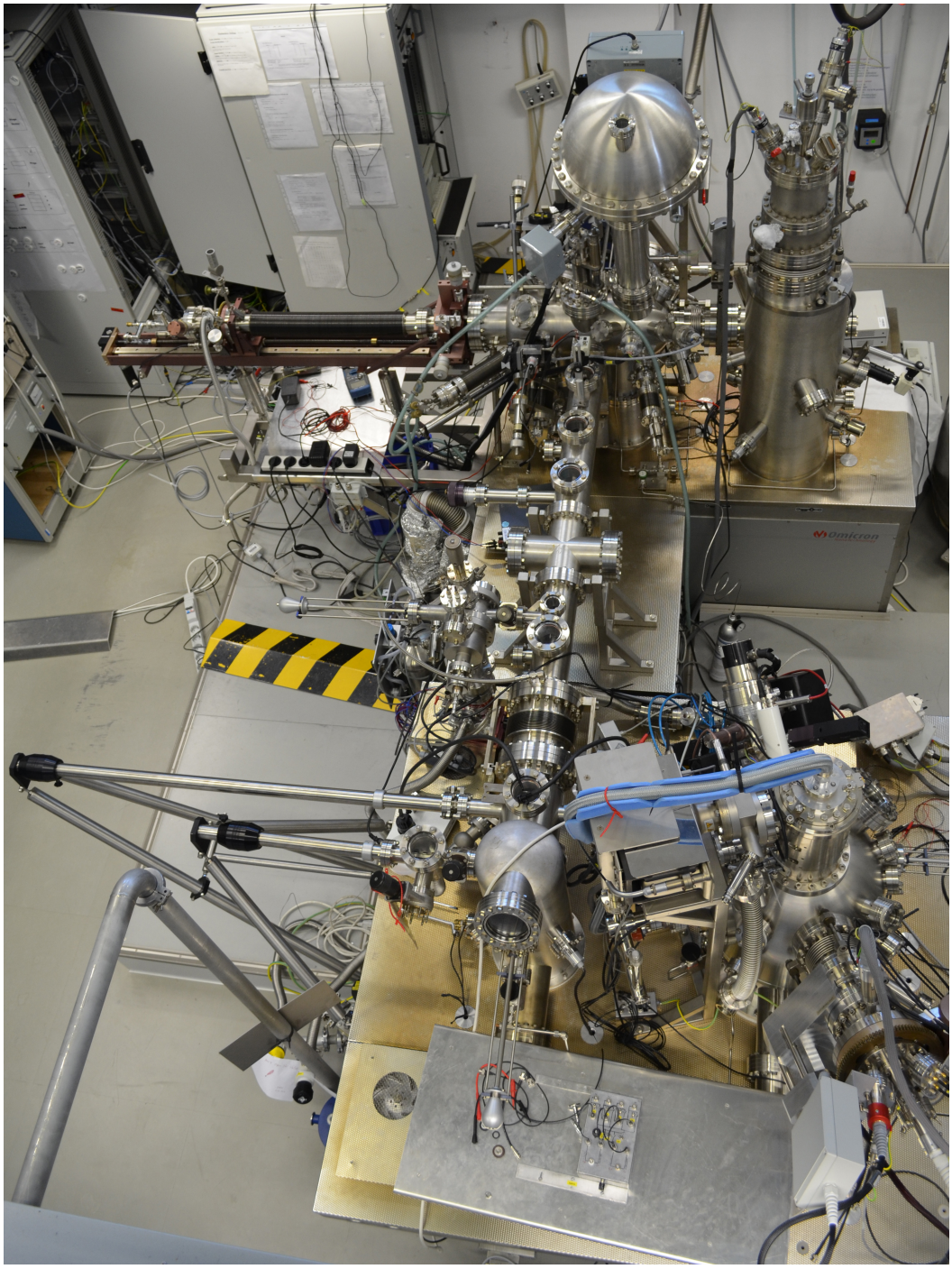

Figure 3.3.: The Nanospintonics Clustertool (NSCT).

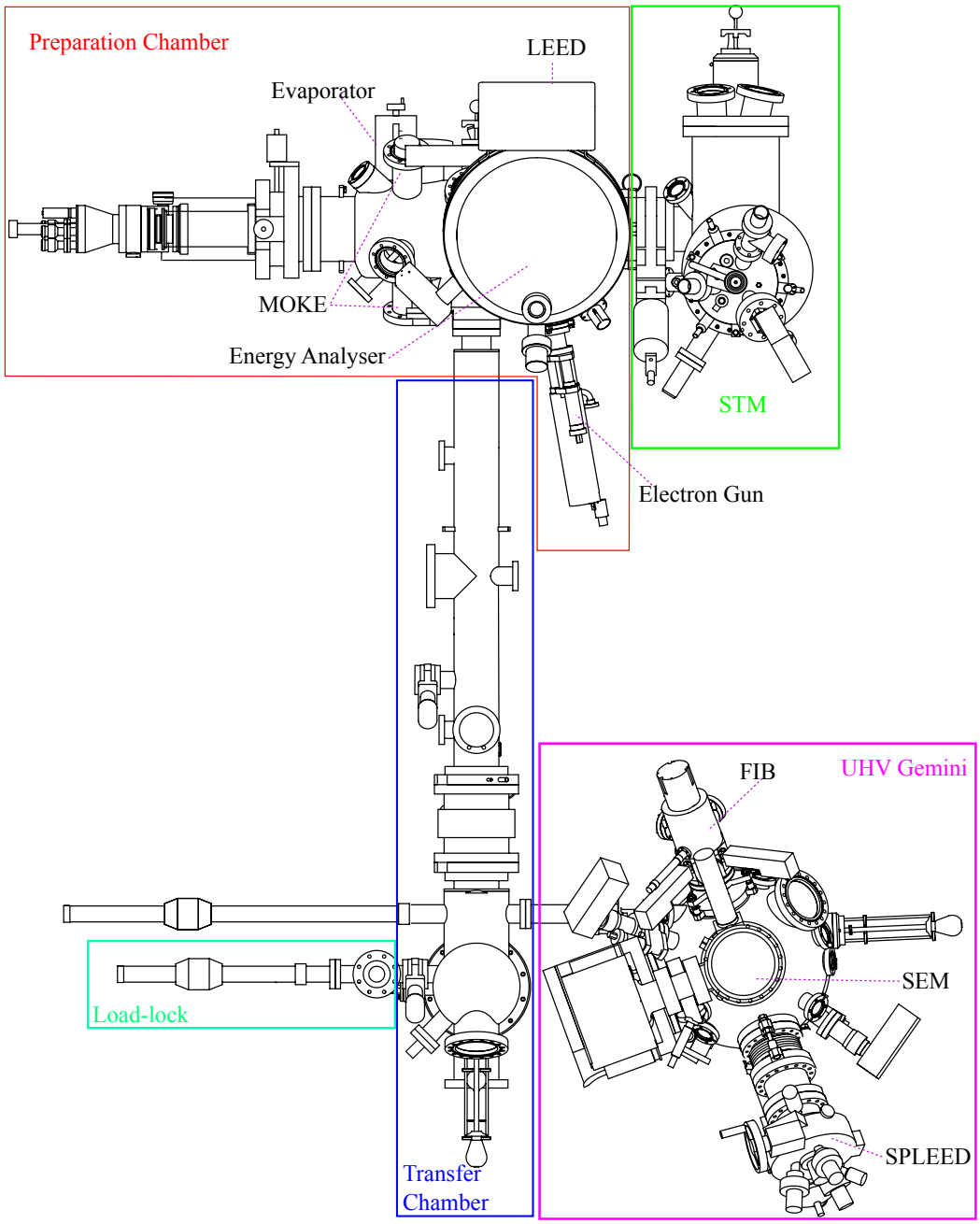

Figure 3.4.: Schematic drawing of the NSCT.

3.2. Sample preparation methods

Typically, there are three ways to prepare single-crystalline FeRh thin films: sputter deposition, co-deposition, and separate layer deposition [52].

Sputtering The most common way to prepare single-crystalline FeRh thin films is sputtering from an FeRh alloy target with certain composition (e.g. $Fe_{51}Rh_{49}$ [43], $Fe_{50}Rh_{50}$[53], $Fe_{47}Rh_{52}$ [54]). The advantage of sputtering is that it is easy to control the composition of the FeRh thin films by using alloy targets of different compositions.

Co-deposition Because the vapor pressures of pure Fe and Rh are significantly different, it is very difficult to deposit single-crystalline FeRh thin films by evaporation from a single FeRh alloy source. But the FeRh thin films can be deposited from two independent e-beam evaporators operated simultaneously. One of them is loaded with Fe and the with pure Rh. However, this requires two independent e-beam evaporators and the possibility to control both evaporation rates [55, 56].

Separate layer deposition A less common way to prepare FeRh thin films is the separate layer deposition route [52]. First a layer of Fe is deposited followed by layer of Rh. The Fe and Rh thicknesses are chosen such that the numbers of Fe and Rh atoms per unit area correspond to the desired composition of the final FeRh film, in our case 50% Fe and 50% Rh. After deposition, the sample needs to be annealed at high temperature for several hours to let Fe and Rh interdiffuse to form the thermodynamically stable CsCl-ordered phase. A potential disadvantage of this method is that the intermixing may not be homogeneous throughout the film, which is more likely for thicker films involving longer diffusion distances. The separate layer deposition method can be achieved with a single e-beam evaporator with at least two crucibles. Thus, it is the only preparation method that can be realized in the NSCT.

In the following the separate layer deposition procedure is adopted to prepare single-crystalline FeRh thin films on MgO substrates. Both ex-situ and in-situ sample preparation procedures are performed by similar techniques. After deposition, the surface order is investigated by LEED, and the composition (and contamination) is analyzed by AES or XPS.

3.2.1. Thermal evaporation

The main components for e-beam evaporation are the e-beam evaporator itself, a mircobalance (based on a quartz crystal sensor) to determine the evaporation rate, and a manipulator to handle the sample and control its temperature. E-beam evaporation is widely used for thin film preparation, because it is compatible with UHV and allows to evaporate very pure materials. In both the MBE system and

the NSCT, there are e-beam evaporators with five crucibles in linear arrangement, such that each crucible can be shifted to the position of the electron beam. Thus only one crucible can be operate at the same time. A cross section of the e-beam evaporator is shown in Fig. 3.5. A high voltage of -5 keV is applied to the filament with respect to ground. The filament is heated by a current source. When the electrons thermally emit from the filament, they are accelerated in the field. The electron beam is bent and focused to the crucible by a magnetic field generated by a permanent magnet. When the evaporation source material reaches a certain material dependent temperature, the material will be evaporated. A microbalance located next to the sample and exposed to the flux of the evaporated material above the crucible is used to monitor the evaporation rate. A shutter introduced between the sample and the crucible, but above the microbalance determines the deposition time. Thus the evaporation rate can be controlled during the whole evaporation process. The directional distribution of the material flux follows the cosine law of emission expressed by [57]

$$j_\Omega(\theta, \phi) = \frac{z \cos\theta}{\pi}, \tag{3.1}$$

where θ is the angle with respect to the normal emission direction and z the crucible-substrate distance. Equation (3.1) indicates that the distribution of materials on a flat sample is not homogeneous even if the emission of atoms is stable. But when the distance z between the sample and the evaporation source is large compared to

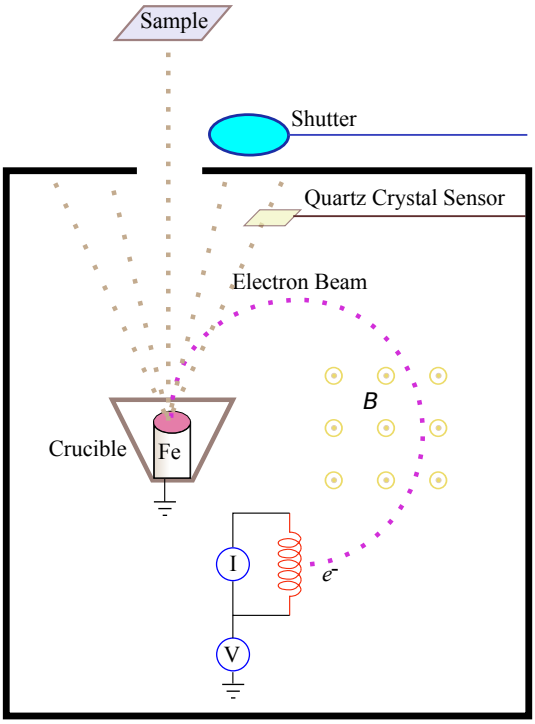

Figure 3.5.: Schematic cross section drawing of an e-beam evaporator.

the substrate size, the error is negligible. In our case, $z \approx 40\,\text{cm}$ and the samples are $1 \times 1\,\text{cm}^2$ in size.

The temperature of the sample on the manipulator is controlled either by e-beam heating from the back side or by cooling with liquid nitrogen. The thickness of the materials evaporated on the sample can be monitored by the microbalance. However, as the microbalance measures the deposited mass rather than the thickness of the sample and is positioned at a different position as the sample, the thickness monitor needs to be calibrated. A thin Au film was evaporated onto a MgO substrate and its thickness was determined from X-ray reflectivity measurements using an open source software *GenX* [58].

3.2.2. Low-energy electron diffraction

Low-energy electron diffraction (LEED) is one of the most common electron-based techniques for surface structure determination. LEED is often used to check the crystal structure and surface reconstructions [59]. The basic requirements for LEED measurements are a electron gun, a manipulator and a screen. Figure 3.6 shows a LEED with a hemispherical semi-transparent screen. Electrons are emitted from the gun and perpendicularly impinge on the sample with an energy in the range from 30 to 500 eV. The probing depth of the low-energy electrons is only a few Ångstrom, hence, LEED is a very surface sensitivity technique.

We consider electron scattering from a two-dimensional lattice, which is defined by the two lattice vectors $\mathbf{a_1}$ and $\mathbf{a_2}$. If the incident electron beam's energy is E, then the wavelength of electron in the unit of Å is given by

$$\lambda = \sqrt{\frac{150.4}{E(\text{eV})}}(\text{Å}), \tag{3.2}$$

i.e. λ is of the order of one Å.

For LEED, only elastic scattering is considered. Thus, the incident and scattered beams have the same energy and wavelength. If the incident and scattered beams are described by unit vectors $\mathbf{s}$ and $\mathbf{s}'$, respectively, then the scattering vector is given by

$$\Delta\mathbf{s} = \mathbf{s} - \mathbf{s}'. \tag{3.3}$$

According to the Laue conditions, diffraction from a two-dimensional lattice must satisfy the two conditions [60]

$$\mathbf{a_1} \cdot \Delta\mathbf{s} = h\lambda, \qquad \mathbf{a_2} \cdot \Delta\mathbf{s} = k\lambda, \tag{3.4}$$

where h and k are integer numbers. If $\mathbf{G}_{hk} = h\mathbf{b_1} + k\mathbf{b_2}$ represents the reciprocal lattice spanned by the basis $\mathbf{b_1}$ and $\mathbf{b_2}$, then the Laue conditions can be also written

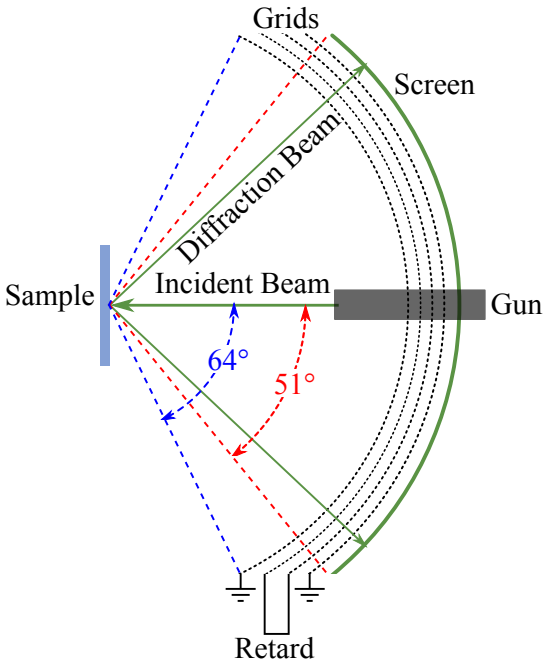

Figure 3.6.: Hemispherical LEED optics.

as

$$\Delta \mathbf{s} = \frac{\lambda}{2\pi} \mathbf{G}_{hk}. \tag{3.5}$$

This means that the reciprocal lattice of the crystal surface can be deduced from the observed LEED pattern.

3.2.3. X-ray photoelectron spectroscopy

X-Ray Photoelectron Spectroscopy (XPS) is used to analyze the chemical composition in the MBE system. The main components for XPS are a X-ray source and a hemispherical energy analyzer. The XPS installed in the MBE system is schematically shown in Fig. 3.7. The sample surface is perpendicular to the axis of the entrance lense of the energy analyzer and the incident angle of the photons is 54.7 °, the so-called the "magic angle".

In the x-ray source an anode material is bombarded with high-energy electrons to generate characteristic X-ray radiation superimposed to the *Bremsstrahlung* spectrum. The anode materials employed in the XR-50 x-ray source are Al and Mg with radiation lines at energy of 1486.6 and 1253.6 eV, respectively. When x-ray phonons are absorbed in the sample, electrons can be excited, travel through the sample to the surface, escape through the surface, and are finally detected in the

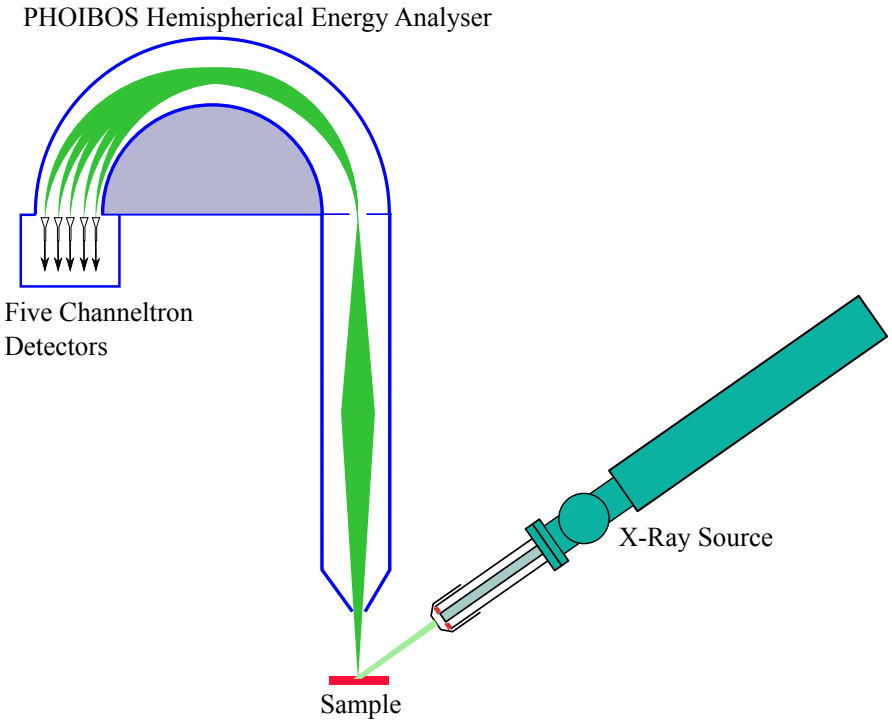

Figure 3.7.: Schematic cross section of the XPS instrument in the MBE system. It comprises an XR-50 x-ray source and a PHOIBOS hemispherical energy analyser with five channeltron detectors.

hemispherical energy analyzer. If the binding energy is E_b, the phonon energy is $h\nu$, and using the work function Φ_A of the PHOIBOS hemispherical energy analyzer is $\Phi_A = 4.324\,\mathrm{eV}$, then the kinetic energy E_k of the electron measured by the analyzer is [61]

$$E_k = h\nu - E_b - \Phi_A. \tag{3.6}$$

Normally for XPS, the energy analyzer is operated in the constant-analyzer-energy (CAE) mode, where the electrons are retarded in the entrance lense of the analyzer to pass the hemisphere with a constant energy resulting in a constant energy resolution $\Delta E = \text{const.}$ throughout the whole spectra. The intensity is recorded as a function of the kinetic energy of the emitted electron, which is varied by sweeping the retarding potential. After an XPS spectrum is obtained, the detected elements can be identified comparing the peak positions with a data base. For a quantitative analysis, the background of the spectrum needs to be subtracted and then the chemical composition can be estimated using tabulated elemental relative sensitivity factors. All these operations can be performed by the software CasaXPS [62].

3.2.4. Auger electron spectroscopy

In a typical Auger electron spectroscopy (AES) measurement, the sample is irradiated with a high-energy electron beam (about 3 keV) from an electron gun. As a result, the atoms in the sample are ionized and outer shell electrons fill up the ionized states. As an alternative to radiative decay (florescence), the energy released by this process is transmitted to another outer shell electron, the so-called Auger electron, that is emitted from the atom.

The AES in the NSCT consists of a high-energy electron gun and a hemispherical analyzer as shown in Fig. 3.8. The applied high voltage to the electron gun is 3 keV. The incident electron beam angle is 45° with respect to the sample plane, while the entrance axis of the energy analyzer is perpendicular to the sample plane. In addition, the sample is tilted by 15° with respect to the horizontal direction. Normally for AES, the energy analyzer is operated in constant-retard-ratio (CRR) mode, where the ratio between retarding potential and pass energy is kept constant. As a consequence, the energy resolution of the analyzer is not constant throughout the spectra, but $\Delta E/E = \text{const}$.

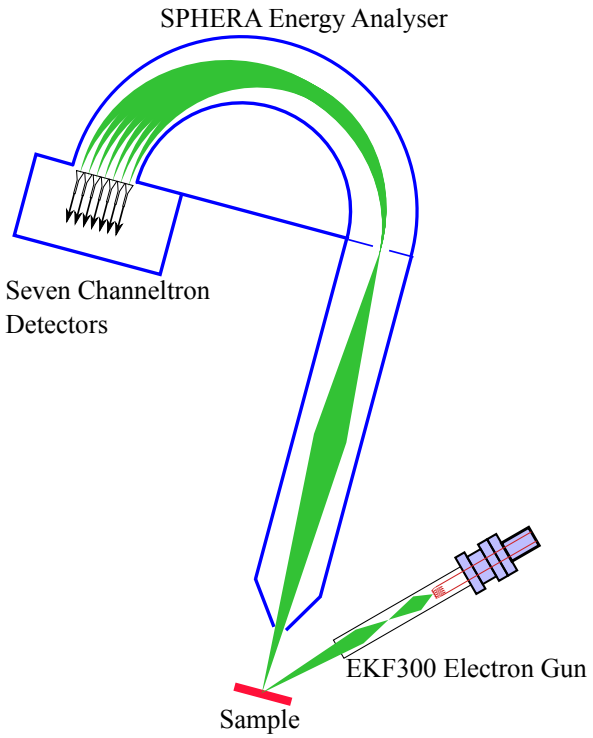

Figure 3.8.: Schematic cross section of the AES instrument in the NSCT. It comprises an EKF300 electron gun and a SPHERA energy analyzer with seven channeltron detectors.

Table 3.1.: Auger sensitivity factors S_i for i = Fe, Rh, C, and O taken from the Auger handbook [64].

Element	Energy (eV)	S_x at 3 keV
C	275	0.6143
O	510	1.2571
Fe	600	0.5359
	654	0.7878
	705	0.9494
Rh	259	0.8283
	305	3.1578

The intensity is recorded as a function of the kinetic energy of the emitted electron. Once the spectrum is recorded, is is numerically differentiated with respect to the energy using a five-point Savitzky-Golay filter in order to get rid of the background [63] and for a better comparison with tabulated spectra [64], which are presented in the differentiated form. In addition to identifying the elements that contribute to the spectra based on the peak positions, on can also obtain the chemical composition using the Auger sensitivity factors. For example, if the measured Auger peak-to-peak height in the differentiated spectrum is I_i for element i in a homogenous alloy with N elements and the relative Auger sensitivity factors are S_i, then the surface atomic concentration of element i, X_i, can be estimated as [65, 66]

$$X_i = \frac{I_i/S_i}{\sum_{n=1}^{N} I_n/S_n}. \tag{3.7}$$

The reference Auger sensitivity factors of Fe and Rh are taken from the Auger Handbook [64] and are listed in Table 3.1 together with those of the most important contaminations in the spectra.

3.3. In-situ magneto-optical Kerr effect

The magneto-optical Kerr effect (MOKE) of ferromagnetic thin films has been intensively studied over last decades [67, 68]. The probing depth of MOKE is material dependent, but typically about 20 nm [69]. An in-situ MOKE setup has been added to the NSCT in order to study the metamagnetic transition of FeRh thin films. The principle of the in-situ MOKE setup will be introduced here.

When linearly p-polarized light is reflected from a sample surface, if the sample is nonmagnetic, the reflected light is purely p-polarized. But if the sample is ferromagnetic, the reflected light can contain an s-component in addition to the p-component [70]. The magneto-Optical Kerr effect is phenomenologically expressed

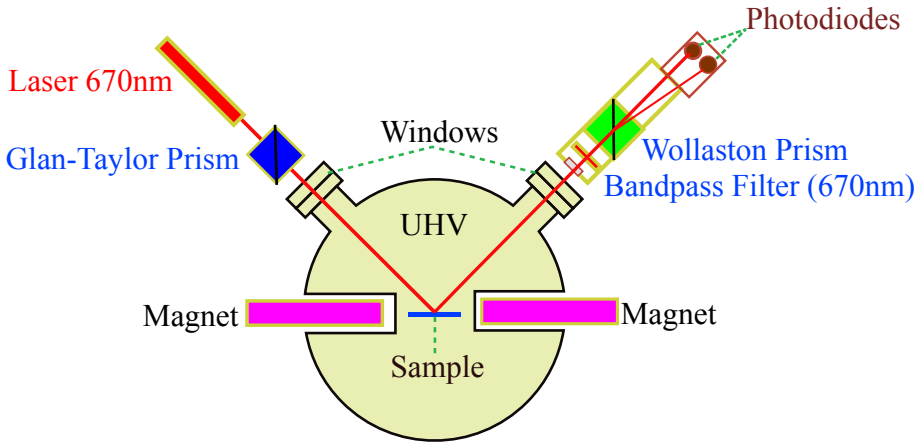

Figure 3.9.: Schematic drawing of the in-situ MOKE setup.

as

$$E_s/E_p = \phi' + i\phi'', \tag{3.8}$$

where $E_{s,p}$ is the s- and p-component, respectively, of the laser beam. ϕ is the Kerr rotation and ϕ'' the ellipticity. The MOKE setup in the NSCT is installed in the preparation chamber and allows measuring the Kerr rotation in-situ immediately after preparing a sample in the NSCT. The longitudinal MOKE configuration, which is sensitive to the in-plane magnetization component in the plane of reflection, is shown in Fig. 3.9. During operation, the sample is mounted on manipulator that can cooled to 143 K by liquid nitrogen.

The optical components of MOKE setup are a laser, a polarizer, and an analyzer. The wavelength of laser is 670 nm, and the laser intensity is modulated at a frequency of 333 Hz in order to employ a lock-in detection technique to reduce the noise and avoid disturbances of the light from the environment. The employed polarizer is Glan-Taylor prism, which totally reflects s-polarized light but transmits p-polarized light [71].

For the polarization analysis of the reflected we use a Wollaston prism, which splits the reflected polarized light into two orthogonal linearly polarized outgoing beams. One beam does not change the propagation direction, but the other beam has a divergence angle of 10°. The outgoing beams' intensities depend on the polarization detection of the incident light and the orientation of the polarization axis of the Wollaston prism. For a given incident polarization state of the incident light, one can adjust the intensities of the two outgoing beams to be equal by rotating the prism. Two photodiodes are used to detect the intensity of the two beams enabling a sensitive detection of small changes of the incident polarization state.

If the azimuth angle of the Glan-Taylor polarizer prism is α, assume that the probe light is p-polarized when $\alpha = 0$ and s-polarized when $\alpha = 90°$. If the azimuth

angle of the Wollaston analyzer prism is $\beta = 0°$, the signal of photodiode 1, $|I_1|^2$, is maximum, whereas for $\beta = 90°$ the signal of photodiode 2, $|I_2|^2$, is maximum. When the input light is p-polarized, the splitted beam amplitudes can be expressed by the reflected light's s and p components $E_{s,p}$

$$\mathbf{I} = \begin{bmatrix} I_1 \\ I_2 \end{bmatrix} = \begin{bmatrix} \cos\beta & \sin\beta \\ -\sin\beta & \cos\beta \end{bmatrix} \begin{bmatrix} E_p \\ E_s \end{bmatrix}. \tag{3.9}$$

Thus,

$$\begin{aligned} |I_1|^2 &= \cos^2\beta E_p E_p^* + \sin^2\beta E_s E_s^* + \sin\beta\cos\beta(E_p E_s^* + E_s E_p^*) \\ |I_2|^2 &= \sin^2\beta E_p E_p^* + \cos^2\beta E_s E_s^* - \sin\beta\cos\beta(E_p E_s^* + E_s E_p^*). \end{aligned} \tag{3.10}$$

Because we use differential detection, there are two output signal, one is the common output $I_{\text{com}} = |I_1|^2 + |I_2|^2$, the other is differential output $I_{\text{diff}} = |I_1|^2 - |I_2|^2$,

$$\begin{aligned} I_{\text{com}} &= E_p E_p^* + E_s E_s^* \\ I_{\text{diff}} &= (\cos^2\beta - \sin^2\beta)(E_p E_p^* - E_s E_s^*) + 2\sin\beta\cos\beta(E_p E_s^* + E_s E_p^*). \end{aligned} \tag{3.11}$$

Substituting Eq. (3.8) into Eq. (3.11) yields

$$\begin{aligned} I_{\text{com}} &= E_p^2(1 + \phi'^2 + \phi''^2) \\ I_{\text{diff}} &= (\cos^2\beta - \sin^2\beta)E_p^2(1 - \phi'^2 - \phi''^2) + 4\sin\beta\cos\beta E_p^2\phi'. \end{aligned} \tag{3.12}$$

For $\beta = 45°$, the differential output can be simplified as

$$I_{\text{diff}} = 2E_p^2\phi', \tag{3.13}$$

and as $1 \gg \phi'^2 + \phi''^2$

$$I_{\text{com}} \simeq E_p^2. \tag{3.14}$$

As a result, the Kerr rotation can be easily obtained by

$$\phi' = \frac{1}{2}\frac{I_{\text{diff}}}{I_{\text{com}}}. \tag{3.15}$$

However, during adjustment it is very difficult to have exactly $\beta = 45°$, if $\beta = 45° + \delta$, where δ is the misalignment angle, then

$$\begin{aligned} I_{\text{com}} &= E_p^2(1 + \phi'^2 + \phi''^2) \\ I_{\text{diff}} &= \sin(2\delta)E_p^2(1 - \phi'^2 - \phi''^2) + 2\cos(2\delta)E_p^2\phi'. \end{aligned} \tag{3.16}$$

Since both the Kerr rotation ϕ' and the Kerr ellipticity ϕ'' are very small compared to unity and we also assume that the misalignment angle δ is also very small, the differential output can be approximated as

$$I_{\text{diff}} = 2E_p^2(\phi' + \delta). \tag{3.17}$$

From Eq. (3.17) it is obvious that for small δ, the differential signal is offset proportional to δ. Therefore, a small misalignment has no influence on the shape of MOKE hysteresis loops, for which ϕ' is measured as a function of the applied field. Besides, the average of many loops can be taken to supress the spurious influence of the possible drift of the laser intensity and to reduce the noise [69].

3.4. Scanning electron microscopy with polarization analysis

Scanning electron microscopy with polarization analysis (SEMPA) is a technique for high-resolution magnetic domain observation. The functional parts of a SEMPA are shown in Fig. 3.10. The setup mainly contains two parts, one is a high-resolution SEM and the other a spin polarization low-energy electron diffraction (SPLEED) detector. The angle between the SEM column and the SPLEED column is 60°. During operation, the sample plane is perpendicular to the SPLEED detector for the detection of the two in-plane magnetization components of the sample. The angle of incidence of the electron beam is then 60°. For the detection of out-of-plane components, the angle between surface normal and SPLEED axis should be as large as possible (but still compatible with the working distance of the SEM). The SPLEED detector has been updated from channeltrons to multi-channel plates (MCPs) during the course of this thesis. Compared to the channeltrons, the MCPs have a longer lifetime [72].

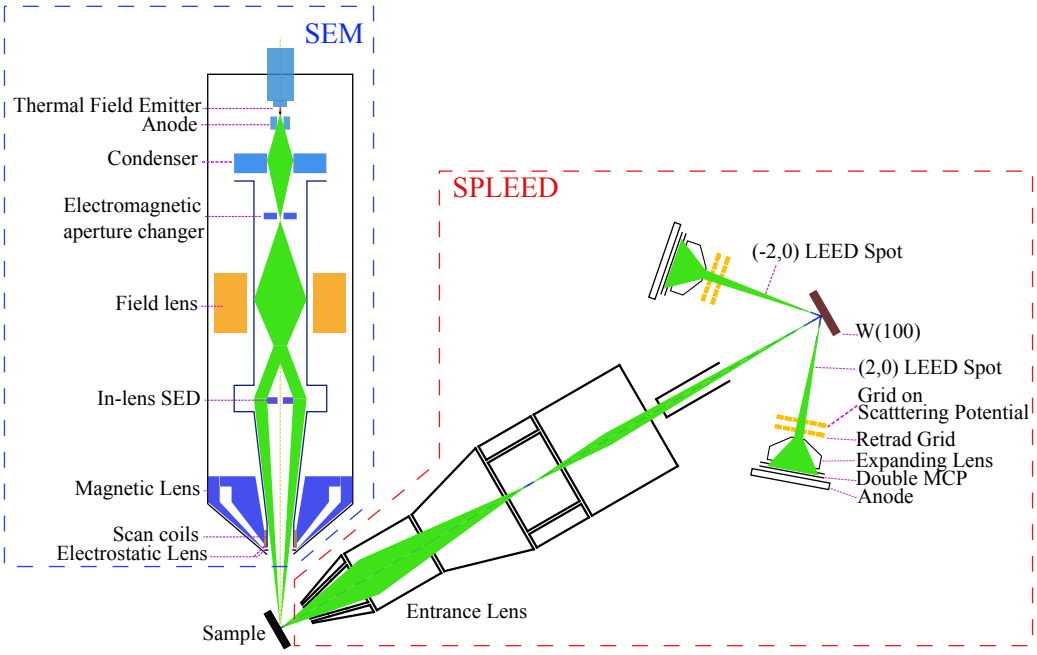

Figure 3.10.: Functional parts of the SEMPA with MCPs-detectors.

3.4.1. Scanning electron microscopy

There are many imaging modes of SEM, but the modes named “secondary electrons (SE)” and “backscattered electrons (BSE)” are the most important ones. By

convention, electrons with exit energies larger than 50 eV are called backscattered electrons, and electrons with exit energies less than 50 eV are called secondary electrons.

There is a empirical formula that describes the backscattering coefficient η [73]

$$\eta(Z, \phi) = (1 + \cos(\phi))^{-9/\sqrt{Z}}, \tag{3.18}$$

where Z is the atomic number of the sample material and ϕ the tilt angle ($\phi = 0$ corresponds to normal incidence). Owing to the the large information volume and exit area, the BSE mode can image the surface topography only at lower magnification.

On the other hand, in the SE mode electrons can leave the specimen only from a small exit depth t_{SE}, which is of the order of 0.5 to 1.5 nm for metals. In the range of 1 to 100 eV, the SE emission yield can be simply described by [73]

$$\delta \propto E^{-0.8} \sec(\phi) t_{SE}, \tag{3.19}$$

where E is the primary electron beam energy. The SE yield decreases as E increases, but increases as ϕ becomes larger.

SEMPA is based on the SE mode of SEM. Hence, SEMPA is very surface sensitive and the probing depth is only a few atomic layers. In order to increase the SE yield and, thus, to achieve a better signal-to-noise ratio, the energy of the electron beam should not be too large. At the same time, the energy should not be too small because lower beam energies decrease the spatial resolution of SEM. For the normal operation of SEMPA, the primary beam energy is between 5 to 10 kV. When the electron beam scans an insulating sample, e.g. MgO or a thin metal film on MgO, it accumulates electrical charge (charging), such that a negative potential builds up, which lowers the spatial resolution. In this case, a higher beam energy can yield a better resolution.

3.4.2. Spin-polarized low-energy electron diffraction

It has been observed that SE from a ferromagnet excited by unpolarized primary electrons are spin-polarized [74]. The characteristic feature of the band structure of ferromagnets is an imbalance between spin-up and spin-down electrons at the Fermi level. When a ferromagnet is irradiated with an electron beam with energies in the range of a few keV, the spin polarization of the SE depends on the magnetization of the emitting sample area. Both the SE yield and the SE polarization depend on the primary energy E. The SE polarization is enhanced for low-energy (a few eV only) SE. This enhancement is commonly believed to originate from the cascade process of SE creation [75].

After the polarized SE escape from the sample surface, the SE polarization can be detected, in our case by the SPLEED detector. The first successful spin-polarized

double-scattering LEED experiment was done by Kirschner [76]. If the electron-solid interaction contains a spin-dependent contribution, the LEED beams exhibit spin polarization effects, which can manifest themselves in two forms: First as an asymmetry in the scattered intensities for polarized primary beams of opposite spin alignment and second as spin polarization of the diffracted beams for an unpolarized primary beam [77].

The operating principle of SPLEED detector is based on the first effect, namely the asymmetric scattering of spin-polarized electrons from a surface, which originates from the spin-orbit coupling contribution to the electron-solid interaction potential, see Fig. 3.10. The SPLEED detector employs scattering of the spin-polarized electrons from the (001) surface of a W single crystal to take advantage of the strong spin-orbit coupling in this high-Z material.

The polarized SE emitted from the sample are collected by the entrance lens, accelerated to an energy of 104.5 eV, and focused onto the well-ordered W(100) crystal, where they are diffracted by the surface lattice as in a LEED experiment. Four structurally equivalent diffraction spots are detected by four MCPs. An expanding lens just in front of the MCPs spreads the beam to cover the whole MCPs area. This reduces the areal current density and, thus, increases the lifetime of the MCPs [72, 78].

As in a LEED setup, the primary beam impinges perpendicularly onto the W(001) surface. Among the diffracted beams, the structurally equivalent $(2,0)$, $(\bar{2},0)$, $(0,2)$, and $(0,\bar{2})$ beams are detected by four MCPs. For unpolarized normally incident electrons, the four (2,0) beams are equivalent and of equal intensity. If the incident beam has a polarization vector normal to the electron momentum, the intensities of the four beams are no more the same. The polarization can be calculated from the count rates of the four MCPs $N_{\rightarrow,\leftarrow,\uparrow,\downarrow}$

$$P_x = \frac{N_{\rightarrow} - N_{\leftarrow}}{N_{\rightarrow} + N_{\leftarrow}} \tag{3.20}$$

$$P_y = \frac{N_{\uparrow} - N_{\downarrow}}{N_{\uparrow} + N_{\downarrow}}. \tag{3.21}$$

Since the polarization is calculated as the normalized intensity difference, SEMPA can in principle suppress topographic contributions. However, due to the finite size of the interaction zone of the electron beam with matter, the suppression of the topography is not perfect. Figure 3.11 shows the so-called topographic effect in SEMPA for a magnetic thin film on a nonmagnetic substrate. When the surface roughness of the magnetic thin film (typical several nanometers) is much smaller than the electron range (e.g. 1 μm for a 10 keV electron beam in Al), the surface roughness can not affect the secondary yield and the spin polarization (see Fig. 3.11 (a)). But when there is a particle or a gap that is larger than the electron range, the secondary electron yield can be changed strongly. See Fig. 3.11 (b), if the

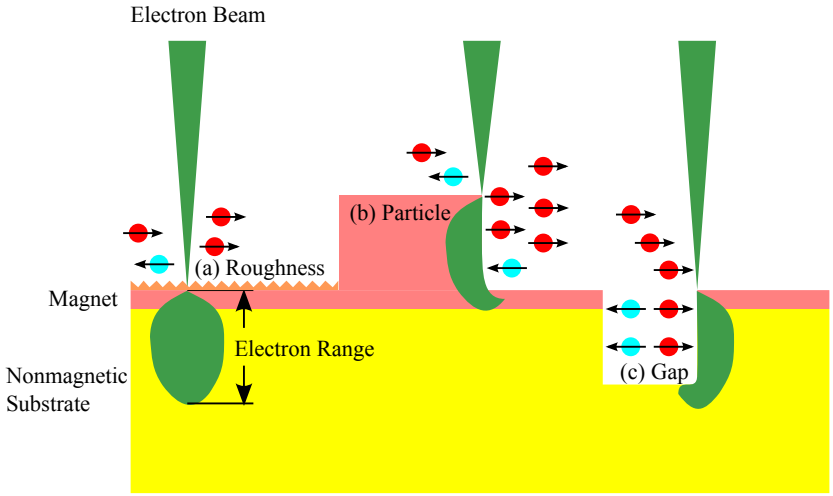

Figure 3.11.: Sketch of topographic effect of a magnetic thin film in SEMPA for (a) a rough surface, (b) a magnetic particle, and (c) a gap.

electron beam incidents at the edge of the particle, more secondary electrons can escape from the edge of the particle, or the backscattering electrons even escape from the edge and are scattered in a cascade so that more secondary electrons are generated. Hence, the yield of secondary electrons can be strongly enhanced at the edge of a particle. On the other hand, if there is a deep gap, the SE may be absorbed by the walls, so that the SE yield will be strongly reduced, see Fig. 3.11 (c). When the SE yield changes too much, the normalization of the intensity difference cannot suppress anymore the topological contrast effectively. Device asymmetry (e.g. amplification asymmetry of the MCPs) can become a delicate problem in SEMPA measurements and may result in a spin polarization even for nonmagnetic substrates [75]. Hence, in real SEMPA measurements, one must be careful not to misinterpret topographic effects as magnetic polarization.

If the incident beam current is I_0, the measured reflectivity is $R = I_{(2,0)}/I_0$. With the polarization of the detector beams is P, the figure of merit for the electron polarization measurement is defined as

$$F = P^2 R. \tag{3.22}$$

The larger this number, the better the efficiency of the detector. The maximum figure of merit of a W(001)-based SPLEED detector operated at a diffraction energy of 104.5 eV is $F = 1.6 \times 10^{-4}$ [79]. Compared with Mott detectors ($F = 6 \times 10^{-4}$ [80]), though the figure of merit of SPLEED detectors is lower. However, a SPLEED detector is much more compact than a Mott detector, because a Mott detector requires much higher electrostatic acceleration voltages (e.g. 40 kV) than the SPLEED detector (e.g. 3 kV) so that the electron lenses and the power supplies

for the Mott detector are much larger.

3.4.3. Calibration of the four MCPs

During SEMPA measurement four images are obtained by recording the intensity of the four diffraction beams from the W(100) crystal. From these four images, one can calculate using Eqs. (3.20) and (3.21) the magnetic domain image of the sample. However, this requires a calibration of the four MCPs signals.

Before the SEMPA measurement one needs to adjust the diffraction and lense voltages of the SPLEED detector to eliminate offsets of the four MCPs using an unpolarized electron beam. One way to obtain an unpolarized electron beam is to scan a nonmagnetic material. However, when the sample is an extended ferromagnetic film, it is not easy to obtain an unpolarized electron beam to adjust the MCPs. In addition, even when the intensity of four diffraction beams impinging on the MCPs have the same intensity, there can still be an asymmetry at the MCPs outputs, e.g. due to different amplification factors and beam trajectories for the four MCPs.

If one cannot adjust the MCPs output signals properly, the actual asymmetry can be estimated by a post-processing procedure using the known domain structure of a well-defined sample geometry. The closed-flux domain structure of a square element cut from a single-crystalline Fe thin film on GaAs(100) shows a symmetric magnetization pattern, the so-called Landau domain structure, if the edges of the square are aligned with the easy axes of the cubic magnetocrystalline anisotropy [81]. The Landau domain pattern results from the interaction of shape and magnetocrystalline anisotropy.

Figure 3.12 shows the domain structure of a 25 nm thick Fe film, into which a quadratic frame is milled by an focused ion beam (FIB) of 30 keV Ga^+ ions. Figure 3.12(a) is the topography image obtained by adding all four MCPs intensities. This signal is very sensitive to topographic contrast and the surface contamination since the SPLEED detector can be viewed as a secondary electron detector. The blue area is the ditch created by the FIB milling. The ditch is about 750 nm wide and its edges run along the easy axes of the Fe film. If the ion beam dose is high enough, all Fe atoms are removed in the ditch, and even atoms of the substrate may have been removed. As a result, the central square with a size of $1.5 \times 1.5\ \mu m^2$ is magnetically decoupled from the environment. The light grey area around the ditch is mainly due to the re-deposition of sputtered material, which has a different work function than the Fe film.

Figures 3.12(b) and (c) show flux-closed domain structures inside the square and in the upper left corner of the images (see the red circles in Figures. 3.12(b) and (c)). The flux-closed magnetic domain structures have four 90° domain walls separating four domains and a vortex in the center.

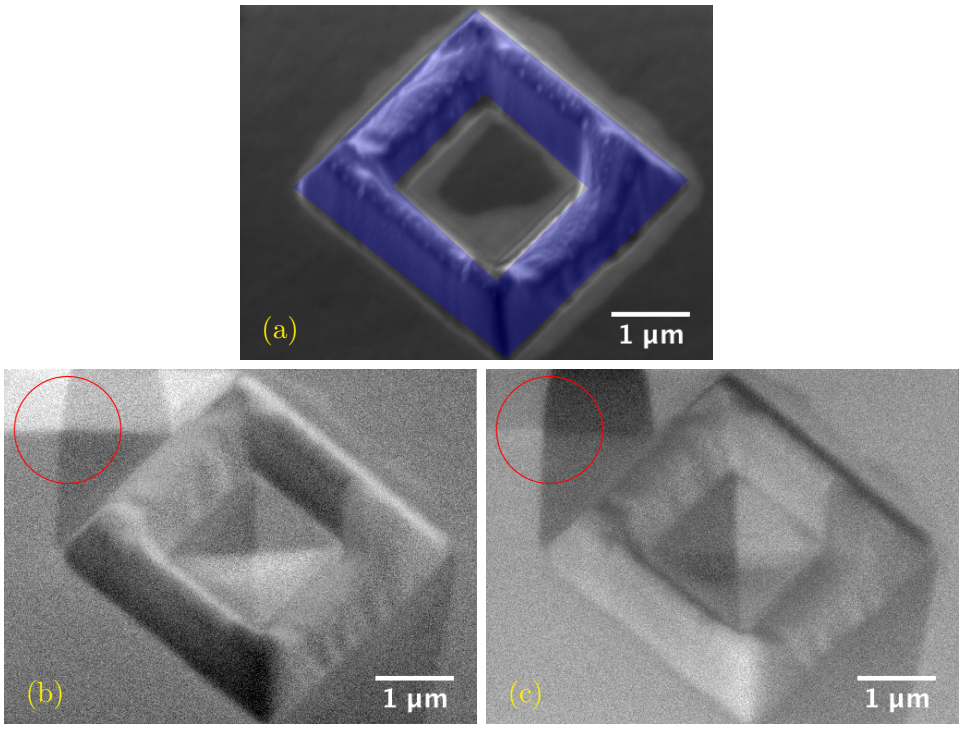

Figure 3.12.: SEMPA images of a Fe square element made by FIB milling of a Fe thin film on GaAs(100). (a) The sum of all four MCPs channels represents the surface topography. (b) and (c) are the P_x and P_y images, respectively, according to Eqs. (3.20) and (3.21). They correspond to the in-plane magnetization components M_x and M_y.

In order to calibrate the offsets of the MCPs we consider a certain position (x, y) of the Fe thin film. The in-plane magnetization at this position (M_x, M_y) is proportional to the polarization vector of the SE emitted from this site, $\mathbf{P} = (P_x, P_y) \propto (M_x, M_y)$ [82]. If the domain walls and the vortex core, which both have sizes of the order of 10 nm, are neglected, the local polarization vectors of the flux-closed domain structure point in four different orientations, but have everywhere the same magnitude. Therefore, the density plot of polarization distribution in such an ideal case is expected to have four symmetric spots.

We extract the values of the polarization of both flux-closed domain structures in Figures. 3.12(b) and (c) after applying a Gaussian filter to reduce the noise in the two-dimensional data. The resulting density plot of the polarization distribution is shown in Fig. 3.13. There are four clearly resolved spots, which are slightly blurred due to noise. The intensity on the lines connecting the four spots is due to the domain walls.

Note that the center of the four spots is not at the zero position, $\mathbf{P} = 0$. This is

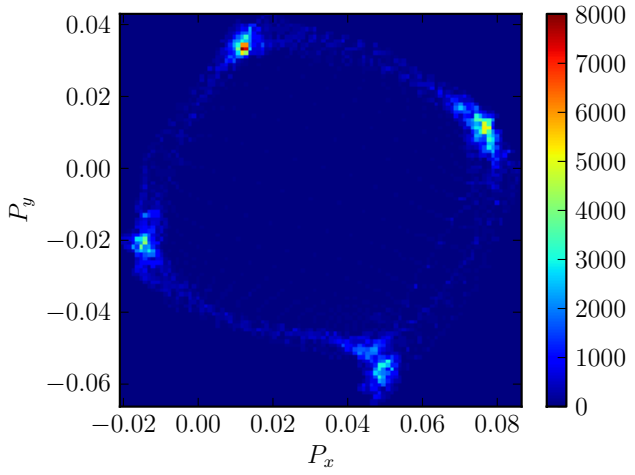

Figure 3.13.: Two-dimensional density plot of the polarization distribution. The color bar shows the probability density of the polarization values. The x-axis polarization offset is $\bar{P}_x = 3.55\%$, and the y-axis polarization offset is $\bar{P}_y = 0.77\%$.

due to the offsets of the MCPs, which are now simply estimated from the mean polarization vector, which is $(\bar{P}_x, \bar{P}_y)$ =(0.0355,0.0077). The calibration procedure is

$$\mathbf{P}' = \begin{pmatrix} P'_x \\ P'_y \end{pmatrix} = \begin{pmatrix} P_x - \bar{P}_x \\ P_y - \bar{P}_y \end{pmatrix}. \tag{3.23}$$

The amplification asymmetry of the four MCPs strongly depends on the applied high voltage, which is adjusted from time to time as the performance of the MCPs degenerates with time. Thus, a new calibration is required after each increase of the MCPs acceleration voltage, but more frequent calibration is advisable, since it also corrects other instrument-related asymmetries, e.g. those of the electron-optical path through the lenses.

In a next step, we estimate the amplitude of the polarization. Since the saturated magnetization is uniform when the temperature is stable, the magnitude of the polarization is the same in all domains and the histogram of the polarization magnitude should show a single sharp peak. The histogram extracted from the data in Fig. 3.12 is shown in Fig. 3.14. Assuming Gaussian noise in the data, we can fit the histogram with a Gaussian peak to precisely determine the mean polarization magnitude $|\mathbf{P}'|$, which in this case is $|\mathbf{P}'|$ =4.6%.

Finally, it is possible to represent the two-dimensional polarization vector distribution $\mathbf{P}'$ as a false color image in the HSV (Hue, Saturation, Lightness) color space. At first, we define the color-wheel, which is shown in Fig. 3.15(b). Different colors represents different magnetization directions, and the saturation is proportional to

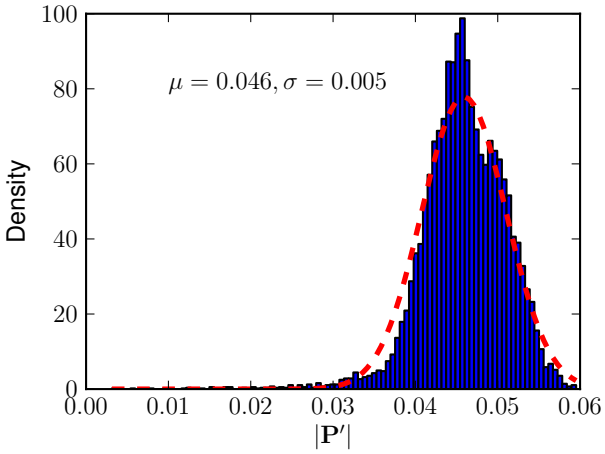

Figure 3.14.: Histogram of the polarization magnitude of Landau structures. $\mu = 0.046$ is the mean value and $\sigma = 0.005$ is the standard deviation.

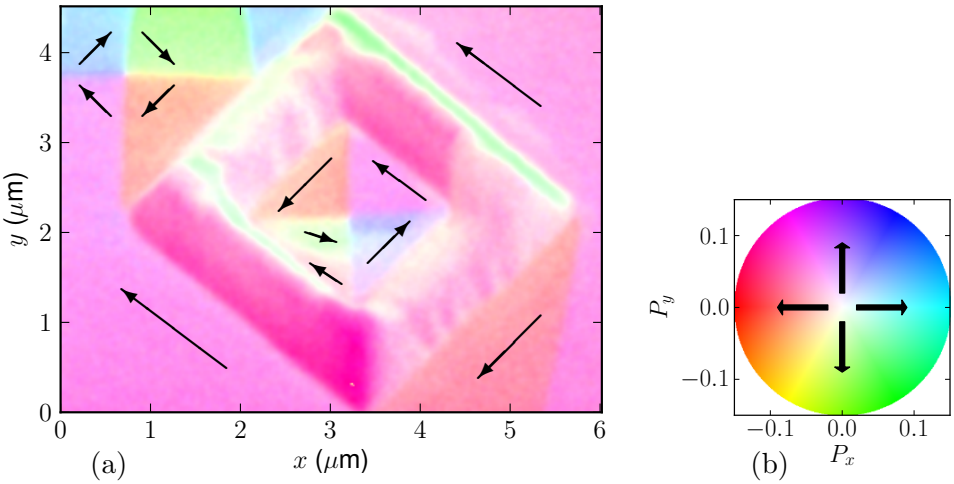

Figure 3.15.: False color representation of SEMPA images of Landau structures after MCPs calibration. (a) The polarization vector image and (b) the color-wheel translating the HSV color space into the polarization space.

the magnitude of $\mathbf{P}'$. The false color representation of the data in Fig. 3.12 after the MCPs offset calibration based on Fig. 3.13 is shown in Fig. 3.15(a).

From Fig. 3.15(a) we find that not only the magnetization can result in the polarization, but also topographic effects seemingly generate polarization contrasts (see Section 3.4.2). The topographic contrast can even exceed the contrast of magnetic origin. An example is the bright green line at the upper right border of the frame in Fig. 3.15(a).

4. Results

It has been revealed by Ding et al. [22] several years ago that both the AFM and the FM state can coexist in single-crystalline FeRh thin films with MgO or Au capping layers. Baldasseroni et al. [23] further indicated that FM domains existed at the surface of the single-crystalline FeRh thin films with an Al capping layer. In order to investigate the intrinsic surface magnetic properties of FeRh, single-crystalline FeRh thin films will be prepared both ex-situ and in-situ without any capping layer. Both bulk and surface magnetic phase transition are analyzed by SEMPA and MOKE, respectively. The details of sample preparation methods and the measurement results are given in this chapter.

4.1. Ex-situ preparation method

In this section, the ex-situ sample preparation method for single-crystalline FeRh thin films on MgO(100) is described. Two samples are prepared, one has a Rh-rich surface, the other an Fe-rich surface. Both samples are transferred trough air without capping layer into the NSCT. After the transfer, the contamination and oxidation of both Fe or Rh-rich surfaces of the FeRh thin films are analyzed by AES. At last, the magnetic properties of both samples are measured by MOKE or SEMPA.

4.1.1. Ex-situ sample preparation

It is well known that Fe can be epitaxially grown on MgO(100), whereas this is not possible for Rh because of the large mismatch between the lattice constants of MgO(100) and metallic Rh. Furthermore, Rh does also not grow epitaxially on Fe for the same reason. In contrast, the mismatch between the lattice constants of FeRh and MgO is small, allowing to achieve single-crystalline growth of FeRh on MgO(100). Lommel [52] has shown that FeRh thin films can be prepared by subsequently depositing layers of Fe and Rh on SiO_2 and applying high-temperature post-annealing, However, the thus prepared FeRh thin films on SiO_2 are polycrystalline. In order to identify the conditions to prepare single-crystalline FeRh films on MgO(100) by thermal evaporation from a single e-beam evaporator with several crucibles, in this work many samples have been prepared with different grown conditions.

MgO(100) substrate preparation by high temperature annealing

The commercial MgO(100) substrates are first cleaned with isopropanol in an ultrasonic bath. Then the substrate is transferred into MBE system. In principle, even if MgO is cleaved in air, the surface of MgO is full of carbon contamination. This is even more the case for air-exposed and polished surfaces. In order to remove the contamination, the MgO substrates need to be annealed at high temperature in UHV [83].

Here, the MgO substrates are annealed at 600°C in UHV for 1 hour. After annealing, a LEED pattern of the MgO(100) surface can be obtained, which is shown in Fig. 4.1. The lattice constant of MgO, which is estimated from the LEED pattern at 106 eV and 132 eV, is 4.05 Å and 4.07 Å, respectively. However, the lattice constant of MgO given by the literature is 4.21 Å, which is about 1% larger than the estimated results from the LEED pattern. Because MgO is an insulator, the surface charges up during the LEED measurements. Comparing the estimated lattice constants and the real lattice constant, we further estimate the potential due to charging to be -7.9 V and -8.6 V at 106 eV and 132 eV, respectively. Nevertheless, LEED patterns of clean MgO surfaces could be observed for higher electron energies in the range between 100 and 300 eV.

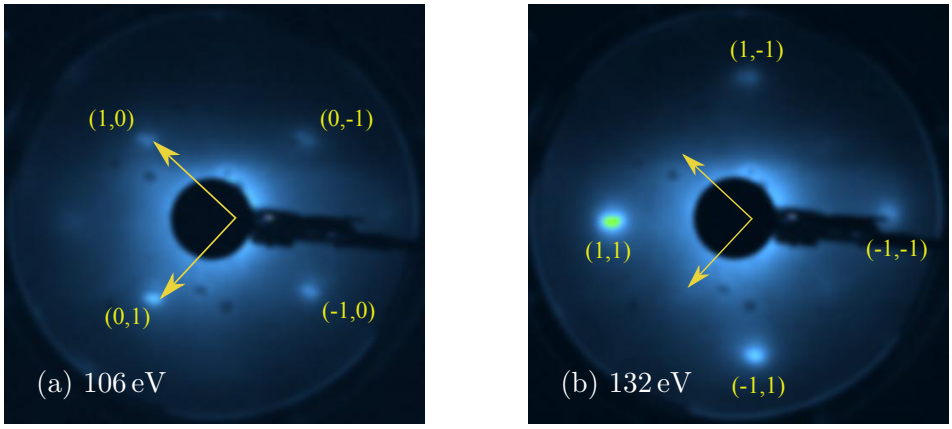

Figure 4.1.: LEED pattern of a clean MgO(100) surface (a) at 106 eV and (b) at 132 eV. The asymmetry of the spot intensities originates from an accidental and partial metallic coating of the LEED screen. The arrows represent the reciprocal unit vectors of the MgO(100) surface.

Epitaxial growth of Fe on MgO(100)

At room temperature, the lattice constants of MgO and bcc Fe are 0.421 and 0.287 nm, respectively. The lattice constant mismatch is less than 4%, if the [100] axis of the bcc cube of Fe is rotated by 45° with respect to the [100] axis the MgO structure. The growth mode of Fe on MgO(100), 2D (layer-by-layer) or 3D (island) growth, depends on the growth temperature. The temperature for Fe on MgO to overcome the Schwoebel barrier[84, 85], which give rise to pyramid-like island growth, is estimated to be between 400-450 K [86]. With increasing growth temperature the Fe pyramid islands on MgO increase in the lateral size and finally coalesce to form an extended and ordered thin film.

In a the first step, three Fe thin films are prepared by thermal evaporation on high-temperature annealed MgO(100) substrates at different growth temperature in order to investigate the temperature effect on the growth. The thickness of the Fe films is fixed to 10 nm, but the growth temperatures are room temperature, 450, and 600 K, respectively. After cooling down to room temperature, LEED is performed in order to analyze the surface order. LEED patterns could only obtained when the Fe growth takes place at 600 K (see Fig. 4.2). Although most of the contamination of the MgO(100) surface can be removed by high-temperature annealing, there still seems to be a significant number of defects indicating that the C contamination could not be removed completely. These defects and C contamination strongly affect the the epitaxial growth of Fe. Hence, only at 600 K the Fe atoms have enough energy to overcome the Schwoebel barrier (and possibly detach from remaining C contaminations on the initial MgO surface) to form a film with a smooth and ordered surface allowing for the observation of clear LEED patterns. The lattice

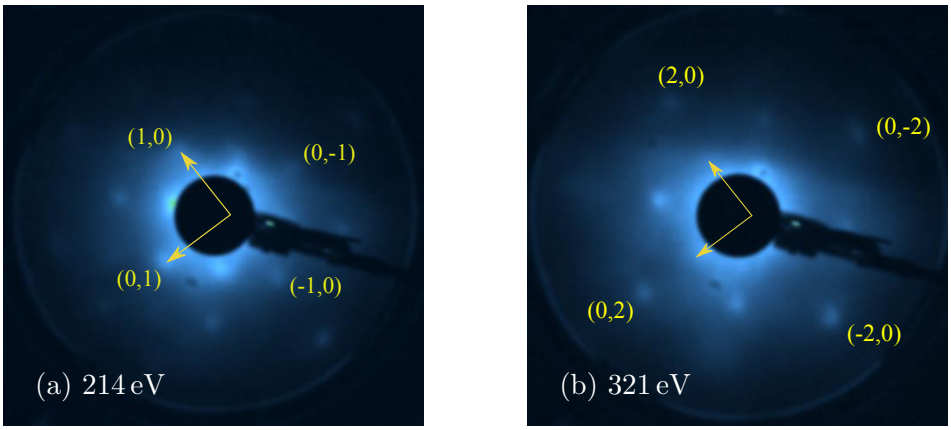

Figure 4.2.: LEED pattern of Fe/MgO(100) grown at 600 K (a) at 214 eV and (b) at 321 eV. The arrows represent the reciprocal unit vectors of the Fe(100) surface.

constant of Fe, which is estimated from the LEED pattern at 214 eV and 321 eV, is 2.46 Å and 2.63 Å, respectively. However, the lattice constant of Fe in the bulk given by the literature is 2.87 Å, which is about 10% larger than the estimation results from the LEED pattern. Comparing the estimated lattice constant and the lattice constant in the bulk, we further estimate the potential due to charging to be -56.8 V and -51.4 V at 214 eV and 321 eV, respectively. Here, we find that a large negative potential is built up by charging, which is due to the poor contact between the thin film and ground.

Deposition Rh on Fe/MgO(100)

After the growth of the single-crystalline Fe thin film another layer of Rh is deposited at 600 K. Just after the Rh deposition, no LEED pattern can be observed anymore, and XPS shows that the surface only contains Rh, but no Fe. Obviously 600 K is not high enough to intermix two layers of Fe and Rh. Hence, the samples need to be further annealed at higher temperatures to let the Fe and Rh atoms interdiffuse and to form the ordered FeRh alloy. After the sample is annealed at 900 K for two hours, XPS reveals that Fe has diffused to the surface. Although no LEED pattern could be obtained immediately after the Rh deposition, clear LEED patterns are observed at 106 and 229 eV after two hours annealing at 900 K, see Fig. 4.3. It is concluded that upon annealing, the deposited material undergoes a structural phase transition from disordered to an ordered structure. The lattice constant of FeRh, which is estimated from the LEED pattern at 106 eV and 229 eV, is 2.67 Å and 2.70 Å, respectively. However, the lattice constant of FeRh in the bulk

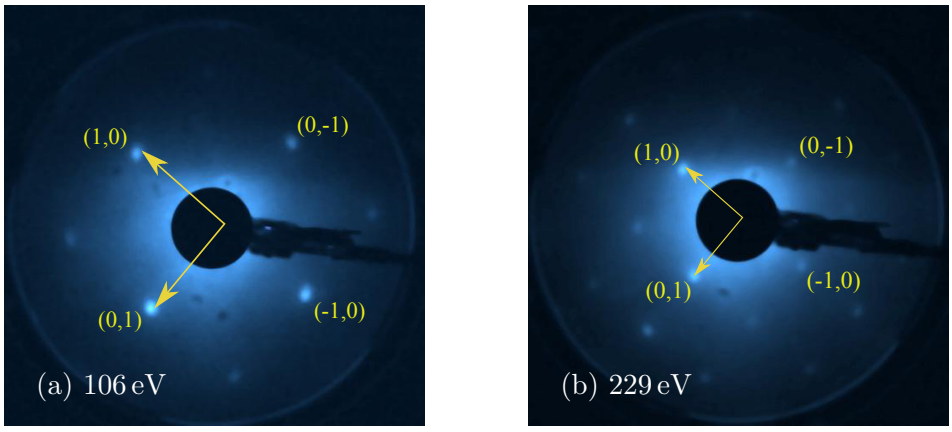

Figure 4.3.: LEED patterns of FeRh/MgO(100) after high-temperature annealing (a) at 106 eV and (b) at 229 eV. The arrows represent the reciprocal unit vectors of the FeRh(100) surface.

given by Zsoldos is 2.99 Å [87], which is about 10% larger than the estimated results from the LEED pattern. If the lattice constant of the FeRh thin film is assumed to be the same in the bulk, we further estimate the potential due to charging to be -21.5 V and -42.3 V at 106 eV and 229 eV, respectively.

Chemical composition of FeRh thin film surface

The first-order magnetic phase transition only exists in FeRh alloys with a composition close to $Fe_{50}Rh_{50}$ [88]. Hence, the chemical composition will here be analyzed by XPS.

The molecular density of a single-element thin film C is the number of atoms per cm^2,

$$C = \frac{\rho t N_A}{M}, \tag{4.1}$$

where ρ is the density, t is the thin film thickness, $N_A = 6.022 \times 10^{23} \mathrm{mol}^{-1}$ is Avogadro constant, and M the atomic weight.

At room temperature, the density of Fe and Rh are 7.86 and 12.4 g/cm^3, respectively, and the atomic weights are 55.847 and 102.9055 respectively. From these numbers we can calculate that for a thickness ratio of $t_{Fe} : t_{Rh} = 1 : 1.17$, the atomic ratio of the molecular densities is $C_{\mathrm{Fe}} : C_{\mathrm{Rh}}$=50%:50%. Thus, we can control the composition of the final alloy film by choosing the proper film thickness ratio of the Fe and Rh films. In addition, the lattice constant of FeRh only changes by less than 2% when the atomic concentration changes by 20% [89], and the lattice constant difference between bcc Fe and CsCl-type FeRh is less than 5%. Hence, the thickness of the resulting FeRh alloy film is about two times the thickness of the Fe layer.

This procedure for the determination of the alloy composition depends on the accurateness of the quartz crystal sensors, which is estimated be of the order of 10% in the best case. For this reason and since we are also interested especially in the surface atomic concentration, the composition of the films are further analyzed by the XPS or AES.

After optimizing the preparation of single-crystalline FeRh thin films on MgO(100), two samples (called S1 and S2) with a FeRh thickness of 40 nm are made under the same procedure: The MgO(100) substrate is cleaned by high-temperature annealing. Then 20 nm Fe and 23 nm Rh are deposited at 600 K one by one. Afterwards, the samples are annealed at 900 K for two hours. Both samples are single-crystalline FeRh thin films and have the similar LEED pattern after annealing.

In order to obtain the chemical composition of the sample surfaces, XPS is performed as shown in Fig. 4.4. The binding energy of the main Fe XPS peaks are 708.1 and 721.1 eV, and the binding energy of the main Rh XPS peaks are at 307.0

and 311.7 eV, and 496.2 and 521.0 eV [90]. The X-ray energy is 1486.6 eV when using the Al anode and the work function of the energy analyzer is 4.324 eV. In principle we should obtain peaks at 761.2, 774.2, 1175.3, 1170.6, 986.1, and 961.3 eV in Fig. 4.4. However, we observe the peaks at 766.3, 779.3, 966.0, 991.0, 1175.5, and 1180 eV in Fig. 4.4(a), and at 762.2, 776.0, 961.5, 986.6, 1171.6, and 1175.6 eV in Fig. 4.4(b). For both samples, due to charging effects related to the insulating MgO substrate, the spectra are shifted by several eV.

Although the spectra reveal different degrees of charging, it is obvious from compar-

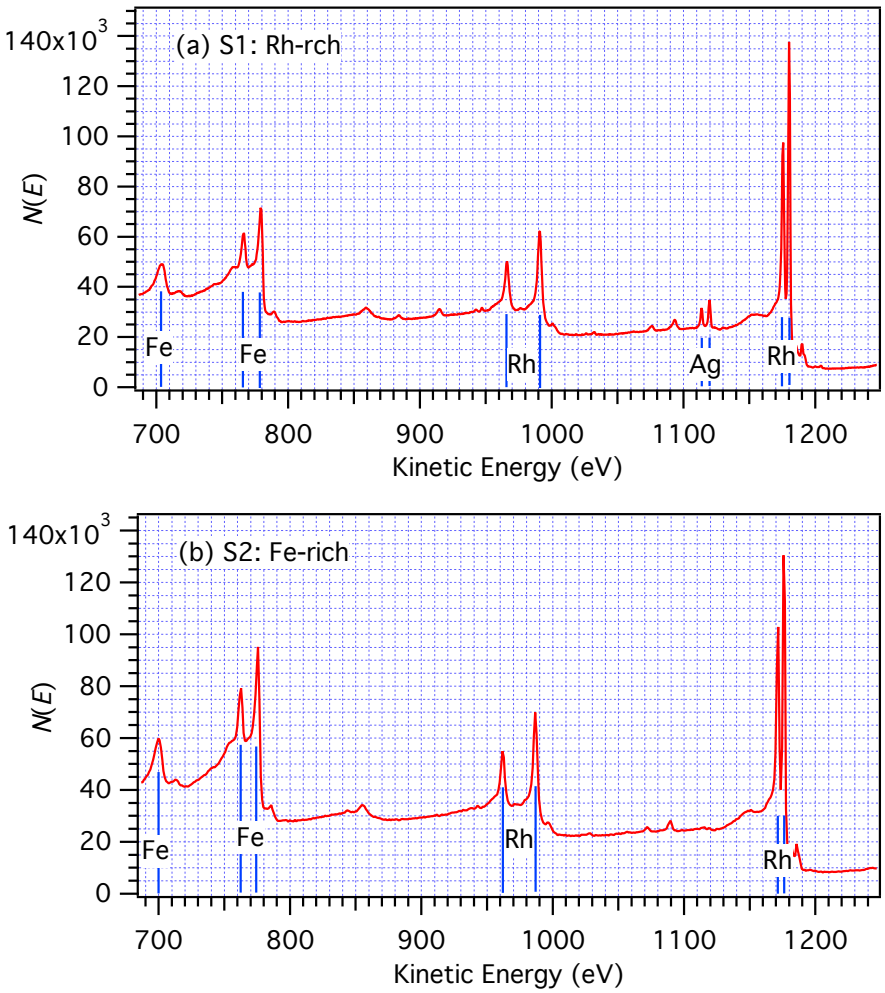

Figure 4.4.: XPS of single-crystalline FeRh thin films on MgO prepared in the MBE system after high-temperature annealing, but before transfer to the NSCT: (a) sample S1 and (b) sample S2. The Ag peaks originate from an accidental Ag coating of the clamps that fix the sample on the sample holder.

ing the Fe peak heights in Figs. 4.4 (a) with (b), that sample S1 has a clearly lower Fe concentration than sample S2. Using CasaXPS, the chemical compositions can be fitted and we find for S1 $C_{\mathrm{Fe}} : C_{\mathrm{Rh}} = 45\% : 55\%$ and for S2 $C_{\mathrm{Fe}} : C_{\mathrm{Rh}} = 52\% : 48\%$. The XPS results reveal for S1 a Rh-rich and for S2 an Fe-rich FeRh surface.

Although the two samples are grown under the same conditions, the atomic concentration difference between them is as large as 7%. One of the possible reasons is that the quartz crystal sensors used to measure the thickness of each layer can have errors, which directly result in non-reproducible concentrations. Therefore, the film growth conditions can be different for two samples, which indirectly can result in different atomic concentrations.

Surface cleaning after transfer through air

It is well known that pure Fe thin films undergo oxidation and contamination in air. The oxidation process is complicated and strongly depends on temperature and humidity. On the other hand, pure Rh thin films are rather stable and are less susceptible to oxidation, but they can be contaminated with nitrogen and organic compounds when exposed to air. Therefore, the bulk of FeRh thin films will not be easily oxidized in air at room temperature, but the surface Fe atoms may be oxidized and iron oxides may form. Contamination due to physisorption of gases like O_2, CO_x, N_2 etc., which is limited to the surface region, can be removed by high temperature annealing. Iron oxides are expected to be much more stable and to resist annealing.

In order to investigate the oxidation of FeRh surface due to the transfer through air, both samples S1 and S2 are analyzed in the NSCT by AES immediately after the transfer and after two annealing cycles at 900 K for two hours, respectively. The results are shown in Fig. 4.5 and Fig. 4.6. Before annealing, the surfaces of both S1 and S2 are contaminated by C and O, but S2 is more strongly contaminated with O than C. After the first annealing, the O peaks of S1 have disappeared, but the C peak remained. On the other hand, the C peak of S2 has disappeared, but the O peak is still very large. The second annealing cycle cannot remove the C contamination of S1 or the O contamination of S2, too.

For a more quantitative analysis of the spectra we employ the Auger sensitivity factors S_{x} (x = Fe, Rh, C, O) of Ref. [64] tabulated in Table 3.1. The sensitivity-corrected intensities $I_{\mathrm{x}}/S_{\mathrm{x}}$, where I_{x} is the measured peak-to-peak height, are used to estimate the relative contributions of the elements to the spectra, see Chapter 3.2.4. Averaging the sensitivity-corrected intensities $I_{\mathrm{x}}/S_{\mathrm{x}}$ of three Fe peaks and two Rh peaks is used to reduce the statistical error. The results are compiled in Table 4.1 and summarized as follows:

S1 Before annealing, we have $X_{\mathrm{Fe}} : X_{\mathrm{Rh}} : X_{\mathrm{C}} : X_{\mathrm{O}} = 21\% : 28\% : 21\% : 21\%$. After the first annealing, the O is removed and we have $X_{\mathrm{Fe}} : X_{\mathrm{Rh}} : X_{\mathrm{C}} = 32\% :$

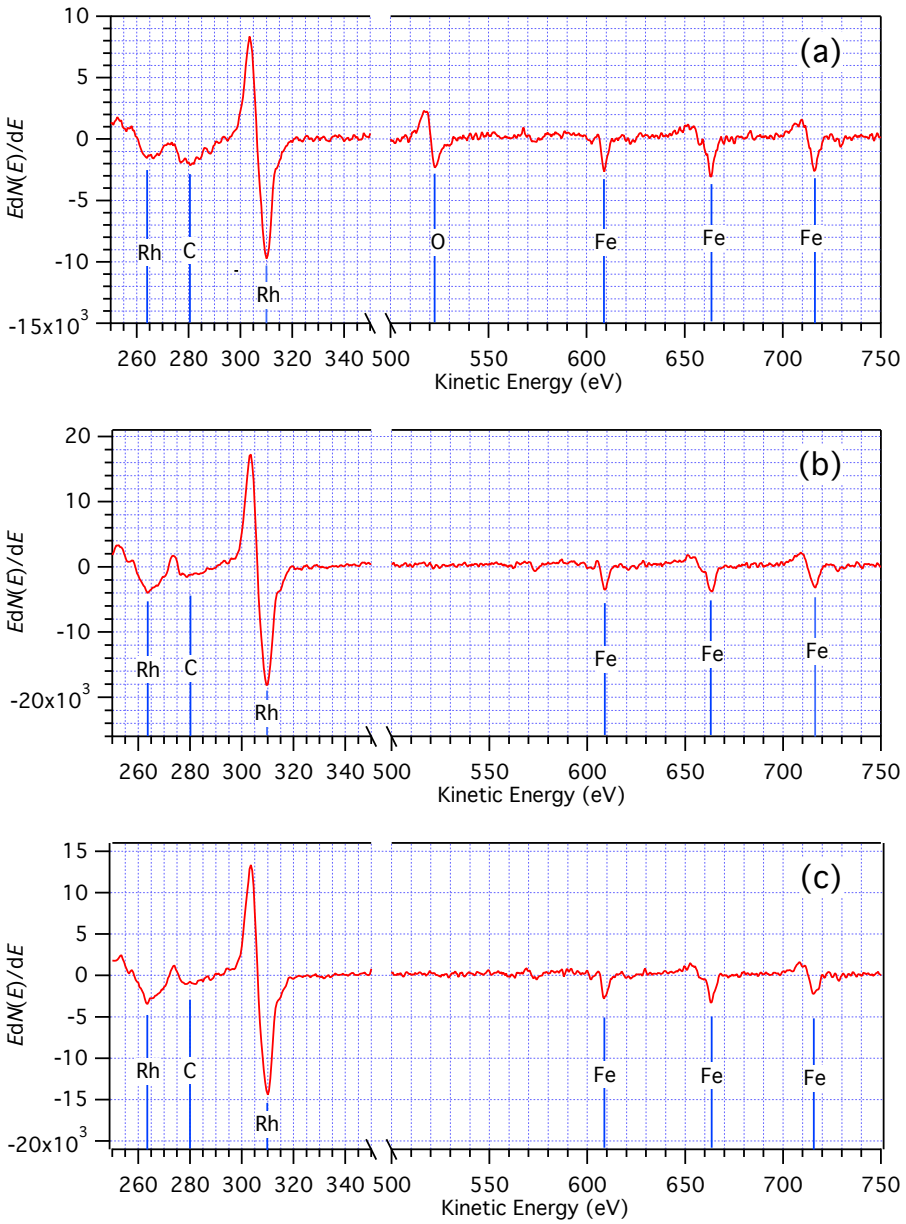

Figure 4.5.: AES of ex-situ prepared single-crystalline Rh-rich FeRh thin films on MgO(100) (S1) after transfer through air (a) before annealing, (b) after first annealing, and (c) after second annealing.

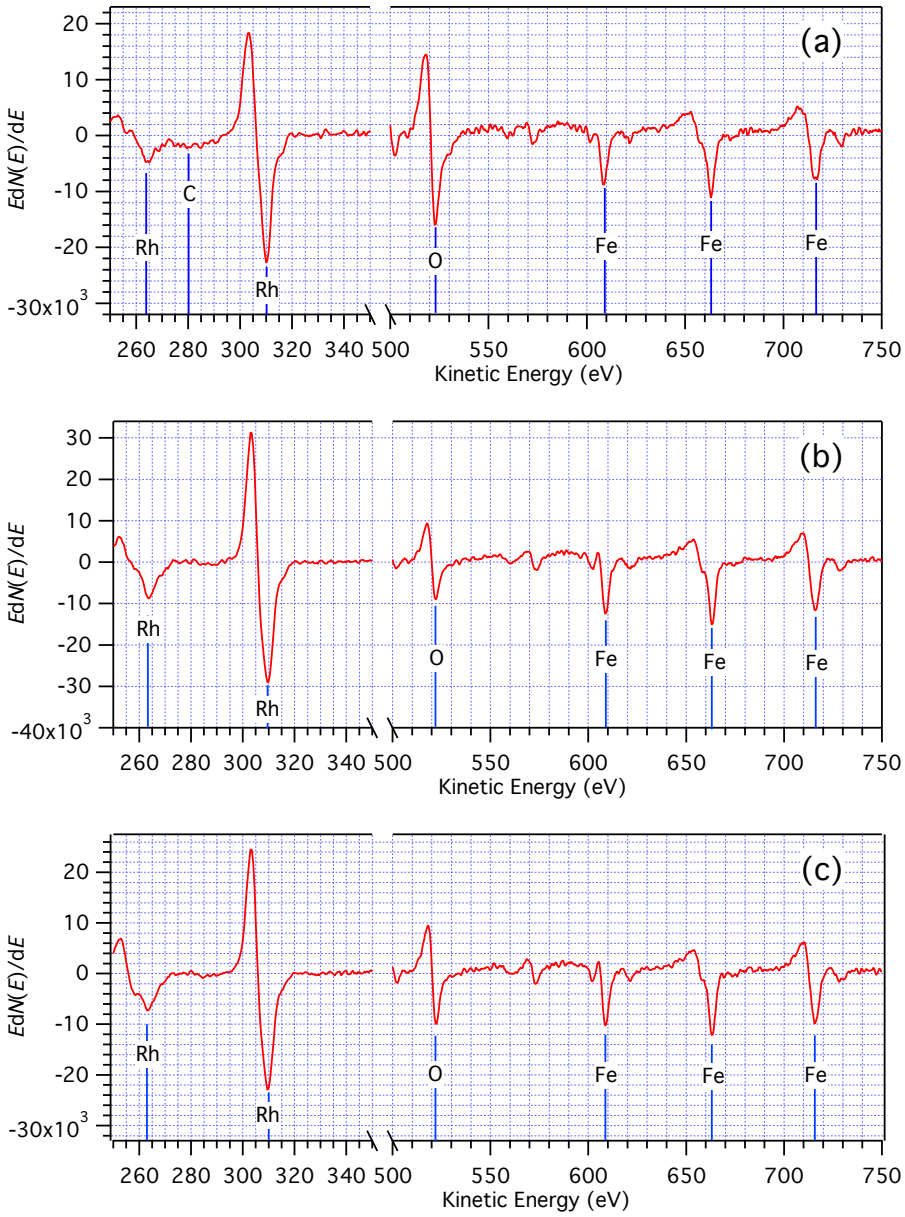

Figure 4.6.: AES of ex-situ prepared single-crystalline Fe-rich FeRh thin films on MgO(100) (S2) after transfer through air (a) before annealing, (b) after first annealing, and (c) after second annealing.

45% : 23%. Comparing Figs. 4.5 (a) with (b), we observe that the peak shape at around 280 eV has changed. This is most likely due to the disappearing of the C contribution from CO_x, which can be desorbed, but a small C peak, possibly due to chemisorbed C species, remains. After the second annealing, the surface atomic concentration does not change so much, we have $X_{\mathrm{Fe}} : X_{\mathrm{Rh}} : X_{\mathrm{C}} = 32\% : 47\% : 21\%$. The increase of the C contribution during the first annealing from 23% to 21% is most likely within the statistical error. The ratio of Fe to Rh is about $X_{\mathrm{Fe}} : X_{\mathrm{Rh}} = 42\% : 58\%$; the surface of the sample S1 is a Rh-rich surface.

S2 Before annealing, we have $X_{\mathrm{Fe}} : X_{\mathrm{Rh}} : X_{\mathrm{C}} : X_{\mathrm{O}} = 29\% : 20\% : 8\% : 43\%$. After the first annealing, C is removed completely and the O contribution is strongly reduced. We have $X_{\mathrm{Fe}} : X_{\mathrm{Rh}} : X_{\mathrm{O}} = 42\% : 33\% : 25\%$ after the first annealing cycle and $X_{\mathrm{Fe}} : X_{\mathrm{Rh}} : X_{\mathrm{O}} = 39\% : 31\% : 30\%$ after the second annealing. The increase of the O contribution from 25% to 30% is most likely within the statistical error. The ratio of Fe to Rh is about $X_{\mathrm{Fe}} : X_{\mathrm{Rh}} = 39\% : 31\% = 56\% : 44\%$; the surface of sample S2 is a Fe-rich surface.

From this analysis, we find that the Fe-rich FeRh surface can easily be oxidized in air, while the Rh-rich FeRh surface only physisorbes oxygen and carbon. Oxygen, which contaminates the Rh-rich FeRh surface can be desorbed by the high-temperature annealing, but not the carbon.

Table 4.1.: Spectral composition of samples S1 and S2 before annealing and after two subsequent annealing cycles.

	Element	Before annealing		First annealing		Second annealing	
		E (eV)	X	E (eV)	X	E (eV)	X
S1	Fe	609 663.5 716	21%	609 663.5 716	32%	608.5 663 715.5	32%
	Rh	264 310	28%	263.5 309.5	45%	263.5 310	47%
	C	280.5	21%	279	23%	280	21%
	O	522.5	21%				
S2	Fe	608.5 663 717	29%	609 663 716	42%	609 663 715.5	39%
	Rh	265 310	20%	263.5 309.5	33%	263 310	31%
	C	280.5	8%				
	O	523	43%	522	25%	522	30%

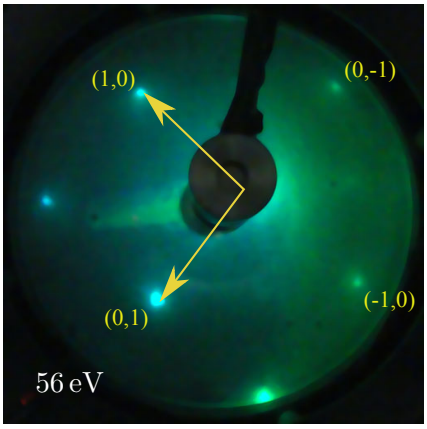

Figure 4.7.: LEED pattern of the Rh-rich FeRh thin film at 56 eV after surface cleaning. The asymmetry of the spot intensities originates from a small tilt angle between the sample surface normal and the LEED electron gun axis. The arrows represent the reciprocal unit vectors of the FeRh(100) surface.

Though we could not obtain LEED patterns of both samples before surface cleaning, a LEED pattern of the Rh-rich sample S1 can be obtained again at 56 eV after surface cleaning (see Fig. 4.7). However, no LEED pattern of the Fe-rich sample S2 can be obtained after surface cleaning. As anticipated, the Fe-rich surface of sample S2 is oxidized and therefore disordered. But the Rh-rich surface is only slightly contaminated by C, and thus exhibits an ordered surface after annealing. The lattice constant of Rh-rich FeRh thin film on MgO(100), which is estimated from the LEED pattern at 56 eV, is 3.00 Å. The estimated lattice constant of Rh-rich FeRh agrees well with the lattice constant in the bulk given by Zsoldos that is 2.99 Å [87]. Here, there is no strongly charging effect during LEED measurement of the Rh-rich sample, because a better contact the thin film and the ground is made during the sample transfer between two separate UHV systems using different clamps between the thin film and the sample holder.

In summary, we could only obtain LEED patterns from Rh-rich FeRh thin films after surface cleaning.

4.1.2. Magnetic properties of ex-situ prepared FeRh films

In a next step MOKE measurements are performed in-situ to measure the bulk magnetic properties, which are accessible because the MOKE probing depth is of the order of the film thickness. On the other hand, the probing depth of SEMPA is only a few atomic layers and will allow measuring the surface magnetic properties, providing the remaining surface contamination, especially the oxides, allows for a magnetic surface and SEMPA measurements at all.

MOKE results

The samples are first measured by MOKE at room temperature. Then they are cooled by liquid nitrogen and the measurements are repeated. Figure 4.8(a) reveals a magnetic hysteresis loop of the Rh-rich FeRh film at room temperature, but not at 170 K. This is in agreement with a AFM to FM phase transition between 170 and 293 K. The coercivity of S1 at room temperature is 16 mT. In contrast, Fig. 4.8(b) shows magnetic hysteresis loops of sample S2 both at room temperature and at 193 K. The coercivity of sample S2 is 26 and 27 mT at 293 and 193 K, respectively. Further MOKE measurements at room temperature along other in-plane directions of both samples show the same coercivity as that of the loops shown in Fig. 4.8, which are measured with the applied field along the MgO[010] direction.

In literature, single-crytalline FeRh thin films on MgO(100) are reported to have uniaxial anisotropy with an in-plane easy axis [14] (see Section 2.3.1). Here, the coercivity of separate-layer-grown Rh-rich FeRh thin films is found to be two times larger than that of sputtered FeRh thin film [14], while the coercivity of separate-layer-grown Fe-rich FeRh thin films is three times larger. The larger coercivity of sample S2 may due to the oxidized surface of the Fe-rich surface, which results in a higher pinning energy.

The MOKE results in Figs. 4.8(a) and (b) reveal that both samples are in a FM state

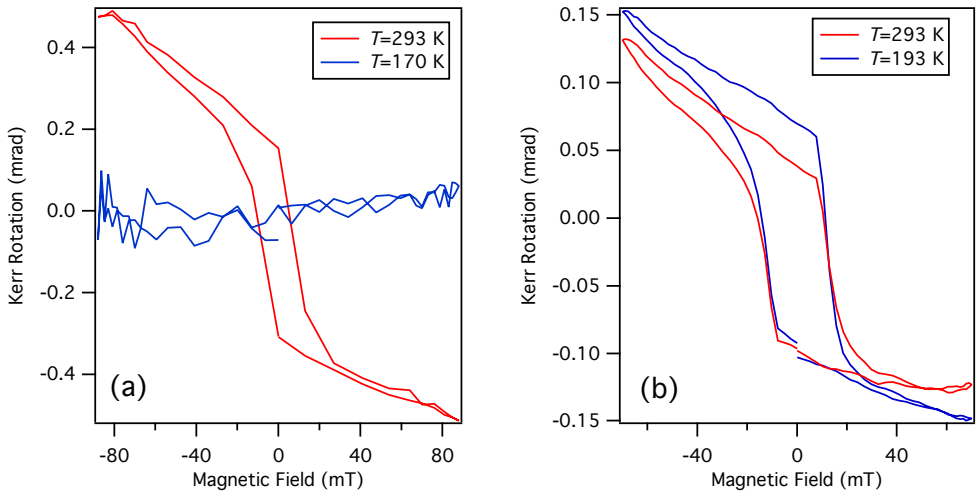

Figure 4.8.: MOKE results of ex-situ prepared samples measured along the MgO(100)[010] direction. (a) Magnetic hysteresis loops of sample S1, which has a Rh-rich surface, at both 293 and 170 K, and (b) for sample S2, which has a Fe-rich surface, at both 293 and 193 K. The MOKE results are taken as the average of three loops in oder to reduce the noise and the zero offset.

at room temperature, but sample S1 is in an AFM state at low temperature, while sample S2 remains FM. The first-order phase transition temperature of sample S1 is below room temperature, which differs from the value of the equiatomic bulk FeRh alloy reported in literature between 310 and 400 K [91, 36, 92].

Shirane et al. [28] and Tu et al. [36] have already pointed out that the Fe-rich FeRh alloy is FM and shows no first-order magnetic transition from AFM to FM (see Fig. 2.3 in Section 2.1). Besides, Hofer et al. [32] further showed that both the magnetic moment and the Curie temperature decease, if the atomic concentration of Rh increases from 50% to 63% for Rh-rich FeRh alloy, while the first-order transition temperature increases as the Rh atomic concentration increases (see Fig. 2.2 and Fig. 2.3 in Section 2.1). The MOKE results of the Rh-rich sample S1 only partially agree with Hofer et al. [32], because they report a first-order transition temperature for $Fe_{40}Rh_{60}$ of 347 K, while sample S1 has a much lower transition temperature. The MOKE results of the Fe-rich sample S2 are in accordance with Shirane et al. [28].

SEMPA results

Although MOKE could be performed on both samples, SEMPA measurements were successful only for sample S1. As anticipated, the Fe-rich surface of sample S2 is oxidized and therefore nonmagnetic, thus not revealing magnetic domains at the surface. The thickness of the oxide layer is thick enough (i.e. more than 2-3 atomic layers) to prevent spin-polarized secondary electrons to escape from the bulk. As a result, we just could obtain the magnetic domain structure of the Rh-rich surface of sample S2 at different temperatures, as shown in Fig. 4.10. SEMPA measurements are first performed at room temperature, then after heating the sample up to 450 K, cooling to room temperature, cooling further to 160 K by liquid nitrogen, and finally heating to 450 K in several steps. During each measurement, the sample's temperature is keep constant by a Lakeshore temperature controller.

The data in Fig. 4.10 is presented in a false color representation. The color-wheel is shown in Fig. 4.9 and defines polarization values in the range ± 0.1 (white in the center corresponds to zero polarization and a saturated color at the circumference of the color wheel indicates a polarization in the direction coded by the color with a magnitude of 0.1). The domain structure in Figs. 4.10(a) to (l) does not change so much when the temperature changes from 160 to 450 K. Figures 4.10(a), (e), and (i) are all taken at room temperature but at different steps of the temperature sequence. Their rather similar appearance indicates that neither heating nor cooling induces significant non-reversible changes to the domain struture. Although the MOKE results showed that the bulk of of the Rh-rich FeRh sample is in an AFM state at 170 K, the SEMPA result at 160 K clearly shows a FM state at the surface, see Fig. 4.10(f).

In order to quantitatively analyze the spin polarization of the temperature dependent SEMPA images, the density of the 2-dimensional polarization vector is plotted as a 2-dimensional histogram as shown for the different temperatures in Figs. 4.11(a) to (l). The general structures of the polarization vector densities are similar at all temperatures. There are two peaks on the x-axis. Actually, this is a consequence of the remanent state because during the MOKE measurements a magnetic field has been applied along the x-axis, which is the MgO(100)[010] direction. Hence, a majority of the domain magnetizations are collinear to the MgO(100)[010] direction.

Figures 4.11(a), (e), and (i) confirm that the domain structure hardly changes during the temperature sequence when returning to the same temperature. Although the structure of these histograms is similar, there are little differences in the polarization amplitude. There are many reasons for this observation. First, the the W(100) crystal of the SPLEED detector tends to become contaminated over time, which reduces the asymmetry of the diffracted beams even if the polarization of the incoming electron beam is constant. Second, every SEMPA measurement takes 22 minutes and both heating and cooling between the measurements to reach the next temperature value last several hours to achieve a stable temperature. Thus, the whole measurement of the 16 images took three days. During this period it is likely that the surface of FeRh film gets more contaminated by the residual gas in the UHV chamber, which will result in a lower polarization of the surface. But if the W(100) crystal is flashed after each measurement and the time delay between experiments is not so long, then the degradation of the spin polarization is less severe [93]. The average amplitude of the spin polarization derived from the radii of the circular pattern in Fig.4.11 are plotted in Fig. 4.12. Although there is degradation of the spin polarization, e.g. at room temperature, it is clear that the spin polarization decreases as the temperature increases. For instance, all data points

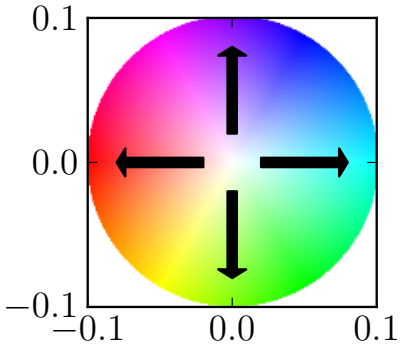

Figure 4.9.: Color wheel for the representation of the SEMPA data of the ex-situ prepared FeRh thin films.

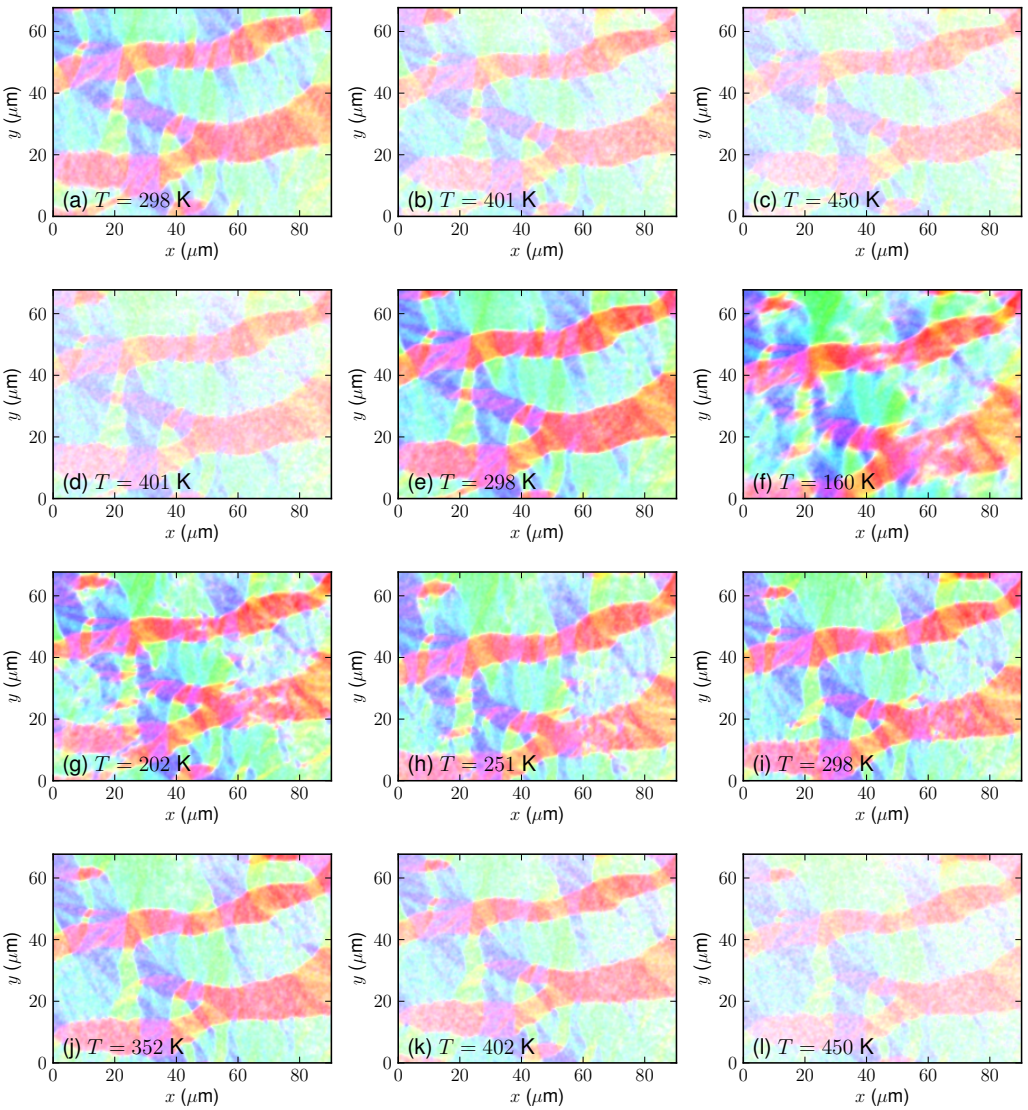

Figure 4.10.: SEMPA images of an ex-situ prepared FeRh thin film with a Rh-rich surface measured at different temperatures as indicated. Images are taken at the same sample spot and in the sequence (a) to (l).

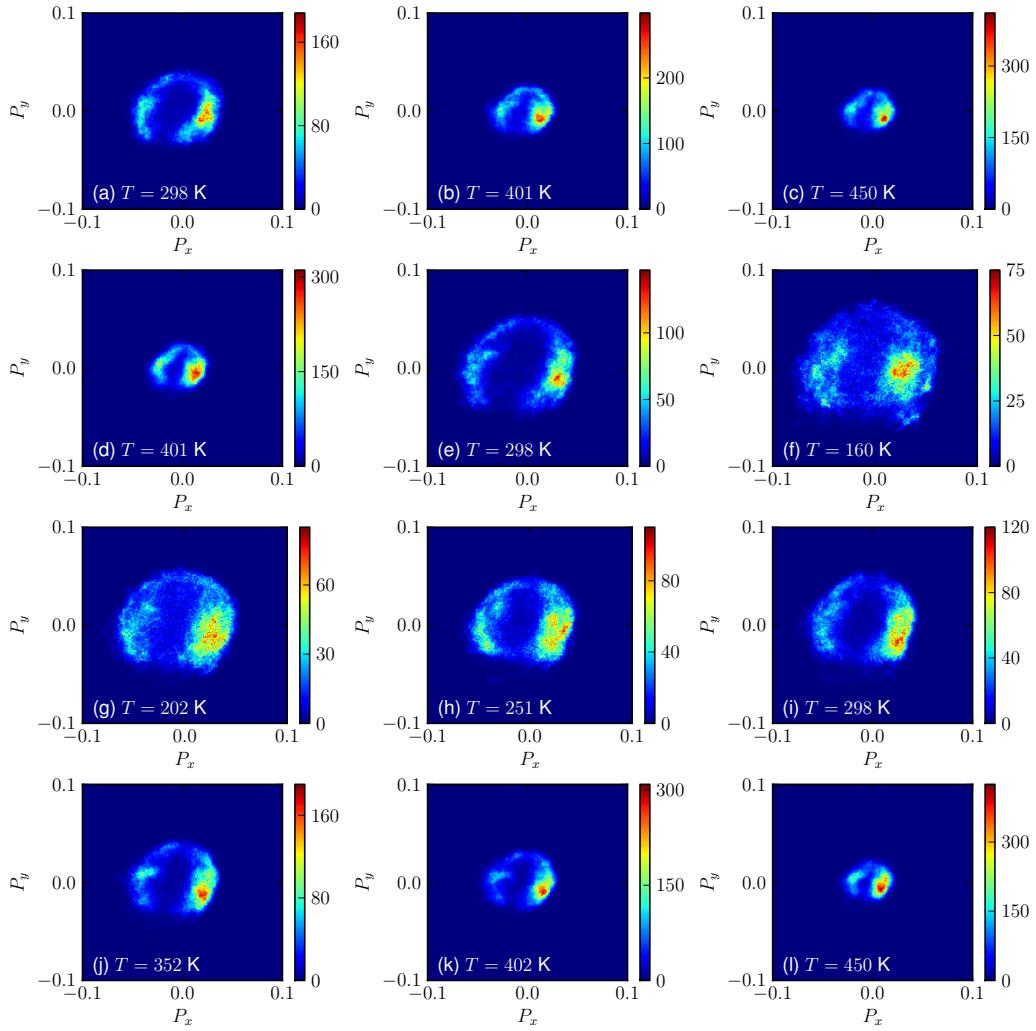

Figure 4.11.: Two-dimensional histograms of the SEMPA images shown in Fig. 4.10, which show the probability density as a function of the polarization vector for the ex-situ prepared Rh-rich FeRh thin film.

at room temperature are clearly higher than those at 450 K. The surface is always in a FM state and shows no magnetic transition, which is in clear contrast to the bulk behavior measured by MOKE that shows a magnetic transition upon cooling to 170 K.

Coexistence of AFM and FM phases in FeRh

Taking together the MOKE and the SEMPA results, it is obvious that the FM and AFM phases can coexist in single-crystalline FeRh thin films on MgO(100) as observed for sample S1 with a Rh-rich surface and at a temperature of 160 K. The SEMPA measurement indicates that the Rh-rich FeRh surface is FM at 160 K, while the bulk is AFM as indicated by the MOKE hysteresis loops.

Although the surface is FM, there are two reasons that no magnetic hysteresis loop of the FM surface can be detected by MOKE at low temperature. One reason could be that the surface anisotropy increases the coercivity to become so large that the magnetic filed generated by the electromagnet of the in-situ MOKE is not sufficient to remagnetize the FM surface. Magnetic surface anisotropy is induced by the symmetry breaking at the surface of the thin film [94]. If we denote the surface anisotropy by K_s and the bulk anisotropy by K_b, then the effective anisotropy is expressed as

$$K_{\text{eff}} = K_{\text{b}} + \frac{K_s}{t}, \tag{4.2}$$

where t is the thickness of the FM layer. Here, we neglect the interface anisotropy between FeRh and MgO. At room temperature, the whole film is FM and the effective anisotropy is dominated by the bulk anisotropy. But at low temperature, only the surface is FM, meaning that the surface anisotropy dominates the effective anisotropy. When t is extremely small, the effective anisotropy can be very large. Hence, the coercivity at low temperature can be much larger than at room temperature, since a larger Zeeman energy is needed to overcome the anisotropy energy in order to reverse the domains.

Another reason is that the thickness of the FM surface layer at low temperature is so small that its contribution to the total MOKE signal is smaller than the sensitivity of our in-situ MOKE setup. In fact, the MOKE signal is rather noisy, which to a large extent is due to mechanical vibrations of the long manipulator at the MOKE position. If the FM surface region is less than 1 nm thick (2.5% of the total FeRh thickness), then its signal is likely to vanish in the noise.

Furthermore, there is no domain wall formation and nucleation when the temperature changes (see Fig. 4.10) though the spin polarization decreases as the temperature increases (see Fig. 4.11). In a SEMPA measurement of a certain material, the spin polarization is proportional to the magnetization for given working conditions. The fact that the spin polarization decreases as the temperature increases indicates that the magnetization also decreases with increasing temperature. Typically, a

change of the magnetization will also modify other energy terms such as the exchange energy, the stray field energy, and the anisotropy. As a consequence, the domain structure is modified to achieve a new equilibrium state that minimizes the total magnetic energy. But if there are a lot of defects on the surface, the domain walls are pinned and the domains cannot easily relax. For the ex-situ prepared samples, we expect defects created by the contamination occurring during air exposure. Although most of the contamination can be removed by high-temperature annealing, some defects seem to remain. Hence, the domain walls of the Rh-rich FeRh surface are pinned by the defects and no domain wall formation and nucleation is observable.

From the 2-dimensional histogram of the SEMPA images, we can further estimate the values of the spin polarization as a function of temperature, which is shown in Fig. 4.12. Although the bulk shows a magnetic phase transition, the surface behaves like the usual ferromagnet. One possible explanation is that the AFM Fe-Fe interaction at the surface is slightly different from the bulk (see Section 2.2). Actually, the thin film's first-order transition temperature in the bulk is lower than reported for bulk FeRh alloy samples [16, 28]. When the Fe-Fe exchange interaction decrease from -1.1 to -1.07 mRy, the first-order transition temperature decreases from 332 to 230 K (see Fig. 2.12 in Section 2.2.2). If the Fe-Fe exchange interaction further decreases, e.g. to -1.06 mRy, then the first-order phase transition does not take place anymore (see Fig. 2.12 in Section 2.2.2). The value of the the Fe-Fe exchange interaction depends on subtle details of the crystalline and electronic structure and is thus very difficult to predict. Basically, ab-initio calculations of a specific local configuration are needed. Without such calculations one can only speculate about the reasons that affect the interaction strength. The Fe-Fe interaction in

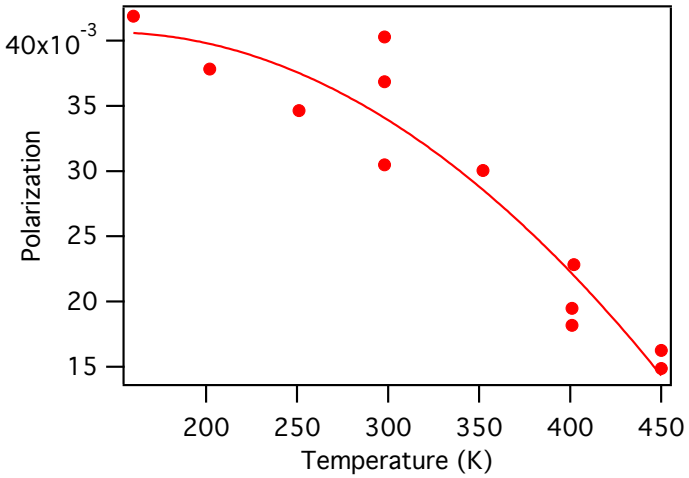

Figure 4.12.: Temperature dependent spin polarization of an ex-situ prepared Rh-rich FeRh film on MgO(100).

the bulk of our films is probably reduced due to strain induced at the MgO/FeRh interface and in this manner gives rise to the observed lower first-order transition temperature.

4.2. In-situ preparation method

For the ex-situ sample preparation the surface magnetic properties of the FeRh thin films are inevitably affected by contamination or even oxidation. In order to investigate the intrinsic surface magnetic properties, the samples need to be prepared and measured in-situ without intermediate vacuum break. In the course of this work the NSCT was upgraded to provide the required tools to prepare single-crystalline FeRh thin films on MgO(100) and measure both the bulk and the surface magnetic properties in-situ without breaking the UHV.

Grazing incident X-ray scattering of a 50 nm FeRh thin film on MgO(100) with a 2 nm thick MgO capping layer revealed that the bulk of the FeRh film is mostly strained due to the substrate, while the strain is relaxed the surface [95]. Hence, the surface magnetic properties of thinner FeRh films is expect to be different compared to the 40 nm thick FeRh films that were discussed in the previous section.

In this section, the method to prepare thin single-crystalline FeRh films on MgO(100) with a thickness of 10 nm is first described. Then the chemical composition is analyzed by the AES, and the bulk magnetic properties are measured by MOKE. Finally, SEMPA is performed to investigate the intrinsic surface magnetic properties of FeRh thin films.

4.2.1. In-situ sample preparation

Compared with the MBE system used for the ex-situ preparation procedure, there is a technical limitation of the manipulator in the NSCT preparation chamber that cannot heat the sample above 600 K during deposition. Hence, the ex-situ preparation procedure is modified in order to grow single-crystalline Fe layers on MgO(100) at room temperature.

MgO(100) substrate preparation by annealing in O_2

Previous studies on the growth of epitaxial metallic layers on MgO reveal that maybe there still remains a sub-monolayer contamination on MgO after high-temperature annealing, especially C [96, 97]. In order to obtain clean surfaces, the MgO substrates can be annealed in a controlled oxygen atmosphere. In the NSCT, we employ a silver tube oxygen dosing set-up, which controls the oxygen

partial pressure in the chamber by the temperature dependence of the oxygen diffusion through bulk silver. Heating the oxygen filled silver tube increases the amount of O_2 that diffuses into the vacuum chamber.

For in-situ sample preparation, the MgO substrate is first cleaned with isopropanol in an ultrasonic bath. Then the MgO substrate is clamped onto a Mo sample holder. The idea of using clamps is that they make electrical contact to the metallic film on the MgO substrate to ground the sample surface and thus reduce charging effects during AES, LEED, and SEMPA measurements. However, it will turn out that shadow effect at the edge of the clamps leave a gap between metallic film and clamp, such that charging still occurs.

Transferred into the NSCT, the MgO substrate is first degassed at 500 K for several hours until the pressure of the chamber goes down to 1×10^{-10} mbar. Then the sample is annealed in O_2 by slowly increasing the temperature up to 900 K using a resistive heater, which is located in the preparation chamber but not at the deposition position. The oxygen partial pressure is 1×10^{-7} mbar as measured by mass spectrometry, while the residual gas pressure during annealing is less than 5×10^{-10} mbar. After the substrate is annealed in O_2 for one hour, we first stop the oxygen supply and then slowly reduce the substrate's temperature to room temperature. Afterwards, a clear cubic LEED pattern can be observed as shown in Fig. 4.13. The lattice of MgO(100) substrate after high temperature annealing in O_2, which is estimated from the LEED pattern at 148 eV and 200 eV, is 4.15 Å and 4.16 Å, respectively. The lattice constant of MgO given by the literature is about 1% larger than the estimated results from the LEED pattern. Comparing the estimated lattice constants and the real lattice constant, we further estimate the potential due

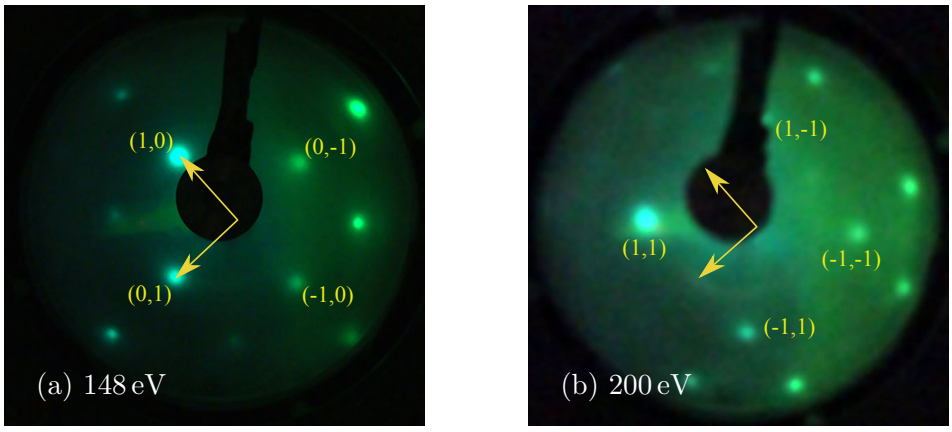

Figure 4.13.: LEED patterns of the MgO(100) surface prepared by high-temperature annealing in O_2. The arrows represent the reciprocal unit vectors of the MgO(100) surface.

to charging to be -4.2 V and -4.7 V at 148 eV and 200 eV, respectively.

Epitaxial growth of Fe on MgO(100)

After a clean MgO(100) surface is obtained, 5 nm Fe are deposited from an e-beam evaporator at room temperature. In order to obtain epitaxial Fe growth at room temperature, a very low evaporation rate between 0.02 to 0.03 Å/s is used. An AES spectrum measured after the Fe deposition is shown in Fig. 4.14. The AES peaks in the reference spectrum of pure Fe are at 600, 654, and 705 eV [64], but we obtain the three peaks at 608.5, 663, and 715 eV. The difference between our measurement and the reference is mainly due to the charging effect of metallic thin layer on the insulating substrate.

In this preparation stage we also obtain cubic LEED patterns, an example taken at a kinetic energy of 201 eV is shown in Fig. 4.15. However, the spots in Fig. 4.15 are rather diffuse compared to those in Fig. 4.13. We attribute this observation to an increased density of defects, i.e. surface roughness, caused by the Fe growth at room temperature. The lattice constant of Fe, which is estimated from the LEED pattern at 201 eV is 2.82 Å. The lattice constant of MgO given by the literature is about 2% lager than the estimated result from the LEED pattern. Comparing the estimated lattice constant and the real lattice constant, we further estimate the potential due to charging to be -6.9 V. Here, we find that a negative potential is built up by charging, which is due to the poor contact between the thin film and ground.

Nevertheless, the LEED patterns reveal that Fe can be grown epitaxially on the

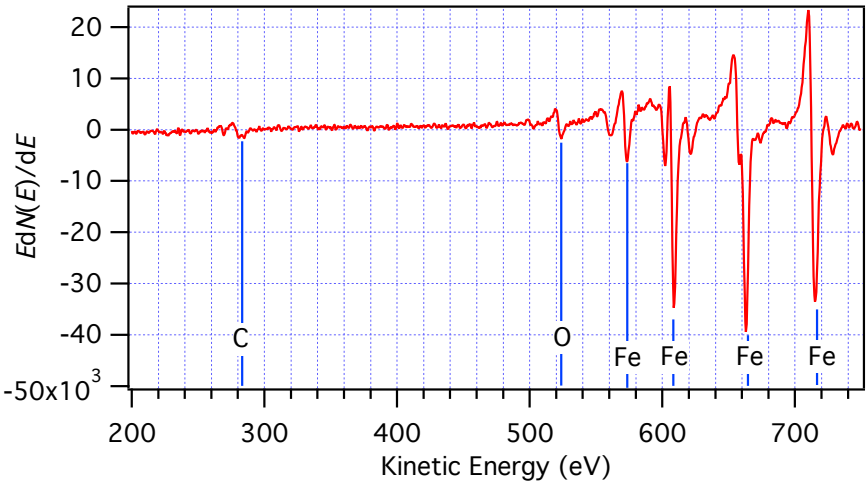

Figure 4.14.: AES spectrum of an in-situ and at room temperature prepared Fe film on MgO(100).

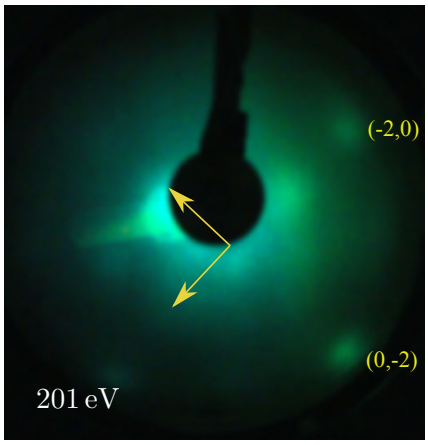

Figure 4.15.: LEED pattern of Fe/MgO(100) taken at 201 eV. The arrows represent the reciprocal unit vectors of the Fe(100) surface.

MgO(100) surface at room temperature. Based on the previous LEED results in Section 4.1.1 of Fe films grown on MgO(100) and annealed at higher temperature without O_2, we know that the cleanness of the MgO(100) surface plays an important role for the epitaxial growth of Fe on MgO(100). If the MgO is cleaved in air, the MgO(100) surfaces are contaminated and damaged [97]. Even after high-temperature annealing, the MgO is still contaminated by C. Only if the MgO(100) surface is annealed in O_2, contamination-free surfaces can be obtained [96]. Annealing in O_2 also improves the crystalline quality of epitaxial Fe films on MgO(100) [96].

Deposition Rh on Fe/MgO(100)

The next step is to evaporate $t_{\mathrm{Rh}} = 5.7\,\mathrm{nm}$ Rh on Fe/MgO(100) at room temperature. Rh is also evaporated at a low evaporation rate between 0.02 and 0.03 Å/s. With $t_{\mathrm{Fe}} = 5\,\mathrm{nm}$ and using Eq. (4.1), this should lead to a nominal atomic ratio of Fe to Rh of $X_{\mathrm{Fe}} : X_{\mathrm{Rh}} = 50.6\% : 49.4\%$.

An AES spectrum taken immediately after the Rh deposition is shown in Fig. 4.16. The reference peaks of Rh are at 259 and 305 eV [64], but we measure both peaks shifted by 5.5 eV at 264.5 and 310.5 eV, respectively, due to the charging of the sample. Note, that there are no other peaks visible in the spectrum, in particular there are no Fe peaks. This is consistent with the probing depth AES, if we assume that no Fe-Rh intermixing takes place at room temperature. In this stage, i.e. before annealing, no LEED spots are observable.

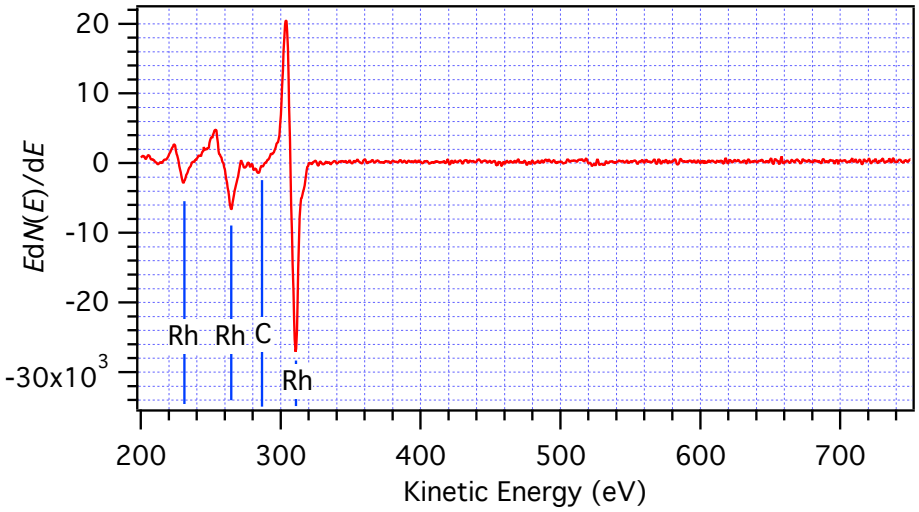

Figure 4.16.: AES spectrum of Rh grown on Fe/MgO(100) at room temperature before annealing.

Annealing

Next, the sample is annealed for two hours at 900 K to induce the intermixing of Fe and Rh and the formation of an ordered FeRh alloy film. We repeat the annealing cycle two times in order to check if the film composition has reached a stable state. The AES spectra taken after the first and the second annealing cycle are shown in Fig. 4.17 and the determined elemental contributions to the spectra taking into account the sensitivity factors are compiled in Table 4.2.

All Auger peak energies are higher than the reference values. The peak separations for a given element agree within 1 to 2 eV with the reference spectra as expected for charging. After the first annealing, we have $X_{\mathrm{Fe}} : X_{\mathrm{Rh}} = 49.8\% : 50.2\%$ and after the second annealing $X_{\mathrm{Fe}} : X_{\mathrm{Rh}} = 49.5\% : 50.5\%$. These two values agree within the estimated error with the intended nominal equiatomic composition. Thus, we

Table 4.2.: Spectral composition of an in-situ prepared intermixed FeRh film on MgO(100) after two subsequent annealing cycles.

Element	First Annealing		Second Annealing	
	E (eV)	X	E (eV)	X
Fe	607.7 662.0 714.7	49.8%	607.9 662.0 714.5	49.5 %
Rh	263.2 308.2	50.2 %	262.9 307.3	50.5 %

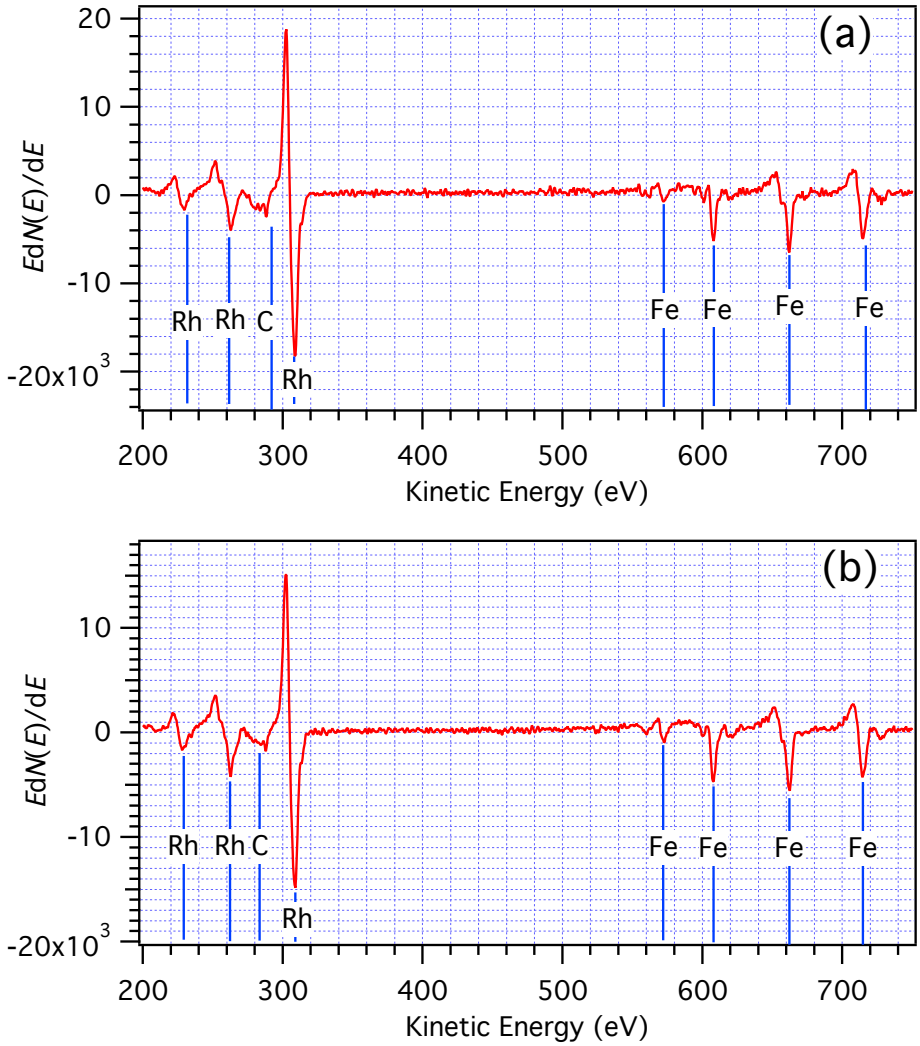

Figure 4.17.: Comparison of AES spectra taken of an in-situ prepared intermixed FeRh film on MgO(100) after (a) the first and (b) the second annealing cycle.

conclude that one annealing cycle at 900 K for two hours is sufficient to form the FeRh alloy and that this alloy is stable against further heating.

The LEED pattern taken after the second annealing is shown in Fig. 4.18 and reveals that the surface of the FeRh alloy film has a well-ordered surface. Thus, the separately deposited Fe and Rh bilayer film system undergoes a structural phase transition from disordered to ordered upon forming the FeRh alloy by high-temperature annealing. The lattice constant of FeRh, which is estimated from the LEED pattern at 266 eV and 359 eV, is 2.75 Å and 2.77 Å, respectively. However,

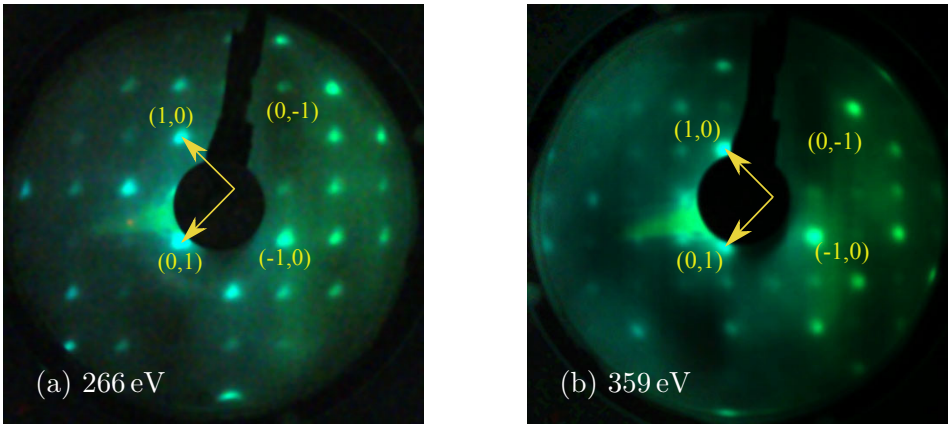

Figure 4.18.: LEED patterns of an in-situ prepared FeRh thin film on MgO(100) after high-temperature annealing taken at (a) 266 eV and (b) 359 eV. The arrows represent the reciprocal unit vectors of the FeRh(100) surface.

the lattice constant of bulk FeRh given by Zsoldos [87] is about 8% larger than the estimated results from the LEED pattern. If the lattice constant of the FeRh thin film is assumed to be the same in the bulk, we further estimate the potential due to charging to be -42.5 V and -57.3 V at 266 eV and 359 eV, respectively.

In summary, the result of the in-situ sample preparation is a single-crystalline, 10 nm thick FeRh alloy film with proper composition and a clean and ordered surface.

4.2.2. Magnetic properties of in-situ prepared FeRh films

In contrast to the ex-situ prepared sample discussed in Section 4.1.1, which required surface cleaning after air exposure for further measurements, the in-situ prepared sample can directly be measured by MOKE and SEMPA. Nevertheless, the whole measurement time is about three days during which the sample is kept at a pressure better than 3×10^{-10} mbar to reduce changes of the surface magnetic property due to residual gas contamination as much as possible.

MOKE results

In-situ MOKE experiments are performed immediately after the sample preparation to investigate the bulk magnetic property at room temperature as well as at low temperature. The Kerr angle versus external field measurements taken at at 293 and 143 K are shown in Fig. 4.19. At 293 K, we observe a magnetic hysteresis loop

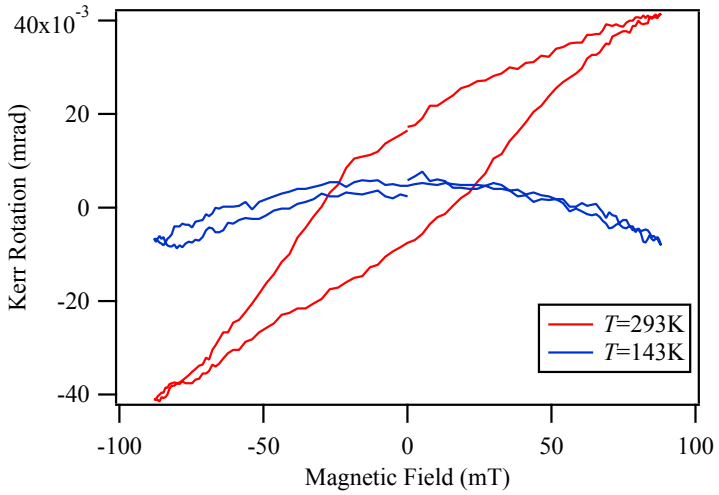

Figure 4.19.: MOKE of an in-situ prepared single-crystalline FeRh thin film on MgO(100) measured with the external field along the MgO[011] direction and at 293 K (red) and 143 K (blue), respectively. The MOKE results are taken as the average of three loops in oder to reduce the noise and the zero offset.

with a coercivity of 45.5 mT, but at 143 K there is no opening of the curve to form a hysteresis loop. These results indicate that the bulk of the alloy film is FM at 293 K but AFM at 143 K. Thus, there is a magnetic phase transition of the FeRh thin film with a transition temperature below room temperature.

Compared to the MOKE results of a 40 nm thick, ex-situ prepared FeRh film, which are shown in Fig. 4.8, the coercivity of 10 nm thick in-situ prepared film is much larger and the Kerr rotation is smaller. Actually, the 10 nm thick FeRh film is half-transparent for visible light. The laser light with a wavelength of 670 nm penetrates through the FeRh film and a fraction of the detected light is reflected at the interface between the FeRh and the MgO. Hence, the Kerr rotation is smaller. The larger coercivity is attributed to an increased influence of the surface and interface induced anisotropy energies, which both contribute to K_s in Eq. (4.2) (see Section 4.1.2).

SEMPA results

The temperature dependence of the domain structure of the surface of the in-situ prepared FeRh thin film is imaged by SEMPA in the temperature range from 122 to 450 K. First, the sample is cooled to 122 K, then heated to 450 K, cooled to 300 K in steps of 50 K, and finally heated again in steps of 50 K to 450 K. In order to reduce the effect of the polarization degradation of the SEMPA set-up due to

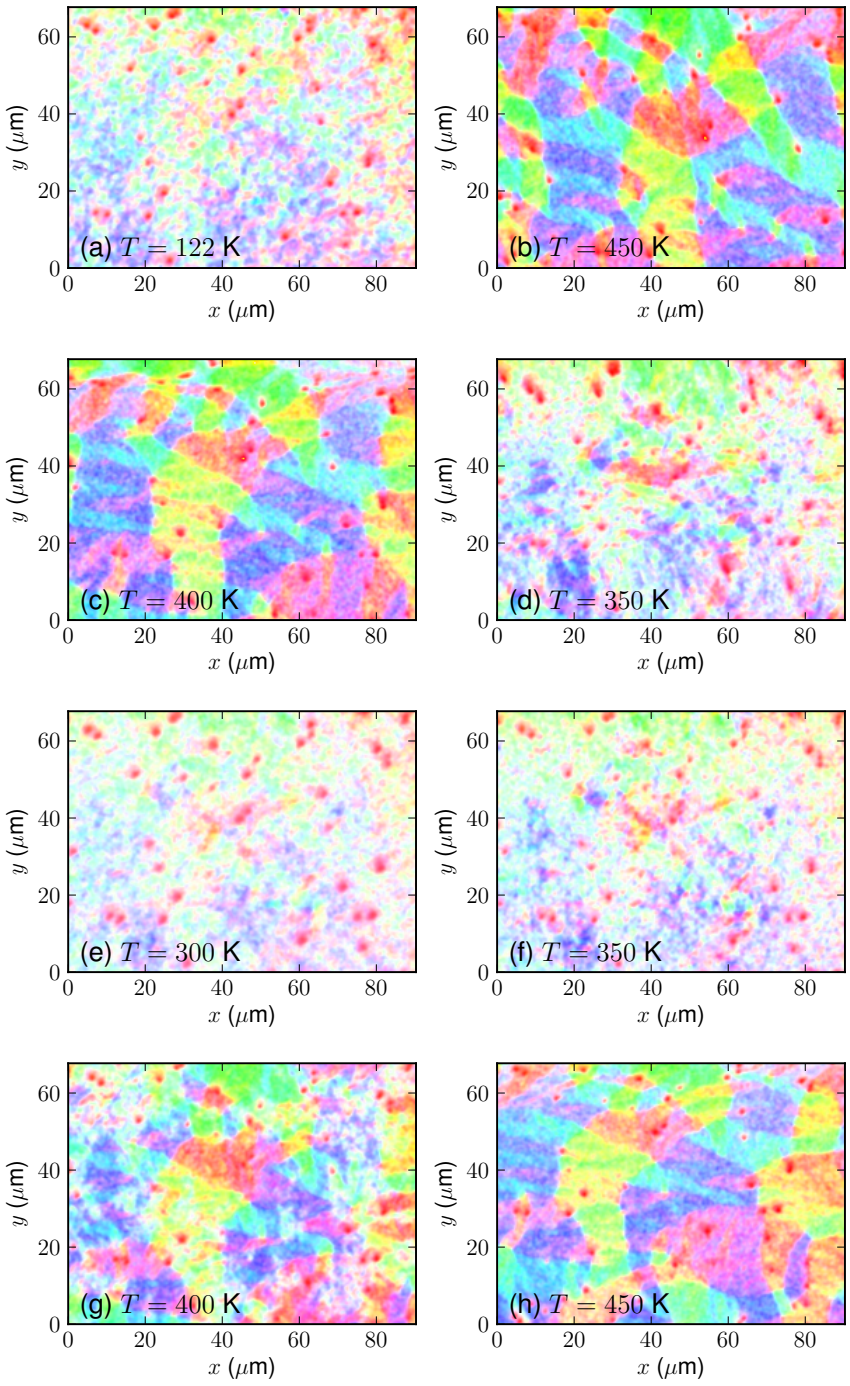

Figure 4.20.: SEMPA images of an in-situ prepared FeRh thin film measured at different temperatures as indicated. Images are taken at the same sample spot and in the sequence (a) to (h).

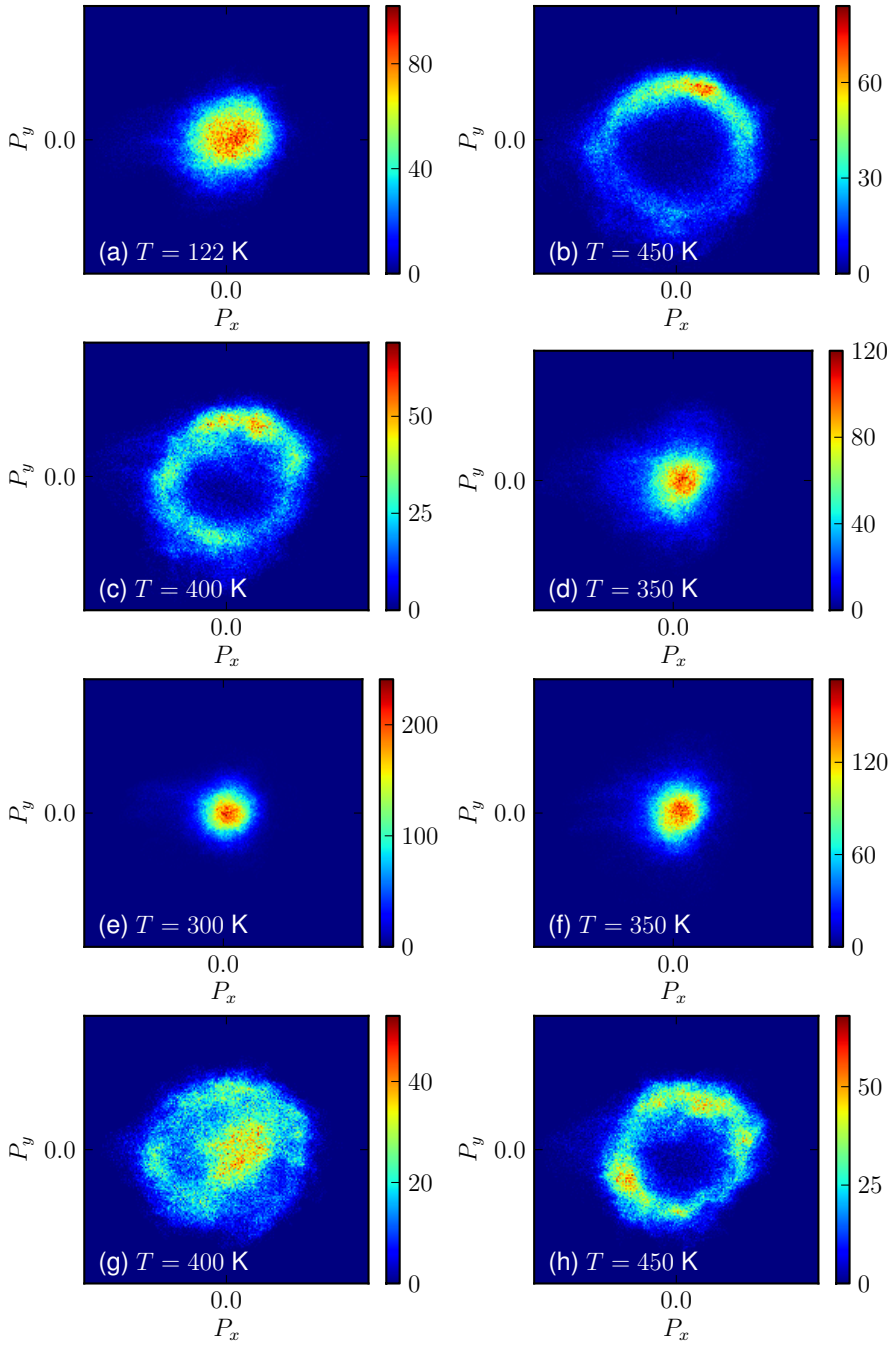

Figure 4.21.: Two-dimensional histograms of the SEMPA images shown in Fig. 4.20, which show the probability density as a function of the polarization vector for an in-situ prepared FeRh thin film.

contamination on the W(100) crystal, we apply a 1500 K flash to the crystal before each SEMPA measurement.

The SEMPA images are again presented in a false-color representation according to the color-wheel in Fig. 4.9, but here the polarization magnitudes are lower and cover the range ±0.07, whereas for the ex-situ prepared films the corresponding value was ±0.1.

At 450 K, the FeRh surface clearly shows a FM domain state. As the temperature decreases, both domain size and magnetization decrease. But even at 122 K, we can still observe magnetic domains. In contrast to Figs. 4.10(b) to (e), the domain walls move and new ones nucleate as the temperature decreases. Between 450 and 300 K, the domain size shrinks significantly, whereas below 300 K it stays almost constant. If the temperature is again increased from 300 to 450 K, the domains grow again and form a similar but not identical domain structure as before, compare Figs. 4.20(b) and (h). The drastic change in domain size and structure between 350 to 400 K shows clearly that the temperature can induce domain formation and nucleation in the surface region of an in-situ prepared FeRh thin film. This is different to what we have observed for the ex-situ prepared FeRh thin films and indicates that there are much less defects at the surface of the in-situ prepared FeRh film, which pin the domain walls. The energy barrier for domain formation and nucleation is lower for the in-situ prepared films. Hence, when the magnetic phase transition happens in the bulk of the film, the domains at the surface are affected in the sense that they can adjust to the new equilibrium state in the magnetic energy landscape, which depends on the temperature dependent magnetization and anisotropy.

Figure 4.21 shows the 2-dimensional histograms of Fig. 4.20, which reflect the strongly temperature dependent domain structure. The spin polarization magnitude abruptly shrinks when the temperature decreases from 400 to 350 K, see Fig. 4.21 (c) and (d). In the reverse direction, when the temperature increases from 350 to 400 K, the spin polarization magnitude increases again as evidenced by Figs. 4.21 (f) and (g).

Spin reorientation transition of the FeRh ultrathin film

The evolution of the surface spin polarization magnitude can be estimated from the radii of the circular contrasts of the magnetization density distributions in Fig. 4.21. The result is shown in Fig. 4.22. Between 400 to 350 K the spin polarization decreases from about 0.030 to 0.015 and then is stable at this level down to the lowest measurement temperature of 122 K. The data show with statistical significance that it does not decrease to zero. Actually, the spin polarization at 122 K is about half the value at 450 K. Therefore, it is obvious that the surface of the in-situ prepared FeRh thin film is FM in the whole temperature range from 122 to 450 K. There is no magnetic phase transition from AFM to FM at the surface. On the other hand,

the MOKE results show that there is such a transition in the bulk with a transition temperature below room temperature, but inside the temperature range covered by the SEMPA measurements. This means that at 122 K, both the AFM state in the bulk and the FM state at the surface coexist in in-situ prepared FeRh thin films.

Similar to the ex-situ prepared films, the reduced transition temperature of the in-situ prepared FeRh thin film's bulk can be attributed to the strain induced by the FeRh/MgO(100) interface (see Section 4.1.2). But the surface magnetic properties of in-situ and ex-situ prepared FeRh films as observed by SEMPA behave differently, though both samples' surfaces are FM in the whole investigated temperature range. The main difference is that the surface spin polarization of the 10 nm thick in-situ prepared FeRh film increases (decreases) abruptly from 1.5% to 3% when the temperature increases (decreases) from 350 to 400 K (400 to 350 K) as seen in Fig. 4.22, while the spin polarization of 40 nm thick ex-situ prepared FeRh films decreases continuously as the temperature increases (see Fig. 4.12).

Because the sample plane is perpendicular to the axis of the SPLEED detector, only the two in-plane magnetization components of the surface magnetization are detected in SEMPA measurements. The step-like behavior of the spin polarization in Fig. 4.22, which more precisely indicates an increase/decrease of the **in-plane** magnetization, is believed to be the result of a spin reorientation transition at the surface from out-of-plane below 350 K to in-plane above 400 K. Previous MOKE results of Cao et al. [24] have already indicated that there is temperature dependent, stress-induced anisotropy with out-of-plane easy axis in a 150 nm thick single-crystalline FeRh film. The induced magnetic anisotropy is in this paper estimated to be as high as 1×10^6 J/m^3 at the temperature, where the first-order transition occurs. The stress-induced anisotropy originates from a volume expansion due to

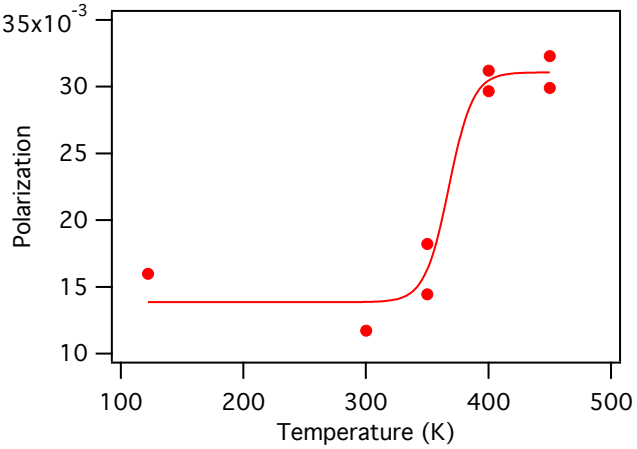

Figure 4.22.: Temperature dependent spin polarization of an in-situ prepared FeRh on MgO(100).

(i) the much larger linear thermal expansion coefficient of FeRh compared to MgO, especially when FeRh undergoes the first-order transition [31], (ii) the large volume magnetostriction, which can be as high as 4×10^{-4} [98], and (iii) the large stress existing in single-crystalline FeRh films epitaxially grown on MgO(100). The DFT calculation results by Bordel et al. [25] also reveal that the Fe moment can undergo a spin reorientation transition from out-of-plane to in-plane depending on the strain. If the out-of-plane lattice constant is c and the in-plane lattice constant is a, then for $c/a < 1$ the Fe magnetic moments are aligned in-plane and for $c/a > 1$ out-of-plane. This stress-induced spin reorientation transition has been experimentally confirmed by Bordel et al. using ^{57}Fe conversion electron Mössbauer spectroscopy of a 150 nm thick single-crystalline FeRh film on MgO(100).

Both Cao et al. and Bordel et al. point out that the spin reorientation transition of FeRh occurs when FeRh undergoes the first-order transition. But in the present case dealing with very thin FeRh films, the spin reorientation transition of the film's surface occurs above the observed transition temperature, which according to the MOKE results is below room temperature, while the SEMPA reveal a spin reorientation transition temperature between 350 to 400 K. As both Cao et al. and Bordel et al. employ 150 nm thick films, the observation of the spin reorientation transition at another temperature than the AFM to FM transition is most likely related to the much lower film thickness in our case. Our data then indicate that the AFM to FM transition is more sensitive to the stress induced by the FeRh/MgO interface than the spin reorientation transition.

In this chapter, single-crystalline FeRh thin films on MgO(100) are prepared both ex-situ and in-situ without capping layer by separate layer deposition. Comparing the measurement results of both ex-situ and in-situ samples, we conclude the following:

1. MOKE results of both ex-situ and in-situ prepared single-crystalline FeRh thin films on MgO(100) show that there is a magnetic phase transition from AFM to FM for Rh-rich and nominal equiatomic samples, but not for the Fe-rich sample, in agreement with the phase diagram of bulk FeRh alloy reported by Shirane et al. [29] and Hofer et al. [32] (see Fig. 2.2 and Fig. 2.3 in Section 2.1). However, the magnetic phase transition temperatures of the Rh-rich and nominal equiatomic samples are below room temperature. This is lower than the first-order phase transition temperature ranges reported in literature for the equiatomic bulk FeRh alloy (310 to 400 K) [91, 32, 36, 92] and sputtered FeRh thin films (320 to 410 K) [88]. As indicated by Maat et al. [43], the decrease of the magnetic transition temperature of single-crystalline thin films can be due to the strain. We conclude that the separate layer deposition method leads to epitaxial FeRh thin films, which exhibit larger strain compared to sputtered FeRh thin films and bulk FeRh samples. Hence, we may also assume that the AFM Fe-Fe interaction entering the Ising model is reduced by the larger strain (see Fig. 2.12 in Section 2.2.2) and in this manner

gives rise to the reduced transition temperature.

2. SEMPA results reveal that Rh-rich and nominal equiatomic FeRh thin films without any capping layers exhibit the coexistence of the AFM in the bulk and the FM state at the surface at low temperature, which has previously been observed only for FeRh thin films with thin capping layers [22, 99, 23]. The suppression of the first-order magnetic phase transition at the surface of FeRh thin films is thus an intrinsic magnetic property rather than an artifact induced by capping layers. As indicated by the Ising model of FeRh, if the AFM Fe-Fe interaction is only slightly reduced, the first-order magnetic transition temperature is dramatically reduced or even drops to zero (see Fig. 2.12 in Section 2.2.2). Hence, a possible explanation for the absence of magnetic phase transition at the surface is that the AFM Fe-Fe interaction at the surface is lower than in the bulk, e.g. due to symmetry breaking at the surface. Thus, the surface layer intrinsically show a much lower transition temperature or even behaves as a normal ferromagnetic layer.

3. While there is a spin reorientation transition in in-situ prepared 10 nm thick equiatomic FeRh, which gives rise to domain nucleation and formation driven by temperature, the domain structure of ex-situ prepared 40 nm thick Rh-rich FeRh films does not change with temperature. Only the spin polarization decreases as the temperature increase as expected for a FM. The temperature driven nucleation of surface magnetic domains in FeRh thin films with thin capping layers has previously been reported by Baldasseroni et al. [23]. In contrast to the work of Baldasseroni et al. the domains of ex-situ prepared Rh-rich FeRh thin films are probably pinned by surface contamination and defects. Therefore, no temperature-driven domain nucleation and formation can be observed by SEMPA. The in-situ prepared FeRh films, however, exhibit domain nucleation and formation similar to the work of Baldasseroni et al.

4. A step-like behavior of the temperature dependent spin polarization is observable in 10 nm thick FeRh films, which based on literature reports is attributed to a spin reorientation transition at the surface from out-of-plane to in-plane [24, 25]. The in-situ prepared sample is much thinner (10 nm) than the ex-situ prepared samples (40 nm) and the samples of Baldasseroni et al. (90 nm), which is likely to give rise to larger strain [25]. Therefore, the observed spin orientation transition at the surface of FeRh thin films is believed to be the result of strongly temperature dependent strain-induced anisotropy.

5. Summary and conclusion

In this thesis, the temperature-induced metamagnetic transition and the associated temperature dependent domain structure of single-crystalline FeRh thin films on MgO(100) without any capping layer have been studied.

First, an Ising model of FeRh is discussed, for which an approximate solution is obtained by mean field theory. The numerical results show that the metamagnetic transition, which is a first-order phase transition from FM to AFM, can be absent if the AFM Fe-Fe interaction is slightly reduced from the bulk value of FeRh. According to DFT calculations, the AFM Fe-Fe interaction can be reduced by a volume change[34]. Hence, strain induced by thermal expansion can also reduce the Fe-Fe interaction leading to a reduced transition temperature or even the suppression of the metamagnetic phase transition.

Previous studies have revealed that both AFM and FM states can coexist in single-crystalline FeRh thin films on MgO(100) with capping layer (e.g. Pt, MgO, Al, or Au) [43, 22, 95]. Baldasseroni et al. [23] studied the surface magnetic domain structure of ex-situ prepared 90 nm thick equiatomic FeRh thin films by PEEM. They reported that when the bulk is in the AFM state, they still could observe FM domains at the capped surface. This was not the case for uncapped films because they were oxidized after the transfer between two UHV systems with air exposure. Thus, these surfaces have become nonmagnetic.

The question whether the coexistence of the FM surface with the AFM bulk is an artifact of the capping layer or an intrinsic property of FeRh films on MgO(100) motivated this thesis. Two kinds of sample preparation procedures are performed to obtain FeRh films without capping layer. The first is called ex-situ preparation and involves two UHV systems as in the study of Baldasseroni et al. [23], but here we aim at removing the contamination and oxide layer after the transfer through ambient air by applying high-temperature annealing prior to the magnetic surface characterization. During the course of this thesis the UHV system housing the MOKE and SEMPA setups was extended to provide suitable facilities for the in-situ deposition of Fe and Rh films allowing for the second, so-called in-situ preparation procedure.

Using the ex-situ sample preparation, two 40 nm single-crystalline FeRh thin films on MgO(100) have been prepared by separate layer deposition of Fe and Rh at 600 K followed by high temperature annealing to induced the formation of the ordered FeRh alloy. Both samples show a cubic LEED patterns after annealing. The XPS

results reveal that one sample is Rh-rich and the other one Fe-rich. After air exposure during transfer between the UHV systems for deposition and characterization, the contamination of the samples is analyzed by AES. The Rh-rich FeRh surface was only contaminated by physisorbed C and O species. After high-temperature annealing, the O contamination was completely removed and the C contamination was strongly reduced. In contrast, the Fe-rich surface is oxidized after air exposure, and only the C contamination can be removed by high-temperature annealing. The in-situ MOKE results indicated that the Rh-rich FeRh thin film shows the magnetic phase transition from AFM to FM below room temperature, while there is no such transition in the Fe-rich FeRh thin film. Furthermore, though no FM domains can be observed by SEMPA in the Fe-rich surface due to oxidation, FM domains are clearly imaged for the Rh-rich film when the bulk is in both the FM as well as in the AFM state. These SEMPA results reveal the coexistence of the AFM and FM state in uncapped, weakly contaminated Rh-rich FeRh thin films below the magnetic phase transition temperature, i.e. the magnetic phase transition from AFM to FM is suppressed at the surface.

While these results are a first indication that the coexistence of the FM and AFM phases is not only due to capping layers, the weak C contamination and the deviation from the equiatomic alloy towards an Rh-rich alloy demand for a more controlled in-situ preparation procedure. After installing and testing an additional e-gun evaporator in the NSCT a entirely in-situ preparation without vacuum break became possible. A 10 nm thick single-crystalline FeRh film on MgO(100) was prepared in the NSCT again by separate layer deposition of Fe and Rh at room temperature followed high-temperature annealing. After the high-temperature annealing, AES show that the separate layers of Fe and Rh intermixed to a nearly equiatomic FeRh alloy, and cubic LEED patterns indicate that the surface is well ordered. The MOKE results show the magnetic phase transition from AFM to FM below room temperature, whereas SEMPA images indicate that the surface is in the FM state above and below the bulk transition temperature. Although the magnetic phase transition is absent in the surface, there is a spin reorientation transition from out-of-plane to in-plane above room temperature, which is believed to originate from strong strain-induced out-of-plane anisotropy.

Considering the ex-situ and in-situ prepared samples, we find that (i) the magnetic phase transition temperature of films prepared by separate layer deposition is lower than for the bulk FeRh alloy [91, 32, 36, 92] or sputtered FeRh thin films [88, 23] and (ii) there is a spin reorientation transition from out-of-plane to in-plane in the 10 nm thick FeRh film but not for the 40 nm thick films. The lower transition temperature may be due to different strain in our films compared to bulk material or sputtered films, which reduces the Fe-Fe interaction. According to the Ising model of FeRh this leads to a lower transition temperature. Similarly, the spin reorientation transition in the thinner FeRh films is believed to be due to strong out-of-plane anisotropy induced by strain originating from the FeRh/MgO interface.

In summary, we could extend the study of Baldasseroni et al. [23], in which FM domains could only be observed at the surface of equiatomic FeRh thin films with capping layer, but not for uncapped surfaces due to oxidation. Here, we have observed FM domains at the surface of (i) an uncapped, weakly C-contaminated, and Rh-rich FeRh film and (ii) a clean and equiatomic FeRh thin film by SEMPA in a temperature range from far below to well above the bulk transition temperature. We conclude that the suppression of the magnetic phase transition from AFM to FM at the surface and the associated coexistence of the FM phase at the surface and the AFM phase in the bulk are an intrinsic magnetic property of single-crystalline FeRh thin films on MgO(100).

The absence of first-order magnetic phase transition at the surface of FeRh films can be harmful for the application to heat-assisted magnetic recording, because the FM surface can reduce the coercivity of the bi-layer system at room temperature via the exchange spring mechanism [18]. This would result in an detrimental lower thermal stability of the data [9].

Though we could observe the FM domains in the single-crystalline FeRh thin film surface when the bulk is in AFM state, the origination of the absence of the magnetic phase transition is still unclear. Hence, future research needs to address this question. In addition, the results of this thesis show that the surface magnetic properties strongly depend on the film thickness. One likely explanation is that the lattice mismatch between FeRh and MgO(100) induces strain that relaxes with increasing film thickness. Here, thickness dependent magnetic domain imaging combined with lattice constant measurements could shed light on the origin of the thickness dependent surface magnetic property.

A. Mean field approximation of Ising model

The Ising model is a simple model of a many-body system that can be solved analytically on one- and two-dimensional lattices. The solutions show a phase transition for two-dimensional lattice but not for the one-dimensional. The Ising model can be widely applied to many problems of statistical physics including the paramagnetic to ferromagnetic phase transition.

The basic assumption of the Ising model is that the spins in a d-dimensional lattice only can take the values +1 or -1 and only nearby spins interact with each other. The Hamiltonian of the Ising model can be expressed as[37]

$$H = -\sum_{<i,j>}^{N} J_{ij} S_i S_j - \mu h \sum_i S_i, \tag{A.1}$$

where J_{ij} are the exchange constants, S_i is the ith spin, and h is the external magnetic field. The symbol $< i, j >$ indicates that the summation is over all pairs of neighbouring spins, N is the total number of the spins of the Ising system.

If an energy E_τ corresponds to a configuration τ, which is defined by the set of values $(S_1, S_2, ..., S_N)$, then the total free energy of the Ising system can be expressed as

$$F(T) = -k_B T \ln Z(T) = -k_B T \ln \sum_\tau \exp\left(-\frac{E_\tau}{k_B T}\right), \tag{A.2}$$

where $Z(T)$ is the partition, T is the temperature, and k_B is the Boltzmann constant. The sum runs over the total number of the possible configurations, which is 2^N. Hence, the exact solution of the partition is very difficult, but exact solutions for the one and two-dimensional Ising model are possible. Unfortunately, the exact solution of three-dimensional model has not yet been found, and one has to resort to the mean-field approximation to solve Ising model in higher ($d \geq 3$) dimensions.

One approach to solve the Ising model in the framework of the mean field theory is the Bragg-Williams approximation [100]. First, the free energy in terms of the order parameter is constructed. Then the system free energy is minimized with respect to the order parameter in order to obtain its equilibrium value. Here, only the Ising systems without external magnetic field will be considered.

Consider an ferromagnetic coupling ($J > 0$) Ising system with the total number of spin N. The order parameter is m, which is also the average (dimensionless) magnetization. If the spin-up number is N_+ and spin-down number N_-, then

$$N_+ = \frac{N}{2}(1+m) \tag{A.3a}$$

$$N_- = \frac{N}{2}(1-m). \tag{A.3b}$$

If the individual spins are statistically independent, the entropy can be expressed as

$$S = -k_B N \left(\frac{N_+}{N} \ln \frac{N_+}{N} + \frac{N_-}{N} \ln \frac{N_-}{N} \right). \tag{A.4}$$

The Hamiltonian of the Ising system is approximated by

$$H = -\frac{zJN}{2} m^2, \tag{A.5}$$

where z is the number of nearest neighbors and J is the isotropic exhange constant ($J = J_{i,j}$ for all pairs $< i, j >$). $h_{eff} = zJNm/2$ is the mean field. As a result, the free energy can be calculated as

$$F(m,T) = -\frac{zJN}{2} m^2 + k_B T N \left(\frac{1+m}{2} \ln \frac{1+m}{2} + \frac{1-m}{2} \ln \frac{1-m}{2} \right) \tag{A.6}$$

Figure A.1 shows the averaged free energy $g(m,T) = F(m,T)/zJN$ as a function of the order parameter (magnetization) m and the reduced temperature T/T_c, where $T_c = zJ/k_B$ is the critical temperature.

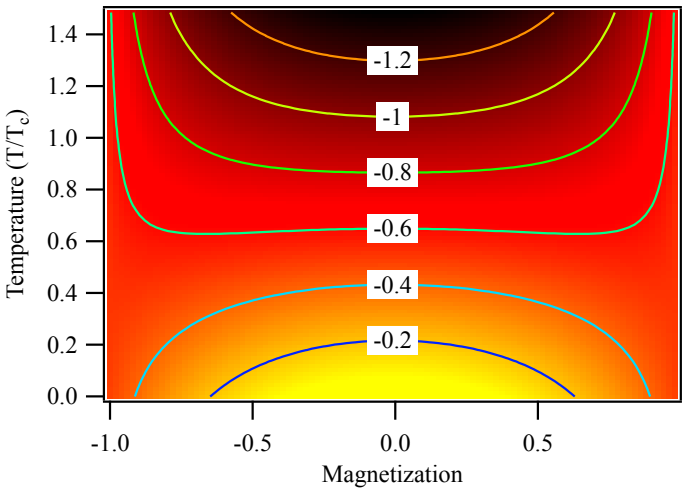

Figure A.1.: Averaged free energy $g(m,T)$ of the Ising system.

The condition to minimize the free energy with respect to the order parameter m is

$$\frac{\partial F(m,T)}{\partial m} = -zJNm + \frac{N}{2}k_BT\ln\frac{1+m}{1-m} = 0, \tag{A.7}$$

which results in

$$m = \tanh(\frac{T_c}{T}m) \quad \text{with} \quad T_c = \frac{zJ}{k_B}. \tag{A.8}$$

When $J > 0$, there is critical temperature T_c, which is called Curie temperature. For $T > T_c$, zero is the only solution of Eq. (A.8). But for $0 < T < T_c$, there are two nonzero solutions, which correspond to ferromagnetic order. The nonzero solutions can be obtained iteratively from Eq. (A.8) by staring with an initial guess, e.g. $m = 0.5$. The result is shown in Fig. A.2. When $T = 0$, $m = \pm 1$, which means all the spins align in the same direction at absolute zero temperature. As the temperature increases, the magnetization decreases. Above the Curie temperature, the magnetization is zero as the system has become fully disordered. Although zero is always a solution when $T \geqslant 0$, zero is an unstable solution when $T < T_c$, because $m = 0$ does not minimize $F(m, T < T_c)$.

Another approach to solve the Ising model within the mean field theory is the variational density matrix method. If the "trial Hamiltonian" is $\hat{H}$, and the corresponding density matrix is $\hat{\rho}$, then the inequality for the free energy is expressed as [101]

$$F \leqslant \mathrm{Tr}\hat{\rho}\hat{H}_0 + k_BT\mathrm{Tr}\hat{\rho}\ln\hat{\rho}, \tag{A.9}$$

where ρ_0 is an approximation of the density matrix of the system fulfilling the normalization condition $\mathrm{Tr}\rho_0 = 1$. Under the mean field approximation, the fluctuating field due to the nearest neighbor interactions acting on a given spin is approximated by its mean value

$$h_{\text{eff}} = zJm. \tag{A.10}$$

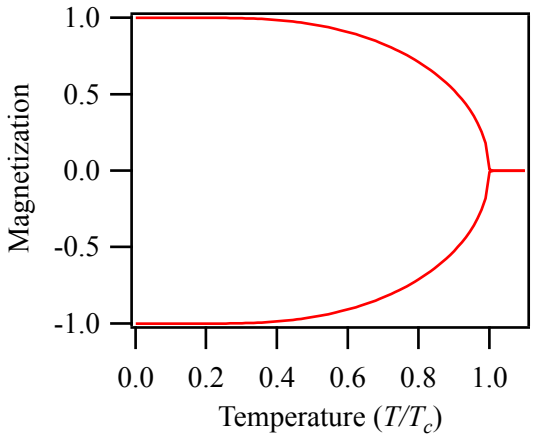

Figure A.2.: Solution of Ising model based on the mean field approximation.

Then the single spin Hamiltonian without external magnetic field can be written as

$$\hat{H}_{i,\mathrm{MF}} = -h_{\mathrm{eff}} S_i \quad ; \quad i = 1 \ldots N, \tag{A.11}$$

where S_i can be expressed as a diagonal matrix as

$$S_i = \begin{pmatrix} 1 & 0 \\ 0 & -1 \end{pmatrix}, \tag{A.12}$$

i.e. $\hat{H}_{i,\mathrm{MF}}$ is diagonal. And the corresponding single spin density matrix can be given by Gibbs districution

$$\hat{\rho}_{i,\mathrm{MF}} = \frac{\exp\left[-\hat{H}_{i,\mathrm{MF}}/(k_B T)\right]}{\mathrm{Tr}\hat{H}_{i,\mathrm{MF}}}, \tag{A.13}$$

i.e. $\hat{\rho}_{i,\mathrm{MF}}$ is also a diagonal matrix.

Then, the trial Hamiltonian can be obtained as

$$\hat{H} = \sum_i \hat{H}_{i,\mathrm{MF}}, \tag{A.14}$$

and the corresponding trial density matrix can also be obtained as

$$\hat{\rho} = \sum_i \hat{\rho}_{i,\mathrm{MF}}, \tag{A.15}$$

The interacting system becomes a non-interacting system under the molecular field approximation. If Eq. (A.14) and Eq. (A.15) is substituted into Eq. (A.9), we could obtain the approximated free energy of the Ising system, which yields the same result as Eq. A.6.

Furthermore, the mean value of m needs to fulfill the self-consistency condition

$$m = \frac{\mathrm{Tr}\{\hat{S}_0 \exp[-H(\hat{S}_0)/(k_B T)]\}}{\mathrm{Tr}\{\exp[-H(\hat{S}_0)/(k_B T)]\}}, \tag{A.16}$$

Substituting Eq. (A.11), Eq. (A.12) and Eq. (A.13) into Eq. (A.16) yields the same result as Eq. (A.8).

Compared to the Bragg-Williams approximation, the variational density matrix method is much more straightforward.

B. Spin-1 Ising model with zero-field splitting

If the external magnetic field is absent, the Hamiltonian of the Spin-1 Ising model with zero field splitting can be expressed as

$$H = D\sum_{i} S_{zi}^2 - J\sum_{<i,j>} S_{zi}S_{zj}, \tag{B.1}$$

where D is zero-field splitting, J is the exchange constant, μ is the magnetic moment, and the spin values $S_z \in (0, \pm 1)$. Each triplet is split into a singlet and a doublet by the zero-field splitting parameter D. Depending the value of D which is due to the crystal filed interaction, the singlet energy level can be lower or higher than the doublet levels, or even between the doublet levels, see Fig. B.1. For $D = 0$, the Spin-1 Ising model with zero field splitting degrades to a standard spin-$\frac{1}{2}$ Ising model. If $|D|$ is not so large, the singlet lies between the doublet energy levels. If $D \gg 0$, the doublet energy level is much higher than the singlet, the ground state will be nonmagnetic. However, if $D \ll 0$, the singlet will not have any effect to the Ising system.

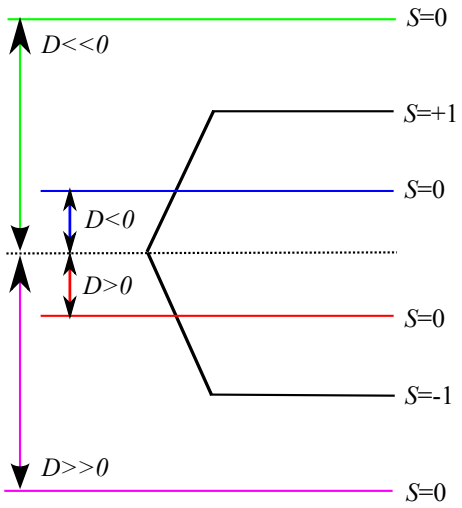

Figure B.1.: Energy-level diagram of the spin-1 Ising model with zero field splitting.

In such an Ising system consisting of N triplet spins with zero field splitting, each site has 3 possible spin configurations $S_z = 0$, $S_z = 1$, or $S_z = -1$. In total, there are 3^N configurations. The exact expression of the partition function is very difficult, even for two-dimensional cubic lattice. One need to resort to the mean field theory to obtain the approximation solution using variational density method (see Appendix A).

For a particular spin S_0 in the spin-1 Ising system which can be expressed as a diagonal matrix

$$S_0 = \begin{pmatrix} 1 & 0 & 0 \\ 0 & 0 & 0 \\ 0 & 0 & -1 \end{pmatrix}. \tag{B.2}$$

if the mean field theory is employed, the single spin Hamiltonian of spin-1 Ising model with zero filed splitting is

$$H_{\mathrm{MF}} = DS_0^2 - h_{\mathrm{eff}} S_0, \tag{B.3}$$

where $h_{\mathrm{eff}} = zJm$, and z is the number of the nearest spins while m is the magnetization. Substituting Eq. (B.2) in Eq. (B.3), we could obtain the expression of H_{MF} as

$$H_{\mathrm{MF}} = \begin{pmatrix} D - h_{\mathrm{eff}} & 0 & 0 \\ 0 & 0 & 0 \\ 0 & 0 & D + h_{\mathrm{eff}} \end{pmatrix}. \tag{B.4}$$

The corresponding density matrix can be given by Gibbs distribution

$$\rho_{\mathrm{MF}} = \frac{\exp\left[-H_{\mathrm{MF}}/(k_B T)\right]}{Z_{\mathrm{MF}}}, \tag{B.5}$$

where Z_{MF} is the single spin partition function, k_B is the Boltzmann constant, T is the temperature. Under the mean field approximation, all the spins are assumed to be independent, then the $\hat{H}$ can be obtained by

$$\hat{H} = \sum_i H_{i,\mathrm{MF}}, \tag{B.6}$$

and $\hat{\rho}$ can also obtained by

$$\rho = \prod_i \rho_{i,\mathrm{MF}}. \tag{B.7}$$

Since the magnetization is the mean value of spins, then m can be calculated as

$$m = \mathrm{Tr}\{S_0 \rho_{\mathrm{MF}}\}. \tag{B.8}$$

Ferromagnetic Spin-1 Ising model with zero-field splitting

At first, ferromagnetic coupling is considered, where $J > 0$. Using the mean field approximation, the single spin partition function can be expressed as

$$\begin{aligned} Z_{\mathrm{MF}} &= \mathrm{Tr} \exp\left(-\frac{H_{\mathrm{MF}}}{k_B T}\right) \\ &= 1 + \exp\left(-\frac{D}{k_B T}\right)\left[\exp\left(\frac{zJm}{k_B T}\right) + \exp\left(-\frac{zJm}{k_B T}\right)\right]. \end{aligned} \tag{B.9}$$

Substituting eq. (B.4) and eq. (B.9) in eq. (B.5), the density matrix of single spin under the mean field approximation can be obtained as

$$\rho_{\mathrm{MF}} = \frac{1}{1 + \exp\left(-\frac{D}{k_B T}\right)\left[\exp\left(\frac{zJm}{k_B T}\right) + \exp\left(-\frac{zJm}{k_B T}\right)\right]} \begin{pmatrix} D - h_{\mathrm{eff}} & 0 & 0 \\ 0 & 0 & 0 \\ 0 & 0 & D + h_{\mathrm{eff}} \end{pmatrix}. \tag{B.10}$$

The average energy per spin given by Blume et al. [102] can be described as

$$\Phi = F/N = D\mathrm{Tr}\rho_{\mathrm{MF}} S_0^2 - \frac{1}{2} zJ(\mathrm{Tr}\rho_{\mathrm{MF}} S_0)^2 + k_B T \mathrm{Tr}\rho_{\mathrm{MF}} \ln \rho_{\mathrm{MF}}, \tag{B.11}$$

where the factor $\frac{1}{2}$ in front of the zJ is used to avoid the double counting of the exchange interaction.
Then substituting Eq. (B.10) into Eq. (B.11), we obtain

$$\Phi = -k_B T \ln\left\{1 + \exp\left(-\frac{D}{k_B T}\right)\left[\exp\left(\frac{zJm}{k_B T}\right) + \exp\left(-\frac{zJm}{k_B T}\right)\right]\right\} + \frac{1}{2} zJm^2. \tag{B.12}$$

Furthermore, substituting Eq. (B.10) into Eq. (B.8), the magnetization can be calculated as

$$m = \frac{\exp[zJm/(k_B T)] - \exp[-zJm/(k_B T)]}{\exp[D/(k_B T)] + \exp[zJm/(k_B T)] + \exp[-zJm/(k_B T)]}. \tag{B.13}$$

If we define $T_0 = zJ/k_B > 0$ and $\delta = D/(zJ)$, then we can rewrite Eq. (B.13) as

$$m = \frac{\sinh(\frac{T_0}{T} m)}{\frac{1}{2}\exp(\frac{T_0}{T}\delta) + \cosh(\frac{T_0}{T} m)}. \tag{B.14}$$

Depending on the value of δ, the system can have different phase transitions. Firstly, consider three extreme cases:

1. For $\delta \to \infty$, $m \to 0$ at all temperature. The system is disordered and does not have phase transition.
2. For $\delta \to -\infty$, $m \to \tanh(T_0 m/T)$. The system degenerates to a Spin-$\frac{1}{2}$ Ising system, which has already been discussed in the previous section.

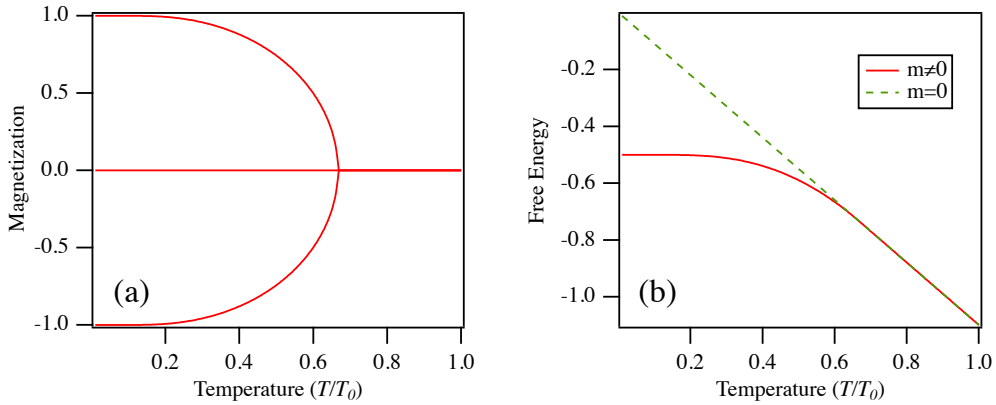

Figure B.2.: Numerical solution of the spin-1 Ising model. Temperature dependence of (a) the magnetization m and (b) then free energy.

3. For $\delta = 0$, the splitting field is absent and the system degenerates to a spin-1 Ising system. The magnetization of spin-1 Ising model is shown in Fig. B.2 (a), which is obtained by solving Eq. (B.14) numerically with $\delta = 0$. Figure B.2 (a) indicates that there is a critical temperature $T_c = 0.6670T_0$. When $T > T_c$, the only solution is $M = 0$. But for $T < T_c$, there are two non-zero solutions with opposite sign in addition to the zero solution. Actually, the zero solution is a meta-stable solution, because the free energy is higher than for the non-zero solutions as shown in Fig. B.2 (b). This means that the system has magnetic order at low temperature and becomes disordered at high temperature. The spin-1 Ising system also shows a second-order phase transition from ferromagnetic order to paramagnetism.

Now we consider the ground state of Eq. (B.14) when $T \to 0^+$. Because Eq. (B.14)is a even function, we just discuss the case when $m \geqslant 0$. For $T \to 0^+$, if we want to have a nonzero solution, the right side of Eq. (B.14) must satisfy the following condition

$$\lim_{T\to 0^+} \frac{\sinh(\frac{T_0}{T}m)}{\frac{1}{2}\exp(\frac{T_0}{T}\delta) + \cosh(\frac{T_0}{T}m)} = \lim_{T\to 0^+} \frac{1}{\exp\left[\frac{T_0}{T}(\delta - m)\right] + 1} > 0. \tag{B.15}$$

Thus we have

$$\delta - m \leqslant 0. \tag{B.16}$$

Besides, for $\delta < m = 1$, we have

$$m = \lim_{T\to 0^+} \frac{\sinh(\frac{T_0}{T}m)}{\frac{1}{2}\exp(\frac{T_0}{T}\delta) + \cosh(\frac{T_0}{T}m)} = 1. \tag{B.17}$$

It clear that, for $\delta < 1$, $m = 1$ is always the ground state. However, when $\delta < 1$, Eq. (B.14) has a singular point $m = \delta < 1$, which corresponds to a unstable state.

For $\delta \leqslant 0$, three are nonzero solutions of the magnetization besides the zero solution. But the stable solutions need to minimize the free energy. Therfore, we now consider the free energy at the ground state. In order to simplify the expression of the free energy, we define the dimensionless parameters $\Phi(m) = G/(NzJ)$ and $T' = T/T_0$ and recall Eq. (B.12), then we can obtain an expression for $\Phi(m)$ as

$$\Phi(m) = -T' \ln \left[1 + 2 \exp\left(-\frac{\delta}{T'} \right) \cosh\left(\frac{m}{T'} \right) \right] + \frac{1}{2} m^2. \tag{B.18}$$

In ground state, Eq. (B.18) has different solutions depending on m and δ when $T' \to 0^+$. Here we only consider the cases with $m > 0$:

1. For $m = 0$, we directly have
$$\Phi(0) = 0. \tag{B.19}$$

2. For $m \neq 0$ and $\delta > m$, we have
$$\lim_{T' \to 0} \Phi(m) = \frac{1}{2} m^2 > \Phi(0). \tag{B.20}$$
Obviously, $m = 0$ is the only stable solution when $\delta > 1$.

3. For $m \neq 0$ and $\delta = m$, we also have
$$\lim_{T' \to 0} \Phi(m) = \frac{1}{2} m^2 > \Phi(0). \tag{B.21}$$
In this case, $\delta = m = 1/2$ is an unstable solution. The only stable solution is also $m = 0$.

4. For $m \neq 0$ and $\delta < m$, we have
$$\lim_{T' \to 0} \Phi(m) = \delta - m + \frac{1}{2} m^2. \tag{B.22}$$
For $\delta < m$, the nonzero solution for the magnetization is $m = 1$. Hence, it is clear that for $1/2 < \delta < 1$, the only stable solution is $m = 0$. And for $\delta < 1/2$, $m = 1$ is the stable solution. Furthermore, when $\delta = 1/2$, both $m = 1$ and $m = 0$ are metastable solutions.

From the above discussion, we conclude that there is no phase transition of the spin-1 Ising model with zero field splitting for $D > zJ/2$, because there is only one stable solution of the system at all the temperatures. But for $D < zJ/2$, a phase transition may occur in the system because there are nonzero solutions. Fig B.3 shows the contour plots of the free energy as a function of temperature and the magnetization with zero-field splitting parameters $D = 0.45zJ$ and $D = 0.47zJ$ near the critical temperature. The black lines are the magnetization as a function of temperature, which is obtained by numerical minimization the free energy function. Fig B.3 (a) shows that the free energy for $m > 0$ is always lower than the free energy

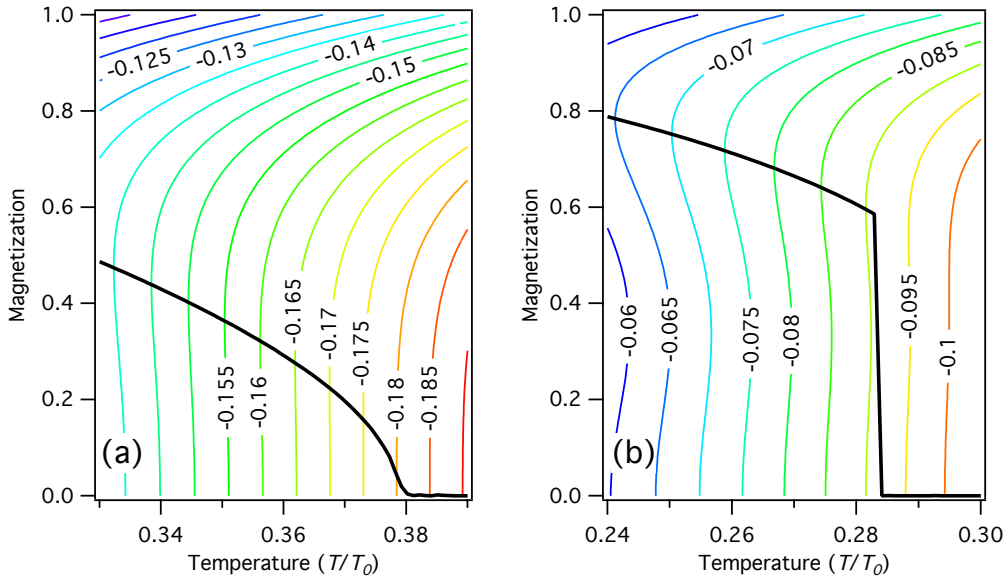

Figure B.3.: Contour plots of the free energy as a function of temperature and magnetization for different values of D, (a) for $D/(zJ) = 0.45$ and (b) for $D/(zJ) = 0.47$.

for $m = 0$ when $D = 0.45$. Hence, the magnetization can continuously decreases to zero, which corresponds to a second-order phase transition. However, Fig B.3 (b) indicates that before the magnetization decreases to zero, the free energy for $m = 0$ is already lower than the free energy for $m > 0$. Hence, the magnetization can decease discontinuously, which corresponds to a first-order phase transition.

Actually, we can obtain the critical temperature of second-order transition from Eq. (B.14). At the second-order transition temperature, $m \to 0$, hence Eq. (B.14) becomes

$$\lim_{m\to 0} m = \lim_{m\to 0} \frac{\sinh(\frac{m}{T'})}{\frac{1}{2}\exp(\frac{\delta}{T'}) + \cosh(\frac{m}{T'})} = \lim_{m\to 0} \frac{m}{\frac{1}{2}T'\exp(\frac{\delta}{T'}) + T'}. \tag{B.23}$$

As a result, we obtain

$$\exp(\frac{\delta}{T'}) = \frac{2}{T'} - 2. \tag{B.24}$$

Eq. (B.24) only has solutions for $\delta < 0.463$. For $\delta \leqslant 0$, Eq. (B.24) only has one solution. However, when $0 < \delta < 0.463$, Eq (B.24) has two solutions. The lower critical temperature, which corresponds to the unstable magnetization solution, will not be discussed in this section. As a result, when $D < 0.463$, we can expect a second-order phase transition of the Ising system with zero-field splitting. The critical temperature can be obtained by solving Eq. (B.24). The numerical results are shown in Fig. B.4 as a function of zero-field splitting parameter. When the

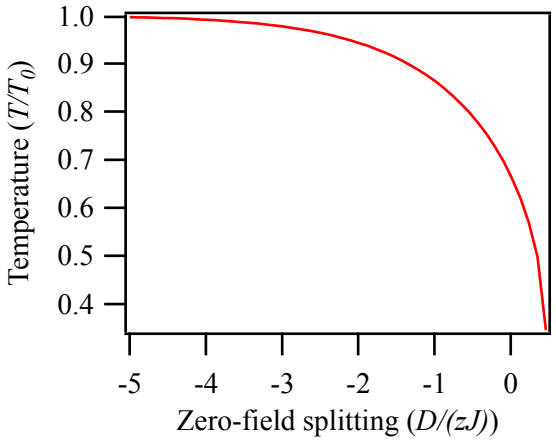

Figure B.4.: Second-order transition temperature as a function of zero-field splitting parameter.

zero-field splitting increases from $-\infty$ to 0.463, the critical temperature decreases from T_0 to $0.3165T_0$.

Considering the difference of the free energy between $m \neq 0$ and $m = 0$ as a function of temperature, we find

$$\Phi(m, T') - \Phi(0, T') = -T' \ln \left[\frac{1 + 2\exp\left(-\frac{\delta}{T'}\right)\cosh\left(\frac{m}{T'}\right)}{1 + 2\exp\left(-\frac{\delta}{T'}\right)} \right] + \frac{1}{2}m^2. \tag{B.25}$$

For a first-order phase transition, the magnetization cannot decrease continuously to zero because there is a critical temperature T_{c1}, where the free energy for magnetization $m_{c1} \neq 0$ is equal to the free energy for $m = 0$. When the temperature increases above T_{c1}, $m = 0$ is the lowest energy state. As a result, we have

$$\Phi(m, T') - \Phi(0, T') = 0. \tag{B.26}$$

When a first-order transition exists, Eq. (B.26) always has nonzero solutions. Substituting Eq. (B.14) into Eq. (B.26), we can numerically obtain the solutions as shown in Fig B.5. The red line is the critical temperature as a function of zero-field splitting, and the blue line is the critical magnetization as a function of zero-field splitting. When the zero-field splitting increases from 0.464 to 0.49, the critical temperature decreases from $0.3182T_0$ to 0.1827, and the critical magnetization increases from 0.3321 to 0.9076.

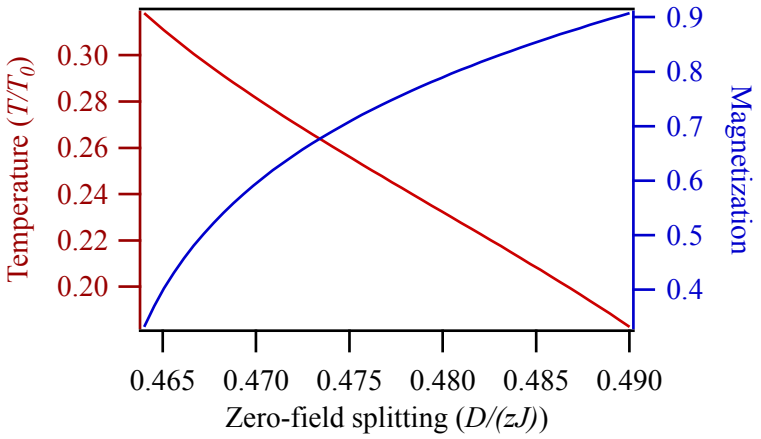

Figure B.5.: First-order transition temperature and the critical magnetization as a function of zero-field splitting parameter.

Antiferromagnetic Spin-1 Ising model with zero-field splitting

In the ferromagnetic case, all the spins' mean values are assumed to be the same for the entire lattice. However, in the antiferromagnetic case, this approximation needs to be modified in a different way [103, 104]. The lattice is divided into sub-lattices, in order to obtain opposite spin directions in the ground state. If the lattice can be decomposed into two equivalent sub-lattices, such as cubic lattices, the partition function of the corresponding antiferromagnetic Ising system is identical to the ferromagnetic Ising system discussed before.

Considering an antiferromagnetic Ising system on a 3-dimensional cubic lattice, we can decompose the cubic lattice into two sub-lattices A and B, which are shown in Fig. B.6. The nearest neighbors of A belong to B, and vice versa. Thus, the two sub-lattices are equivalent. The magnetization of sub-lattices A and B can be expressed as

$$m_A = -\frac{\sinh(\frac{T_0}{T} m_B)}{\frac{1}{2}\exp(\frac{T_0}{T}\delta) + \cosh(\frac{T_0}{T} m_B)} \tag{B.27a}$$

$$m_B = -\frac{\sinh(\frac{T_0}{T} m_A)}{\frac{1}{2}\exp(\frac{T_0}{T}\delta) + \cosh(\frac{T_0}{T} m_A)}, \tag{B.27b}$$

where $T_0 = z|J|/k_B$ and $\delta = D/(z|J|)$. Obviously, $m_A = -m_B$ is the solution of Eqs. (B.27). Substituting $m_A = -m_B$ into Eqs. (B.27), we obtain

$$m_A = -\frac{\sinh(\frac{T_0}{T} m_A)}{\frac{1}{2}\exp(\frac{T_0}{T}\delta) + \cosh(\frac{T_0}{T} m_A)} \tag{B.28a}$$

$$m_B = -\frac{\sinh(\frac{T_0}{T} m_B)}{\frac{1}{2}\exp(\frac{T_0}{T}\delta) + \cosh(\frac{T_0}{T} m_B)}. \tag{B.28b}$$

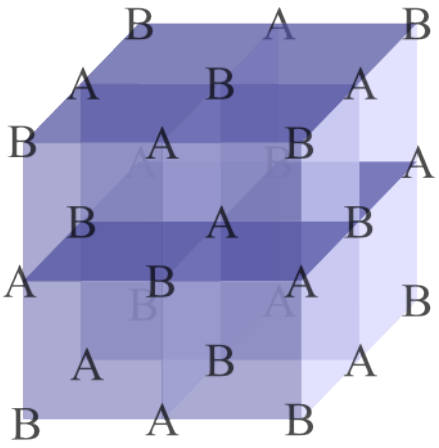

Figure B.6.: Sub-lattices A and B decomposition of a 3-dimensional cubic lattice.

The solutions for m_A and m_B are identical to the ferromagnetic Ising system with zero-field splitting except that m_A and m_B always have opposite sign. Hence, we can expect first-order and second-order phase transitions from antiferromagnetic order to the disordered state. The possible phase transitions are summarized in Tab. B.1.

Table B.1.: Phase transitions of the antiferromagnetic Ising model with different zero-field splittings.

Zero-field splitting	Phase transition	Critical Temperature
$-\infty < D < 0.463z\|J\|$	Second-order	$z\|J\|/k_B > T_{c2} > 0.3165z\|J\|/k_B$
$0.463z\|J\| < D < 0.5z\|J\|$	First-order	$0.3165z\|J\|/k_B > T_{c2} > 0$
$0.5z\|J\| < D$	No transition	0

Bibliography

[1] E. Grochowski and R. D. Halem. Technological impact of magnetic hard disk drives on storage systems. *IBM Systems Journal*, 42(2):338–346, 2003.

[2] E. Grochowski and R. F. Hoyt. Future trends in hard disk drives. *IEEE Transactions on Magnetics*, 32(3):1850–1854, 1996.

[3] M. N. Baibich, J. M. Broto, A. Fert, F. N. Van Dau, F. Petroff, P. Etienne, G. Creuzet, A. Friederich, and J. Chazelas. Giant magnetoresistance of (001)Fe/(001)Cr magnetic superlattices. *Physical Review Letters*, 61:2472–2475, 1988.

[4] G. Binasch, P. Grünberg, F. Saurenbach, and W. Zinn. Enhanced magnetoresistance in layered magnetic structures with antiferromagnetic interlayer exchange. *Physical Review B*, 39:4828–4830, Mar 1989.

[5] S. S. P. Parkin, C. Kaiser, A. Panchula, P. M. Rice, B. Hughes, M. Samant, and S.-H. Yang. Giant tunnelling magnetoresistance at room temperature with MgO(100) tunnel barriers. *Nature Materials*, 3(12):862–867, 12 2004.

[6] S. Yuasa, T. Nagahama, A. Fukushima, Y. Suzuki, and K. Ando. Giant room-temperature magnetoresistance in single-crystal Fe/MgO/Fe magnetic tunnel junctions. *Nature Materials*, 3(12):868–871, 2004.

[7] M. F. Doerner, K. Tang, T. Arnoldussen, H. Zeng, M. F. Toney, and D. Weller. Microstructure and thermal stability of advanced longitudinal media. *IEEE Transactions on Magnetics*, 36(1):43–47, 2000.

[8] D.A. Thompson and J.S. Best. The future of magnetic data storage techology. *IBM Journal of Research and Development*, 44(3):311–322, 2000.

[9] D. Weller and Andreas Moser. Thermal effect limits in ultrahigh-density magnetic recording. *IEEE Transactions on Magnetics*, 35(6):4423–4439, 1999.

[10] S. N. Piramanayagam. Perpendicular recording media for hard disk drives. *Journal of Applied Physics*, 102(1):011301, 2007.

[11] H. J. Richter. The transition from longitudinal to perpendicular recording. *Journal of Physics D: Applied Physics*, 40(9):R149, 2007.

[12] M.H. Kryder, E.C. Gage, T.W. McDaniel, W.A. Challener, R.E. Rottmayer,

G. Ju, Y.-T. Hsia, and M.F. Erden. Heat assisted magnetic recording. *Proceedings of the IEEE*, 96(11):1810–1835, 2008.

[13] W. A. Challener, Chubing Peng, A. V. Itagi, D. Karns, W. Peng, Y. Peng, X. Yang, X. Zhu, N. J. Gokemeijer, Y. T. Hsia, G. Ju, R. E. Rottmayer, M. A. Seigler, and E. C. Gage. Heat-assisted magnetic recording by a near-field transducer with efficient optical energy transfer. *Nature Photonics*, 3(4):220–224, 2009.

[14] J.-U. Thiele, S. Maat, and E. E. Fullerton. FeRh/FePt exchange spring films for thermally assisted magnetic recording media. *Applied Physics Letters*, 82(17):2859–2861, 2003.

[15] J.-U. Thiele, S. Maat, J.L. Robertson, and E.E. Fullerton. Magnetic and structural properties of FePt-FeRh exchange spring films for thermally assisted magnetic recording media. *IEEE Transactions on Magnetics*, 40(4):2537–2542, 2004.

[16] J. S. Kouvel and C. C. Hartelius. Anomalous magnetic moments and transformations in the ordered alloy FeRh. *Journal of Applied Physics*, 33(3):1343–1344, 1962.

[17] J. S. Kouvel. Unusual nature of the abrupt magnetic transition in FeRh and its pseudobinary variants. *Journal of Applied Physics*, 37(3):1257–1258, 1966.

[18] E. F. Kneller and R. Hawig. The exchange-spring magnet: a new material principle for permanent magnets. *IEEE Transactions on Magnetics*, 27(4):3588–3560, 1991.

[19] J.-U. Thiele, M. Buess, and C. H. Back. Spin dynamics of the antiferromagnetic-to-ferromagnetic phase transition in FeRh on a subpicosecond time scale. *Applied Physics Letters*, 85(14):2857–2859, 2004.

[20] G. Ju, J. Hohlfeld, B. Bergman, R. van de Veerdonk, O. N. Mryasov, J. Kim, X. Wu, D. Weller, and B. Koopmans. Ultrafast generation of ferromagnetic order via a laser-induced phase transformation in FeRh thin films. *Physical Review Letters*, 93:197403, 2004.

[21] L. Muldawer and F. Debergevin. Antiferromagnetic-ferromagnetic transformation in FeRh. *Journal of Chemical Physics*, 35(5):1904–1905, 1961.

[22] Y. Ding, D. A. Arena, J. Dvorak, M. Ali, C. J. Kinane, C. H. Marrows, B. J. Hickey, and L. H. Lewis. Bulk and near-surface magnetic properties of FeRh thin films. *Journal of Applied Physics*, 103(7):07B515, 2008.

[23] C. Baldasseroni, C. Bordel, A. X. Gray, A. M. Kaiser, F. Kronast, J. Herrero-Albillos, C. M. Schneider, C. S. Fadley, and F. Hellman. Temperature-driven nucleation of ferromagnetic domains in FeRh thin films. *Applied Physics Letters*, 100(26):262401, 2012.

[24] J. Cao, N. T. Nam, S. Inoue, H. Y. Y. Ko, N. N. Phuoc, and T. Suzuki. Magnetization behaviors for FeRh single crystal thin films. *Journal of Applied Physics*, 103(7):07F501, 2008.

[25] C. Bordel, J. Juraszek, D. W. Cooke, C. Baldasseroni, S. Mankovsky, J. Minar, H. Ebert, S. Moyerman, E. E. Fullerton, and F. Hellman. Fe spin reorientation across the metamagnetic transition in strained FeRh thin films. *Physical Review Letters*, 109(11):117201, 2012.

[26] M. J. McLaren, M. A. de Vries, R. M. D. Brydson, and C. Marrows. Characterisation of magnetic FeRh epilayers. *Journal of Physics: Conference Series*, 371(1):012031, 2012.

[27] M. Loving, M. A. de Vries, F. Jimenez-Villacorta, C. Le Graet, X. Liu, R. Fan, S. Langridge, D. Heiman, C. H. Marrows, and L. H. Lewis. Tailoring the FeRh magnetostructural response with Au diffusion. *Journal of Applied Physics*, 112(4):043512, 2012.

[28] G. Shirane, R. Nathans, and C. W. Chen. Magnetic moments and unpaired spin densities in the Fe-Rh alloys. *Physical Review*, 134:A1547–1553, 1964.

[29] G. Shirane, C. W. Chen, P. A. Flinn, and R. Nathans. Mössbauer study of hyperfine fields and isomer shifts in the Fe-Rh alloys. *Physical Review*, 131:183–190, 1963.

[30] E. Kren, L. Pal, and P. Szabo. Neutron diffraction investigation of the antiferromagnetic-ferromagnetic transformation in the FeRh alloy. *Physics Letters*, 9(4):297–298, 1964.

[31] M. R. IbarraI and P. A. Algarabel. Giant volume magnetostriction in the FeRh alloy. *Physical Review B*, 50(6):4196–4199, 1994.

[32] P. E. M. Hofer and P. E. Cucka. Magnetic Properties of Rh-rich FeRh alloy. *Journal of Physics and Chemistry*, 27(9):1552–1555, 1966.

[33] V. L. Moruzzi and P. M. Marcus. Antiferromagnetic-ferromagnetic transition in FeRh. *Physical Review B*, 46:2864–2873, 1992.

[34] L. M. Sandratskii and P. Mavropoulos. Magnetic excitations and femtomagnetism of FeRh: A first-principles study. *Physical Review B*, 83(17):174408, 2011.

[35] C. Kittel. Model of exchange-inversion magnetization. *Physical Review*, 120:335–342, 1960.

[36] P. Tu, A. J. Heeger, J. S. Kouvel, and J. B. Comly. Mechanism for the first-order magnetic transition in the FeRh system. *Journal of Applied Physics*, 40(3):1368–1369, 1969.

[37] W. Nolting and A. Ramakanth. *Quantum Theory of Magnetism*. Spinger, Heidelberg, 2009.

[38] M. Blume. Theory of the first-order magnetic phase change in UO_2. *Physical Review*, 141:517–524, 1966.

[39] H. W. Capel. On the possibility of first-order phase transitions in ising systems of triplet ions with zero-field splitting. *Physica*, 32(5):966–988, 1966.

[40] H. W. Capel. On the possibility of first-order transitions in ising systems of triplet ions with zero-field splitting ii. *Physica*, 33(2):295–331, 1967.

[41] H. W. Capel. On the possibility of first-order transitions in ising systems of triplet ions with zero-field splitting iii. *Physica*, 37(3):423–441, 1967.

[42] M. E. Gruner and E. Hoffmannand P. Entel. Instability of the rhodium magnetic moment as the origin of the metamagnetic phase transition in α-FeRh. *Physical Review B*, 67(6):064415, 2003.

[43] S. Maat, J.-U. Thiele, and E. E. Fullerton. Temperature and field hysteresis of the antiferromagnetic-to-ferromagnetic phase transition in epitaxial FeRh films. *Physical Review B*, 72(21):214432, 2005.

[44] R. C. Wayne. Pressure dependence of the magnetic transitions in Fe-Rh alloys. *Physical Review*, 170:523–527, 1968.

[45] L.D. Landau and E. Lifshitz. On the theory of the dispersion of magnetic permeability in ferromagnetic bodies. *Physikalische Zeitschrift der Sowjetunion*, 8:153–169, 1935.

[46] C. Kittel. Physical theory of ferromagnetic domains. *Reviews of Modern Physics*, 21:541–583, 1949.

[47] M.J. Donahue and R.D. McMichael. Exchange energy representations in computational micromagnetics. *Physica B: Condensed Matter*, 233(4):272 – 278, 1997.

[48] S. Chikazumi. *Physics of Ferromagnetism*. Oxford University Press Inc., New York, 2nd edition, 1997.

[49] A. Hubert and R. Schäfer. *Magnetic domains: The analysis of magnetic microstructures*. Springer, Berlin, 1998.

[50] H. P. Oepen and J. Kirschner. Magnetization distribution of 180° domain walls at Fe(100) single-crystal surfaces. *Physical Review Letters*, 62:819–822, 1989.

[51] M. Speckmann, H. P. Oepen, and H. Ibach. Magnetic domain structures in ultrathin Co/Au(111): On the influence of film morphology. *Physical Review Letters*, 75:2035–2038, 1995.

[52] J. M. Lommel. Magnetic and electrical properties of FeRh thin films magnetic and electrical properties of FeRh thin films. *Journal of Applied Physics*, 37(3):1483–1484, 1966.

[53] S. Inoue, N. N. Phuoc, J. Cao, N. T. Nam, H.Y. Y. Ko, and T. Suzuki. Structural and magneto-optical properties of FeRh thin films. *Journal of Applied Physics*, 103(7):07B312, 2008.

[54] C. Stamm, J. . U. Thiele, T. Kachel, I. Radu, P. Ramm, M. Kosuth, J. Minar, H. Ebert, H. A. Duerr, W. Eberhardt, and C. H. Back. Antiferromagnetic-ferromagnetic phase transition in FeRh probed by x-ray magnetic circular dichroism. *Physical Review B*, 77(18):184401, 2008.

[55] J.-S. Lee, E. Vescovo, L. Plucinski, C. M. Schneider, and C.-C. Kao. Electronic structure and magnetic properties of epitaxial FeRh(001) ultrathin films on W(100). *Physical Review B*, 82:224410, 2010.

[56] S.-U. Jang, E. B. Park, J.-H. Kim, K.-H. Park, J. S. Lee, Y. K. Kim, S. Hyun, H.-J. Lee, S.-J. Kwon, and H.-S. Lee. Observation of suppressed interdiffusion in FeRh/FePt-Ta bilayer thin films. *IEEE Transactions on Magnetics*, 46(6):2104–2107, 2010.

[57] J. E. Mahan. *Physical vapor Deposition of Thin Films*. John Wiley & Sons, 2000.

[58] M. Björck and G. Andersson. *GenX*: an extensible X-ray reflectivity refinement program utilizing differential evolution. *Journal of Applied Crystallography*, 40(6):1174–1178, 2007.

[59] K. Pussi and R. D. Diehl. Low-energy electron diffraction. In Elton N. Kaufmann, editor, *Characterization of Materials*. John Wiley & Sons, 2nd edition, 2012.

[60] L. J. Clarke. *Surface Crystallography*. John Wiley & Sons, 1985.

[61] S. Hofmann. *Auger- and X-Ray Photoelectron Spectroscopy in Materials Science*. Springer, 2013.

[62] CasaXPS manual: Introduction to XPS and AES, 2009.

[63] A. Savitzky and M. J. E. Golay. Smoothing and differentiation of data by simplified least squares procedures. *Analytical Chemistry*, 36(8):1627–1639, 1964.

[64] K. D. Childs, B. A. Carlson, L. A. LaVanier, J. F. Moulder, D. F. Paul, W. F. Stickle, and D. G. Watson. *Handbook of Auger Electron Spectroscopy*. Physical Electronics Inc, Minnesota, 3rd edition, 1995.

[65] C.C. Chang. General formalism for quantitative Auger analysis. *Surface Science*, 48(1):9–21, 1975.

[66] P. W. Palmberg. Quantitative Auger electron spectroscopy using elemental sensitivity factors. *Journal of Vacuum Science and Technology*, 13(1):214–218, 1976.

[67] S.D. Bader. SMOKE. *Journal of Magnetism and Magnetic Materials*, 100(1–3):440–454, 1991.

[68] M. Buchmeier, R. Schreiber, D. E. Bürgler, and C. M. Schneider. Thickness dependence of linear and quadratic magneto-optical Kerr effects in ultrathin Fe(001) films. *Physical Review B*, 79:064402, 2009.

[69] Z. Q. Qiu and S. D. Bader. Surface magneto-optic Kerr effect. *Review of Scientific Instruments*, 71(3):1243–1255, 2000.

[70] Z.Q Qiu and S.D Bader. Surface magneto-optic kerr effect (SMOKE). *Journal of Magnetism and Magnetic Materials*, 200(1–3):664 – 678, 1999.

[71] J. M. Bennett. Polarizers. In *Handbook of Optics*, volume 1, chapter 13. McGraw-Hill, Inc., New York, USA, 3rd edition, 2010.

[72] R. Frömter, H. P. Oepen, and J. Kirschner. A miniaturized detector for high-resolution sempa. *Applied Physics A: Materials Science & Processing*, 76(6):869–871, 2003.

[73] L. Reimer. *Scanning Electron Microscopy - Physics of Image Fromation and Microanalsis*. Springer, Heidelberg, 2nd edition, 1998.

[74] J. Unguris, D. T. Pierce, A. Galejs, and R. J. Celotta. Spin and energy analyzed secondary electron emission from a ferromagnet. *Physical Review Letters*, 49:72–76, 1982.

[75] H. P. Oepen and R. Frömter. Scanning electron microscopy with polarisation analysis. In *Handbook of Magnetism and Advanced Magnetic Materials*. John Wiley & Sons, 2007.

[76] J. Kirschner and R. Feder. Spin polarization in double diffraction of low-energy electrons from W(001): Experiment and theory. *Physical Review Letters*, 42:1008–1011, 1979.

[77] R. Feder. Spin-polarised low-energy electron diffraction. *Journal of Physics C: Solid State Physics*, 14:2049–2091, 1981.

[78] R. Fromter, S. Hankemeier, H. P. Oepen, and J. Kirschner. Optimizing a low-energy electron diffraction spin-polarization analyzer for imaging of magnetic surface structures. *Review of Scientific Instruments*, 82(3):033704, 2011.

[79] J. Kirschner. *Polarized Electrons at Sufraces*. Spinger, Heidelberg, 1985.

[80] V. N. Petrov, V. V. Grebenshikov, B. D. Grachev, and A. S. Kamochkin. New compact classical 40 kV Mott polarimeter. *Review of Scientific Instruments*, 74(3):1278–1281, 2003.

[81] M. Zölfl, M. Brockmann, M. Köhler, S. Kreuzer, T. Schweinböck, S. Miethaner, F. Bensch, and G. Bayreuther. Magnetic films epitaxially grown on semiconductors. *Journal of Magnetism and Magnetic Materials*, 175(1–2):16–22, 11 1997.

[82] J. Unguris, S.-H. Chung, and D. T. Pierce. SEMPA imaging for spintronics applications. In D. G. Seiler, A. C. Diebold, R. McDonald, C. M. Garner, D. Herr, R. P. Khosla, and E. M. Secula, editors, *AIP Conference Proceedings*, volume 931, 2007.

[83] H. Tokutaka and M. Prutton. LEED observations of the (11) beam from the (100) surfaces of some NaCl-type crystals. *Surface Science*, 11(2):216–226, 1968.

[84] Richard L. Schwoebel and Edward J. Shipsey. Step motion on crystal surfaces. *Journal of Applied Physics*, 37(10):3682–3686, 1966.

[85] Gert Ehrlich and F. G. Hudda. Atomic view of surface self-diffusion: Tungsten on Tungsten. *The Journal of Chemical Physics*, 44(3):1039–1049, 1966.

[86] K. Thürmer, R. Koch, M. Weber, and K. H. Rieder. Dynamic evolution of pyramid structures during growth of epitaxial Fe(001) films. *Physical Review Letters*, 75:1767–1770, 1995.

[87] L. Zsoldos. Lattice paramter change of FeRh alloys due to antiferromagnetic-ferromagnetic transformation. *Physica Status Solidi*, 20(1):K25, 1967.

[88] S. Inoue, H. Y. Y. Ko, and T. Suzuki. Magnetic properties of single-crystalline FeRh alloy thin films. *IEEE Transactions on Magnetics*, 44(11):2875 –2878, 2008.

[89] K.M Cher, T.J. Zhou, and J.S. Chen. Compositional effects on the structure and phase transition of epitaxial FeRh thin films. *IEEE Transactions on Magnetics*, 47(10):4033 –4036, 2011.

[90] J. A. Bearden and A. F. Burr. Reevaluation of X-Ray atomic energy levels. *Reviews of Modern Physics*, 39:125–142, 1967.

[91] J. M. Lommel and J. S. Kouvel. Effects of mechanical and thermal treatment on the structure and magnetic transitions in FeRh. *Journal of Applied Physics*, 38(3):1263, 1967.

[92] J. A. Ricodeau and D. Melville. Model of the antiferromagnetic-ferromagnetic transition in FeRh alloys. *Journal of Physics F: Metal Physics*, 2(2):337, 1972.

[93] F. Lofink, S. Hankemeier, R. Frömter, J. Kirschner, and H. P. Oepen. Long-time stability of a low-energy electron diffraction spin polarization analyzer for magnetic imaging. *Review of Scientific Instruments*, 83(2):023708, 2012.

[94] P. Bruno and J. P. Renard. Magnetic surface anisotropy of transition metal ultrathin films. *Applied Physics A*, 49(5):499–506, 1989.

[95] J. W. Kim, P. J. Ryan, Y. Ding, L. H. Lewis, M. Ali, C. J. Kinane, B. J. Hickey, C. H. Marrows, and D. A. Arena. Surface influenced magnetostructural transition in FeRh films. *Applied Physics Letters*, 95(22):222515, 2009.

[96] M. Rickart, B. F. P. Roos, T Mewes, J. Jorzick, S. O. Demokritov, and B. Hillebrands. Morphology of epitaxial metallic layers on MgO substrates: influence of submonolayer carbon contamination. *Surface Science*, 495:68–76, 2001.

[97] C. Duriez, C. Chapon, C.R. Henry, and J.M. Rickard. Structural characterization of MgO(100) surfaces. *Surface Science*, 230:123–136, 1990.

[98] C. Marquina, M. R. Ibarra, P. A. Algarabel, A. Hernando, P. Crespo, P. Agudo, A. R. Yavari, and E. Navarro. Magnetic and magnetoelastic behavior of mechanically alloyed FeRh compound. *Journal of Applied Physics*, 81(5):2315–2320, 1997.

[99] R. Fan, C. J. Kinane, T. R. Charlton, R. Dorner, M. Ali, M. A. de Vries, R. M. D. Brydson, C. H. Marrows, B. J. Hickey, D. A. Arena, B. K. Tanner, G. Nisbet, and S. Langridge. Ferromagnetism at the interfaces of antiferromagnetic FeRh epilayers. *Physical Review B*, 82:184418, 2010.

[100] M. Plischke and B. Bergersen. *Equilibrium Statistical Physics*. World Scientific Publishing, 3rd edition, 2006.

[101] L. Peliti. *Statistical Mechanics in a Nutshell*. Princeton University Press, New Jersey, 2003.

[102] M. Blume, V. J. Emery, and Robert B. Griffiths. Ising model for the λ transition and phase separation in He^3-He^4 mixtures. *Physical Review A*, 4:1071–1077, 1971.

[103] J. H. Van Vleck. On the theory of antiferromagnetism. *The Journal of Chemical Physics*, 9(1):85–90, 1941.

[104] C. Domb. On the theory of cooperative phenomena in crystals. *Advances in Physics*, 9(34):149–244, 1960.

Acknowledgement

I would like to express my deepest appreciation to all those who provided support for this thesis:

- My doctoral supervisor PD Dr. Daniel E. Bürgler, who gave me the opportunity to pursue this doctoral thesis in Germany and shared his valuable experience with me.
- Prof. Dr. Thomas Michely, who spend his valuable time to review my thesis.
- Prof. Dr. Achim Rosch, who agreed to chair the thesis committee.
- Prof. Dr. Claus M. Schneider, who gave me the opportunity to do my doctoral thesis in his institute, the PGI-6 of the Research Center Jülich.
- My colleagues Dr. Frank Matthes, Dr. Christian Caspers, Dr. Rajeswari Jayaraman, Saban Tirpanci, and all the other colleagues in the PGI-6 for experimental support and the pleasant working atmosphere.
- The mechanical and electronic workshops, in particular Thomas Jansen, Franz-Josef Köhne, Heinz Pfeifer, and Norbert Schnitzler, who provided important technical support to my doctoral thesis.

At last, I would like to express a sense of gratitude and love to my wife, my parents and my brother for their endless love to me and their support to my doctoral study in Germany.

Erklärung

Ich versichere, dass ich die von mir vorgelegte Dissertation selbständig angefertigt, die benutzten Quellen und Hilfsmittel vollständig angegeben und die Stellen der Arbeit - einschließlich Tabellen, Karten und Abbildungen -, die anderen Werken im Wortlaut oder dem Sinn nach entnommen sind, in jedem Einzelfall als Entlehnung kenntlich gemacht habe; dass diese Dissertation noch keiner anderen Fakultät oder Universität zur Prüfung vorgelegen hat; dass sie - abgesehen von unten angegebenen Teilpublikationen - noch nicht veröffentlicht worden ist sowie, dass ich eine solche Veröffentlichung vor Abschluss des Promotionsverfahrens nicht vornehmen werde. Die Bestimmungen der Promotionsordnung sind mir bekannt. Die von mir vorgelegte Dissertation ist von PD Dr. Daniel E. Bürgler betreut worden.

Xianzhong Zhou

Jülich, 05.11.2013

Curriculum Vitæ

Birth	1985	Zhuhai, Guangdong, China
Primary School	09.1991-07.1997	Xinxing Primary School, Zhuhai, Guangdong, China
Junior middle school	09.1997-07.2000	Lianxi Middle School, Zhuhai, Guangdong, China
Senior middle school	09.2000-07.2003	Doumen First Middle School, Zhuhai, Guangdong, China
Bachelor study	09.2003-07.2007	Harbin Institute of Technology, Harbin, Heilongjiang, China
Master study	09.2007-07.2009	Harbin Institute of Technology, Harbin, Heilongjiang, China
Doctoral study	02.2010-12.2013	Peter Grünberg Institut, Electronic Properties (PGI-6), Research Center Jülich, Jülich, Germany